Supplement to February 2025
Volume 54, Number 1

AppliedRadiology®
The Journal of Practical Medical Imaging and Management

Leaders on the Horizon Residents Program 2024

CLINICAL RESEARCH

Abhijan Maity, MD
Indira Gandhi Government Medical College

Kamyar Ghabili, MD
Penn State Health
Milton S. Hershey Medical Center

Luis Lorenzo A. Chan, MD
St. Luke's Medical Center

CLINICAL REVIEW

Hira Qureshi, MD
Henry Ford Hospital

Yesim Yekta Yuruk, MD
Health Science University Hospital

Jacob Schick, MD
Johns Hopkins Medicine

Supported by Bracco Diagnostics, Inc.

Applied Radiology®

The Journal of Practical Medical Imaging and Management

Anderson Publishing, Ltd
180 Glenside Avenue,
Scotch Plains, NJ 07076
Tel: 908-301-1995
Fax: 908-301-1997
info@appliedradiology.com

PRESIDENT & CEO
Oliver Anderson

GROUP PUBLISHER
Kieran N. Anderson

EDITOR-IN-CHIEF
Erin Simon Schwartz, MD, FACR

MANAGING EDITOR
Claudia Stahl

PRODUCTION
Barbara A. Shopiro

FOREWORD

I am pleased to present this special supplement to *Applied Radiology*, featuring the winning papers from the 2024 *Leaders on the Horizon* Residents Program. These 6 papers, authored by an outstanding group of early-career radiologists, reflect diverse and international perspectives on advancements in medical imaging. I would also like to recognize all of our applicants for the time and effort that it took to develop and submit their work for consideration.

Leaders on the Horizon is made possible through the generous support of Bracco Diagnostics Inc., whose unrestricted educational grant enables us to identify and showcase exemplary research from radiology residents worldwide. Since expanding eligibility to international participants in 2023, submissions have continued to grow, with the latest winners representing 4 countries across 3 continents.

We would like to express our sincere gratitude to our expert review panel: Drs. Lorna Browne, Christopher Comstock, Mark C. DeLano, Paul Finn, Elliot Fishman, Alessandro Furlan, Christine Glastonbury, Ryan Lee, Louis Mazzarelli, Mahmud Mossa-Basha, Neil Rofsky, Frank Shellock, and Lawrence Tanenbaum, for upholding the highest standards in selecting the winners.

2024 Leaders on the Horizon Winners

Research Category

First Place: Abhijan Maity, MD – Indira Gandhi Government Medical College, Nagpur, India

Second Place: Kamyar Ghabili, MD – Penn State Health Milton S. Hershey Medical Center, Hershey, PA

Third Place: Luis Chan, MD – St. Luke's Medical Center, Quezon City, Philippines

Review Category

First Place: Hira Qureshi, MD – Henry Ford Hospital, Detroit, MI

Second Place: Yesim Yuruk, MD – Health Sciences University Izmir Tepecik Hospital, Izmir, Turkey

Third Place: Jacob Schick, MD – Johns Hopkins Medicine, Baltimore, MD

For information on the 2025 *Leaders on the Horizon* Residents Program, including registration and submission details, visit appliedradiology.com/leaders.

Sincerely,

Group Publisher, *Applied Radiology*
Anderson Publishing, Ltd.

LEADERS ON THE HORIZON 2024

CLINICAL RESEARCH

CLINICAL REVIEW

Diagnostic Accuracy of Cerebroplacental Ratio in Anticipating Adverse Perinatal Outcome in Uncomplicated Appropriate-for-Gestational-Age Pregnancies at Term

Abhijan Maity, MBBS; Bhawana Sonawane, MD; Anagha Deshpande, MD; Sunita Bhutada, MD

Abstract

Objectives and Hypothesis: Anticipating which babies are in danger of experiencing poor outcomes during the perinatal period in uncomplicated appropriate-for-gestational-age (AGA) pregnancies at term is difficult in obstetric practice. Cerebroplacental ratio (CPR) is emerging as a significant indicator of negative perinatal results. The current study sought to establish the efficacy of CPR in predicting negative perinatal outcomes in term uncomplicated AGA pregnancies.

Materials and Methods: This was a hospital-based prospective observational cohort study conducted at a single center. Patients were chosen based on different criteria for inclusion and exclusion. A prenatal color Doppler US scan was carried out to calculate CPR. Patients were grouped into either normal CPR or pathological CPR categories based on their last CPR measurement before delivery. Doppler results did not impact clinical decisions, and delivery followed institutional protocols. After childbirth, data on the outcome of the perinatal period were obtained from the patients' medical records. Negative perinatal outcomes were assessed through the delivery method, APGAR score, perinatal morbidity, and perinatal mortality. These outcomes were correlated with CPR.

Results: The study included 605 women separated into normal and pathological CPR groups. Of these, 452 (74.7%) were assigned to the normal CPR category, and 153 (25.3%) were assigned to the pathological CPR category. In our study, 138 patients in the pathological CPR group experienced adverse perinatal outcomes, while 44 patients in the normal CPR group experienced adverse outcomes. The diagnostic accuracy of pathological CPR to predict any negative perinatal result was 90.25%.

Conclusion: The CPR shows potential in detecting at-risk fetuses in full-term uncomplicated AGA pregnancies.

Keywords: cerebroplacental ratio, appropriate for gestational age, adverse perinatal outcome, term uncomplicated pregnancy

Introduction

A national, survey-based analysis published in 2023 found that 49.4% of Indian women experienced high-risk pregnancies, while 50.6% experienced low-risk pregnancies (LRPs).[1] Predicting whether a fetus is in danger of a negative perinatal outcome at term (37 weeks 0 days to 41 weeks 6 days of gestation) LRP is difficult. While high-risk pregnant women are promptly transferred from primary health care (PHC) to first referral unit (FRU) care, low-risk pregnant women, who make up the majority of those receiving antenatal care at PHC, frequently require

Affiliation: Department of Radio-diagnosis, Indira Gandhi Government Medical College and Hospital, Nagpur, India.
Disclosure: The authors have no conflicts of interest to disclose. None of the authors received outside funding for the production of this original manuscript and no part of this article has been previously published elsewhere.

Published: February 1, 2025. https://doi.org/10.37549/AR-D-24-0061

immediate referral to FRU for intrapartum fetal distress. Women requiring immediate transfer to an FRU for emergency cesarean section (CS) typically experience worse perinatal outcomes than those who are promptly referred for elective CS.[2] Therefore, a screening tool is necessary to identify LRPs at risk of adverse perinatal outcomes, allowing for timely referral to FRU and thus ultimately reducing perinatal morbidity and mortality.

Although being small for gestational age (SGA; ie, fetuses with estimated fetal weight or EFW below the 10th percentile for gestational age) is a recognized risk factor for poor perinatal outcomes, most adverse outcomes actually involve fetuses that are appropriate for gestational age (AGA; ie, fetuses with EFW between the 10th and 90th percentiles).[3] Hence, relying solely on EFW may not accurately identify all fetuses at risk for adverse perinatal outcomes at term.

Recent studies have shown that some AGA fetuses have not reached their full genetic growth potential by the end of pregnancy and may experience negative outcomes during the perinatal period.[4] Detecting fetuses at risk of perinatal complications, particularly those in LRPs, is currently the main challenge in obstetric health care. In recent years, the cerebroplacental ratio (CPR) has become increasingly important as a predictor of negative outcomes. This has consequences for assessing the well-being of SGA and AGA fetuses close to the end of pregnancy.[5]

Calculated by dividing the Doppler flow rate of the middle cerebral artery (MCA) by the flow rate of the umbilical artery (UA), the CPR is an obstetric US measurement that demonstrates how elevated placental resistance and fetal hypoxia lead to the redistribution of cardiac output to the cerebral circulation. Owing to cerebral vasodilation and increased diastolic flow, this brain-sparing effect leads to a reduction in the pulsatility index (PI) of the MCA[6] and helps protect the brain from damage. Although other Doppler indices such as the systolic/diastolic ratio and resistance index have been used to calculate CPR in the past, PI is currently the preferred method for estimating the CPR.[7]

Fetal hypoxia leads to increased perinatal morbidity and mortality rates and is a key factor in various neurodevelopmental issues, hypoxic-ischemic encephalopathy, stillbirth, and other negative perinatal results worldwide.[8] During labor, fetal hypoxia is caused by uterine contractions and falling uterine artery flow velocities, resulting in decreased placental perfusion.[9] Blood vessels in the brain react with vasodilation, decreasing resistance to blood flow and resulting in a lower PI in MCA.[10]

The majority of clinical research into the CPR has centered on evaluating complicated pregnancies. Little research has been conducted on how CPR is involved in evaluating pregnancies with no or low risk for complications. Our study aimed to assess how well CPR can predict adverse perinatal outcomes in term uncomplicated or low-risk AGA pregnancies.

Materials and Methods

This was a single-center, hospital-based prospective observational cohort study. Cases were chosen from among pregnant women being referred to our institution's Department of Radio-Diagnosis for antenatal color Doppler US scanning. The 2-year study was conducted between January 2022 and December 2023.

In addition to giving informed consent, participants in the study had to meet specific criteria for eligibility: (1) term pregnancy (37 weeks 0 days, or 259 days, to 41 weeks 6 days, or 293 days of gestation); (2) singleton pregnancy; (3) confirmed gestational age (based on crown-rump length measurement between 6 and 12 weeks of gestation); (4) nulliparous or previous normal vaginal delivery; (5) be between 20 and 35 years of age; (6) cephalic presentation; (7) normal amniotic fluid index (AFI, between 5 and 25 cm); and (8) AGA pregnancies (EFW between the 10th and 90th percentiles for the gestational age).

In addition to refusal to give informed consent, subjects were excluded for (1) preterm delivery (<37 weeks or <259 days of gestation); (2) post-term pregnancy (≥42 weeks 0 days, or 294 days); (3) twin or multiple pregnancies; (4) unconfirmed gestational age; (5) being below age 20 or above 35; (6) known fetal anomalies; (7) intrauterine fetal demise; (8) medical or surgical illnesses complicating pregnancy (eg, pregnancy-induced hypertension, preeclampsia, hypothyroidism, gestational diabetes mellitus, severe anemia, syphilis/HIV positive, and so forth); (9) Rh-negative; (10) poor obstetric history; (11) malpresentation; (12) low-lying placenta/placenta previa; (13) oligohydramnios (AMI < 5 cm) or polyhydramnios (AFI > 25 cm); (14) previous CS or uterine surgery such as myomectomy; (15) elective CS; (16) emergency CS for reasons other than intrapartum fetal compromise (IFC); and (17) SGA (EFW below the 10th percentile for the gestational age) or LGA (EFW above the 90th percentile for the gestational age) pregnancies.

The research was carried out according to the Declaration of Helsinki and received ethical approval from the institution's ethics committee. During their

initial appointment, patients were asked to give written consent in their native language before undergoing a thorough history and clinical examination. The evaluation included information about the mother's age, previous pregnancies, estimated gestational age from the last menstrual period, menstrual cycle and obstetric history, past or current medical conditions, surgical history, medication use or allergies, smoking habits, alcohol consumption, and tobacco use. The clinical assessment covered blood pressure, body mass index, and a general survey evaluation.

Each subject then underwent an antenatal color Doppler US scan for CPR calculation; this procedure was performed every 8 days until delivery to ensure Doppler values were current within 7 days of delivery. The final CPR before delivery was utilized for all examinations.

A single US machine, the Mindray DC 80, equipped with a Mindray SC6-1E transabdominal curved array transducer with a frequency range of 1.3-5.7 MHz, was used for all US procedures. An obstetric scanning guideline recommended by the US Food and Drug Administration was followed, keeping the spatial peak temporal average intensity below 94 mW/cm^2. Smart Care US gel was applied for transmission of the US.

The gestational age was verified by measuring the crown-rump length between 6 and 12 weeks of pregnancy. Fetal biometry and AFI were documented during every appointment. The EFW was determined using the Hadlock formula incorporating biparietal diameter, head and abdominal circumference, and femur length.[11] Fetuses with EFW below the 10th percentile for gestational age were classified as SMA, and those with EFW between the 10th and 90th percentile were classified as AGA.[12]

Doppler parameters were assessed based on the revised guidelines set by the International Society of Ultrasound in Obstetrics and Gynecology (ISUOG).[13] Doppler assessment of the UA was performed from a loose loop of the umbilical cord located away from the insertion sites of the placenta or the fetus. Assessment of the MCA was conducted by observing a cross-sectional image of the fetal head at the trans-thalamic plane, which includes the thalami and cavum septum pellucidum. MCA Doppler was evaluated in the circle of Willis in the straight part of the artery about 1 cm away from its origin at the internal carotid artery.

Efforts were made to avoid undue transducer compression on the fetal head, which can change intracranial pressure and affect Doppler assessment of the MCA. Two skilled radiologists recorded all Doppler waveforms while the patient was lying supine with the head of the bed raised at a 45° angle. The CPR was determined by dividing the MCA PI by the UA PI and utilizing reference ranges based on gestational age instead of relying on a single threshold. The CPR was assessed as either normal or abnormal using the calculator found at https://portal.medicinafetalbarcelona.org/calc/.[14]

Subjects were separated into 2 groups based on their last CPR measurement before delivery: one with normal CPR and the other with pathological CPR. The results from Doppler tests were not utilized in the treatment plan. Patients and obstetricians were unaware of the CPR outcomes. Labor and childbirth were conducted according to institutional protocols and guidelines. Post delivery, information on perinatal outcomes was retrieved from the patient's medical records.

Adverse perinatal outcomes were assessed through the mode of delivery (including instrumental deliveries or CS for IFC; diagnosis of IFC was determined by cardiotocographic abnormalities, fetal heart sound irregularities, meconium stained liquor, or a combination of these); APGAR scores < 7 at 5 minutes; perinatal morbidity (admission to the neonatal intensive care unit [NICU] within 24 hours post delivery); and perinatal mortality (including stillbirth and death within the first week of life). The CPR was correlated with negative outcomes during childbirth.

Statistical Analysis

The data gathered were inputted into a Microsoft Excel spreadsheet designed for Windows 10. Statistical Package for Social Sciences Version 22.0 (SPSS Inc., Chicago, Illinois, USA) software was used for statistical analysis, upon which the results were displayed in tables. Quantitative data were represented in numbers and percentages and presented as mean ± SD. Nonparametric tests such as the chi-square test were employed to test the significance of difference for qualitative data, and parametric tests such as independent *t* tests were performed to assess the significance of difference for quantitative data. Tests for diagnostic accuracy were performed by measuring sensitivity, specificity, positive predictive value (PPV), negative predictive value (NPV), positive likelihood ratio (positive LR), negative likelihood ratio (negative LR), area under receiver operating characteristic (ROC) curve (AUC-ROC), and overall diagnostic accuracy within a 95% CI. Any

Table 1. Baseline Characteristics of Study Population, *N* = 605

BASELINE CHARACTERISTICS	NORMAL CEREBROPLACENTAL RATIO (*N* = 452)	PATHOLOGICAL CEREBROPLACENTAL RATIO (*N* = 153)	*P* VALUE
Maternal age[a] (years)	26.97±4.32	27.11±4.3	.73[c]
Gestational age at time of last Doppler scan[a] (days)	273.11±7.7	273.66±7.45	.44[c]
Gestational age at time of delivery[a] (days)	277.15±7.54	277.75±7.28	1.0[c]
Interval between last scan and delivery[a] (days)	4.09±1.89	4.09±1.87	.39[c]
Residency[b] (% of patients)			.37[d]
Rural	244 (54)	89 (58)	
Urban	208 (46)	64 (42)	
Literacy[b] (% of patients)			.68[d]
Illiterate	105 (23)	38 (25)	
Literate	347 (77)	115 (75)	
Parity[b] (% of patients)			.98[d]
Nulliparous	261 (58)	87 (57)	
Primiparous	145 (32)	50 (33)	
Multiparous	46 (10)	16 (10)	

[a]*The data are given as the mean ± SD.*

[b]*The data are given as the number (%) of patients.*

[c]*Independent-sample Student t test.*

[d]*χ^2 test.*

probability value (*P* value) <.05 was deemed statistically significant with a 95% CI.

Results

In the study period, 627 women were deemed eligible for the study, with 12 women excluded from planned C-sections and 10 who were lost to follow-up. The ultimate group of participants included 605 female individuals. Of the 605 subjects, 452 (74.7%) were classified as having normal CPR, while 153 (25.3%) were classified to the pathological CPR group.

The study population's baseline characteristics were recorded. There was no notable discrepancy between the 2 groups in maternal age, parity, literacy, residency, average gestational age at delivery, average gestational age at the last Doppler scan, and the average interval between the final Doppler scan and delivery, as demonstrated in Table 1.

As presented in Table 2, of the 153 subjects with pathological CPR, 138 (90.2%) experienced adverse perinatal outcomes, while among the 452 patients with normal CPR, only 44 (9.73%) had adverse perinatal outcomes, which was statistically significant (*P*<.00001).

Table 3 demonstrates that the rates of CS and instrumental deliveries for IFC, NICU admission within 24 hours of delivery, and an APGAR score < 7 at 5 minutes were notably elevated in the group with abnormal CPR compared with those with normal CPR. This was deemed to be statistically significant (*P*<.05).

Table 4 presents the diagnostic precision of pathological CPR in predicting adverse perinatal outcomes, as well as different types of adverse perinatal outcomes. The sensitivity, specificity, PPV, NPV, AUC, and overall diagnostic accuracy of pathological CPR to predict any adverse perinatal outcome were 75.82%, 96.45%, 90.2%, 90.27%, 0.86%, and 90.25%, respectively. Table 4 shows that CPR has high sensitivity, specificity, PPV, NPV, positive LR, AUC-ROC, and overall diagnostic accuracy and low negative LR for predicting any adverse perinatal outcome and also for predicting various adverse perinatal outcomes.

Discussion

Determining which pregnant patients will experience a poor perinatal outcome during labor has always been a challenging task. Therefore, there is a need for a screening tool that can anticipate negative perinatal results beforehand. The CPR, which considers fetal response (MCA PI) and placental perfusion (UA PI), is increasingly being used to efficiently identify at-risk fetuses. The results of

Table 2. Association of Cerebroplacental Ratio with Any Adverse Perinatal Outcome

	NORMAL CEREBROPLACENTAL RATIO (*N* = 452)	PATHOLOGICAL CEREBROPLACENTAL RATIO (*N* = 153)	*P* VALUE
Any adverse perinatal outcome[a] (% of patients)			<.00001[b]
Yes	44 (10)	138 (90)	
No	408 (90)	15 (10)	

[a]*The data are given as the number (%) of patients.*

[b]χ^2 *test.*

Table 3. Association of Cerebroplacental Ratio with Various Adverse Perinatal Outcomes

ADVERSE PERINATAL OUTCOMES	NORMAL CEREBROPLACENTAL RATIO (*N* = 452)	PATHOLOGICAL CEREBROPLACENTAL RATIO (*N* = 153)	*P* VALUE
Cesarean section for [a]intrapartum fetal compromise (% of patients)	24 (5)	105 (70)	<.00001[b]
Instrumental delivery for [a]intrapartum fetal compromise (% of patients)	2 (0.4)	9 (6)	<.001[c]
APGAR score < 7 at 5 minutes[a] (% of patients)	6 (1.3)	33 (22)	<.000001[c]
Admission to neonatal intensive care unit within 24 hours of delivery[a] (% of patients)	18 (4)	66 (44)	<.00001[b]

[a]*The data are given as the number (%) of patients.*

[b]χ^2 *test.*

[c]*Fisher exact test.*

our research show that conducting fetal CPR measurements in term, low-risk AGA pregnancies can predict an unfavorable perinatal outcome.

The present study found that in pregnancies with AGA babies, those with abnormal CPR had significantly higher rates of CS and instrumental delivery compared with those with normal CPR. This finding aligned with Khalil et al,[4] who showed a higher rate of CSs and instrumental deliveries for IFC in AGA pregnancies with poor CPR compared with normal CPR (11.0% vs 8.7%, *P*=.043% and 11.2% vs 7.8%, *P*=.003, respectively).

We found that 44% of the infants in the low-CPR group required NICU hospitalization, in contrast to 4% of those in the normal CPR group (*P*<.05). Flood et al[15] also found that pathological CPR was associated with a higher requirement for infant NICU hospitalization compared with those in the normal CPR group (69.4% vs 22%, *P*<.0001). Prior et al[16] also reported that the pathological group had higher NICU admission rates, but this difference was not statistically significant.

Our study also observed a higher percentage of infants with low APGAR scores in the pathological CPR group; 22% of infants in this group had an APGAR score below 7 at 5 minutes compared with 1.3% of infants in the normal CPR group with an APGAR score below 7 (*P*<.0001). This aligns with findings by Ropacka Lesiak et al[17] and Gramellini et al,[18] who observed a higher incidence of infants with low APGAR scores in the abnormal CPR group. No cases of perinatal mortality were documented in either group in our study.

To summarize, we observed an increased rate of cesarean and instrumental deliveries in pregnancies with pathological CPR compared with normal CPR, as well as higher NICU admission and poorer APGAR scores for infants. This comports with similar findings by Mohamed et al[19] and Anand et al,[20] who reported higher rates of cesarean and instrumental delivery for IFC, NICU admission, and babies with poor APGAR score in term uncomplicated AGA pregnancies with low CPR compared with normal CPR.

The results strongly suggest that negative perinatal outcomes are associated with abnormal CPR in term, low-risk pregnancies. Currently, routine Doppler tests are not recommended for fetuses with normal EFW. A 2010 Cochrane systematic review database suggests there is not enough evidence to show that using fetal Doppler in low-risk term AGA pregnancies can reduce the rates of perinatal morbidity and mortality.[21]

Table 4. Diagnostic Accuracy of Pathological Cerebroplacental Ratio for Predicting Any Adverse Perinatal Outcome

DIAGNOSTIC ACCURACY	ANY ADVERSE PERINATAL OUTCOME	CESAREAN SECTION FOR INTRAPARTUM FETAL COMPROMISE	INSTRUMENTAL DELIVERY FOR INTRAPARTUM FETAL COMPROMISE	APGAR SCORE < 7 AT 5 MINUTES	ADMISSION TO NEONATAL INTENSIVE CARE UNIT WITHIN 24 HOURS OF DELIVERY
Sensitivity (95% CI)	75.82 (68.94-81.85)	81.4 (73.59-87.7)	81.82 (48.22-97.72)	84.62 (69.47-94.14)	78.57 (68.26-86.78)
Specificity (95% CI)	96.45 (94.22-98)	89.92 (73.59-87.2)	75.76 (72.1-79.15)	78.8 (75.2-82.1)	83.3 (79.82-86.4)
Positive predictive value (95% CI)	90.2 (84.75-93.84)	68.63 (62.29-74.33)	5.88 (4.37-7.87)	21.57 (18.26-25.29)	43.14 (37.8-48.6)
Negative predictive value (95% CI)	90.27 (87.75-92.31)	94.69 (92.54-96.24)	99.56 (98.47-99.87)	98.67 (97.26-99.36)	96.02 (94.11-97.32)
Positive likelihood ratio (95% CI)	21.38 (12.92-35.39)	8.07 (6.1-10.69)	3.37 (2.47-4.61)	3.99 (3.24-4.91)	4.7 (3.77-5.87)
Negative likelihood ratio (95% CI)	0.25 (0.19-0.32)	0.21 (0.14-0.3)	0.24 (0.07-0.84)	0.19 (0.09-0.41)	0.26 (0.17-0.39)
Area under receiver operating characteristic curve (95% CI)	0.86 (0.83-0.89)	0.86 (0.83-0.88)	0.79 (0.75-0.82)	0.82 (0.78-0.85)	0.81 (0.78-0.84)
Overall diagnostic accuracy (95% CI)	90.25 (87.6-92.49)	88.1 (85.25-90.57)	75.87 (72.25-79.23)	79.17 (75.72-82.34)	82.65 (79.39-85.58)

Most previous research has focused mainly on the predictive value of CPR for adverse perinatal outcomes in SGA fetuses and high-risk or complicated pregnancies.[15,17,22-25] However, many current studies indicate that AGA fetuses with abnormal CPR are linked to a heightened risk of negative perinatal outcomes.[4,7,16,19,20,26-28] Therefore, it is feasible to include regular, late-third-trimester CPR measurement in routine clinical practice to detect at-risk AGA fetuses who may suffer from placental insufficiency and fail to reach their full genetic potential at term as they may not be identified as high risk through traditional methods such as EFW. Our study adds to the growing body of evidence indicating that abnormal CPR in SGA and AGA pregnancies is a separate indicator of a negative perinatal outcome.

Debate continues regarding the best CPR cut-off value to identify negative perinatal outcomes. Recent research has used percentiles (<5 th or 10th percentile)[7,16,29-31] or multiple of median[32]; on the other hand, earlier studies used absolute values (<1[15,20,28] or <1.08[17,18] or <1.1).[19] Instead of utilizing one specific CPR cut-off value, we determine CPR by considering reference ranges associated with gestational age, as per the latest ISUOG practice guidelines.[14] Our research demonstrated a sensitivity of 75.82%, specificity of 96.45%, PPV of 90.2%, NPV of 90.27%, AUC of 0.86%, and an overall diagnostic accuracy of 90.25% for predicting adverse perinatal outcomes with CPR in the study population. As a result, we believe that CPR using gestational age-specific reference ranges is more strongly linked to adverse perinatal outcome than is a single cut-off value.

Our study suggests CPR measurement should be incorporated into standard practice for term uncomplicated or low-risk AGA pregnancies. This can help identify pregnancies requiring advanced care with facilities for continuous electronic fetal monitoring (EFM), emergency CS, and NICU, in contrast to those with normal CPR that can be managed without such capabilities. Therefore, our study findings align with those of most previous studies that focused on the same important clinical question.

Strengths of the Study

Obstetricians are unaffected by the CPR; thus, the measurement will not impact clinical decision-making regarding delivery. Additionally, based on what we know as of now, few studies have been conducted

on the efficacy of CPR in predicting negative perinatal outcomes in term uncomplicated AGA pregnancies. Of these, most are retrospective in nature.[4,7,26-28] While some prospective studies have been completed,[16,19,20] ours has the largest number of study groups. Furthermore, all the previous prospective studies utilized only one CPR cut-off value, whereas ours utilized the most recent ISUOG guideline for CPR calculation.[14]

Limitations of the Study

Currently, because there are not enough color Doppler facilities in rural areas, many pregnant women in these regions cannot be screened for the CPR. Furthermore, to date there is a lack of properly structured prospective, randomized, controlled trials regarding the efficacy of CPR in predicting negative perinatal outcomes in low-risk, uncomplicated term AGA pregnancies. Hence, before incorporating routine CPR measurement into clinical practice, a well-planned, prospective, randomized, controlled study involving a larger population is needed. Additionally, we did not incorporate umbilical cord blood gas analysis in our study, which may have shown a stronger correlation with negative perinatal outcomes.

Conclusion

Measuring the CPR appears to be a highly encouraging technique for recognizing at-risk fetuses. Owing to the decreasing costs of US machines, measuring the CPR in full-term pregnancies can become a routine clinical practice that can be performed quickly and accurately by a trained medical professional during third-trimester, antepartum evaluations. Through the CPR, at-risk pregnancies can be identified in advance, assisting health care professionals in making more-informed decisions and timely referrals to higher level facilities, ultimately enhancing perinatal results.

Because of the CPR's high sensitivity, specificity, AUC, PPV, NPV, and diagnostic accuracy, women with normal values can likely give birth at local facilities with limited resources as the risk for complications is minimal in such cases. Conversely, women with abnormal CPRs and increased likelihood of complications for their babies can be promptly transferred to a more advanced center with continuous EFM, emergency CS, and NICU capabilities.

References

1) Kuppusamy P, Prusty RK, Kale DP. High-risk pregnancy in india: prevalence and contributing risk factors—a national survey-based analysis. *J Glob Health*. 2023;13(13):04116. doi:10.7189/jogh.13.04116

2) Benzouina S, Boubkraoui ME-M, Mrabet M, et al. Fetal outcome in emergency versus elective cesarean sections at souissi maternity hospital, Rabat, Morocco. *Pan Afr Med J*. 2016;23(23):197. doi:10.11604/pamj.2016.23.197.7401

3) Khalil A, Thilaganathan B. Role of uteroplacental and fetal doppler in identifying fetal growth restriction at term. *Best Pract Res Clin Obstet Gynaecol*. 2017;38:38-47. doi:10.1016/j.bpobgyn.2016.09.003

4) Khalil AA, Morales-Rosello J, Morlando M, et al. Is fetal cerebroplacental ratio an independent predictor of intrapartum fetal compromise and neonatal unit admission?. *Am J Obstet Gynecol*. 2015;213(1):54. doi:10.1016/j.ajog.2014.10.024

5) DeVore GR. The importance of the cerebroplacental ratio in the evaluation of fetal well-being in SGA and AGA fetuses. *Am J Obstet Gynecol*. 2015;213(1):5-15. doi:10.1016/j.ajog.2015.05.024

6) Ebrashy A, Azmy O, Ibrahim M, Waly M, Edris A. Middle cerebral/umbilical artery resistance index ratio as sensitive parameter for fetal well-being and neonatal outcome in patients with preeclampsia: case-control study. *Croat Med J*. 2005;46(5):821-825.

7) Morales-Roselló J, Khalil A, Morlando M, et al. Changes in fetal doppler indices as a marker of failure to reach growth potential at term. *Ultrasound Obstet Gynecol*. 2014;43(3):303-310. doi:10.1002/uog.13319

8) Blencowe H, Cousens S, Jassir FB, et al. National, regional, and worldwide estimates of stillbirth rates in 2015, with trends from 2000: a systematic analysis. *Lancet Glob Health*. 2015;4(2):e98-e108.

9) Low JA, Pickersgill H, Killen H, Derrick EJ. The prediction and prevention of intrapartum fetal asphyxia in term pregnancies. *Am J Obstet Gynecol*. 2001;184(4):724-730. doi:10.1067/mob.2001.111720

10) Bligh LN, Alsolai AA, Greer RM, Kumar S. Cerebroplacental ratio thresholds measured within 2 weeks before birth and risk of cesarean section for intrapartum fetal compromise and adverse neonatal outcome. *Ultrasound in Obstet & Gyne*. 2018;52(3):340-346. doi:10.1002/uog.17542

11) Hadlock FP, Harrist RB, Sharman RS, Deter RL, Park SK. Estimation of fetal weight with the use of head, body, and femur measurements--a prospective study. *Am J Obstet Gynecol*. 1985;151(3):333-337. doi:10.1016/0002-9378(85)90298-4

12) Salomon LJ, Alfirevic Z, Da Silva Costa F, et al. ISUOG practice guidelines: ultrasound assessment of fetal biometry and growth. *Ultrasound Obstet Gynecol*. 2019;53(6):715-723. doi:10.1002/uog.20272

13) Bhide A, Acharya G, Baschat A, et al. ISUOG practice guidelines (updated): use of doppler velocimetry in obstetrics. *Ultrasound Obstet Gynecol*. 2021;58(2):331-339. doi:10.1002/uog.23698

14) Ciobanu A, Wright A, Syngelaki A, et al. Fetal medicine foundation reference ranges for umbilical artery and middle cerebral artery pulsatility index and cerebroplacental ratio. *Ultrasound in Obstet & Gyne*. 2019;53(4):465-472. doi:10.1002/uog.20157

15) Flood K, Unterscheider J, Daly S, et al. The role of brain sparing in the prediction of adverse outcomes in intrauterine growth restriction: results of the multicenter PORTO study. *Am J Obstet Gynecol*. 2014;211(3):288. doi:10.1016/j.ajog.2014.05.008

16) Prior T, Mullins E, Bennett P, Kumar S. Prediction of intrapartum fetal compromise using the cerebroumbilical ratio: a prospective observational study. *Am J Obstet Gynecol*. 2013;208(2):124. doi:10.1016/j.ajog.2012.11.016

17) Ropacka-Lesiak M, Korbelak T, Świder-Musielak J, Breborowicz G. Cerebroplacental ratio in prediction of adverse perinatal outcome and fetal heart rate disturbances in uncomplicated pregnancy at 40 weeks and beyond. *Arch Med Sci*. 2015;11(1):142-148. doi:10.5114/aoms.2015.49204

18) Gramellini D, Folli MC, Raboni S, Vadora E, Merialdi A. Cerebral-umbilical doppler ratio as a predictor of adverse perinatal outcome. *Obstet Gynecol*. 1992;79(3):416-420. doi:10.1097/00006250-199203000-00018

19) Mohamed ML, Mohamed SA, Elshahat AM. Cerebroplacental ratio for prediction of adverse intrapartum and neonatal outcomes in a term uncomplicated pregnancy. *Middle East Fertil Soc J*. 2021;26(1):45. doi:10.1186/s43043-021-00090-3

20) Anand S, Mehrotra S, Singh U, Solanki V, Agarwal S. Study of association of fetal cerebroplacental ratio with adverse perinatal outcome in uncomplicated term AGA pregnancies. *J Obstet Gynaecol India*. 2020;70(6):485-489. doi:10.1007/s13224-020-01357-x

21) Alfirevic Z, Stampalija T, Gyte GM. Fetal and umbilical doppler ultrasound in normal pregnancy. *Cochrane Database Syst Rev*. 2015;4:CD001450.

22) Odibo AO, Riddick C, Pare E, Stamilio DM, Macones GA. Cerebroplacental doppler ratio and adverse perinatal outcomes in intrauterine growth restriction: evaluating the impact of using gestational age-specific reference values. *J Ultrasound Med*. 2005;24(9):1223-1228. doi:10.7863/jum.2005.24.9.1223

23) Bahado-Singh RO, Kovanci E, Jeffres A, et al. The doppler cerebroplacental ratio and perinatal outcome in intrauterine growth restriction. *Am J Obstet Gynecol*. 1999;180(3 pt 1):750-756. doi:10.1016/s0002-9378(99)70283-8

24) Alanwar A, El Nour AA, El Mandooh M, et al. Prognostic accuracy of cerebroplacental ratio for adverse perinatal outcomes in pregnancies complicated with severe pre-eclampsia; a prospective cohort study. *Pregnancy Hypertens*. 2018;14:86-89. doi:10.1016/j.preghy.2018.08.446

25) Malik N, Jain S, Ranjan R, et al. Cerebroplacental ratio as a predictor of perinatal outcome in hypertensive disorders of pregnancy and its comparison with its constituent doppler indices. *Cureus*. 2023;15(12):e49951. doi:10.7759/cureus.49951

26) Mecke L, Ignatov A, Redlich A. The importance of the cerebroplacental ratio for the prognosis of neonatal outcome in AGA fetuses. *Arch Gynecol Obstet*. 2023;307(1):311-317. doi:10.1007/s00404-022-06596-z

27) Ortiz JU, Graupner O, Flechsenhar S, et al. Prognostic value of cerebroplacental ratio in appropriate-for-gestational-age fetuses before induction of labor in late-term pregnancies. *Ultraschall Med*. 2023;44(1):50-55. doi:10.1055/a-1399-8915

28) Singh A, Lnu S, Bano I, Ahmad I. Doppler cerebroplacental ratio and adverse perinatal outcome. *Journal of South Asian Federation of Obstetrics and Gynaecology*. 2014;6(1):25-27. doi:10.5005/jp-journals-10006-1262

29) Berkley E, Chauhan SP, Abuhamad A, Society for Maternal-Fetal Medicine Publications Committee. Doppler assessment of the fetus with intrauterine growth restriction. *Am J Obstet Gynecol*. 2012;206(4):300-308. doi:10.1016/j.ajog.2012.01.022

30) Flatley C, Kumar S. Is the fetal cerebroplacental ratio better that the estimated fetal weight in predicting adverse perinatal outcomes in a low risk cohort?. *Journal of Maternal-Fetal & Neonatal Medicine*. 2019;32(14):2380-2386. doi:10.1080/14767058.2018.1438394

31) Bligh LN, Alsolai AA, Greer RM, Kumar S. Cerebroplacental ratio thresholds measured within 2 weeks before birth and risk of cesarean section for intrapartum fetal compromise and adverse neonatal outcome. *Ultrasound Obstet Gynecol*. 2018;52(3):340-346. doi:10.1002/uog.17542

32) Khalil A, Morales-Rosello J, Khan N, et al. Is cerebroplacental ratio a marker of impaired fetal growth velocity and adverse pregnancy outcome?. *Am J Obstet Gynecol*. 2017;216(6):606. doi:10.1016/j.ajog.2017.02.005

Comparing Diagnostic Efficacy of Contrast-Enhanced US and CTA for Detecting Type 2 Endoleaks: A Comparison with Conventional Angiography and Assessment of Periprocedural Factors

Kamyar Ghabili, MD; Kevin Yiu, DO; Hreedi Dev, BA; Benjamin Shin, MD; Peter Waybill, MD; Kathryn McGillen, MD

Abstract

Objective and Hypothesis: Contrast-enhanced US (CEUS) remains less widely accepted than CTA for endoleak surveillance after endovascular aortic aneurysm repair (EVAR), with type 2 endoleaks being a common early complication. Direct comparisons of CEUS, CTA, and conventional angiography are limited in the United States. We evaluated the diagnostic efficacy of CEUS versus CTA for detecting type 2 endoleaks, using conventional angiography as the reference standard, and assessed procedural factors during endoleak repair in patients with and without preprocedural CEUS. The null hypothesis is that no differences exist in diagnostic accuracy or procedural factors between CEUS and CTA, while the alternative hypothesis anticipates significant differences.

Materials and Methods: This retrospective, single-institution study analyzed patients with suspected type 2 endoleak on CEUS and/or CTA following EVAR who underwent conventional angiography between October 2018 and July 2024. We compared the diagnostic outcomes of CEUS and CTA with conventional angiography and evaluated periprocedural factors such as time from the last contrast-enhanced imaging to angiography, sedation time, contrast dose, and fluoroscopy duration/dose.

Results: The rate of type 2 endoleak detection on conventional angiography was similar between patients with preprocedural CEUS and those with CTA (90% vs 75.5%; $P = .32$). The sensitivity, specificity, positive predictive value (PPV), and negative predictive value (NPV) of CEUS for detecting endoleaks were 100%, 50%, 90%, and 100%, respectively. CTA had sensitivity, specificity, PPV, and NPV of 93.2%, 9.1%, 80.4%, and 25%, respectively. The median time from the last imaging to angiography was significantly shorter for patients with preprocedural CEUS compared with CTA (0 vs 23 days; $P < .001$). Intraprocedural factors (sedation time, contrast dose, and fluoroscopy duration/dose) were not statistically different ($P > .05$).

Conclusions: CEUS was more reliable for ruling out clinically significant type 2 endoleaks and was associated with quicker access to confirmatory angiography than CTA. Sensitivity, endoleak detection rate, and procedural factors were similar between the modalities. These findings suggest CEUS is an equally accurate, yet potentially more efficient, alternative to CTA for EVAR surveillance.

Keywords: contrast-enhanced US, conventional angiography, CTA , endovascular aortic aneurysm repair, type 2 endoleak

Affiliation: Department of Radiology, Penn State Health Milton S. Hershey Medical Center, Hershey, Pennsylvania.
Disclosure: The authors declared no potential conflicts of interest with respect to the research, authorship, and/or publication of this article.
Data sharing statement: Data are available upon reasonable request. All deidentified data are available upon request from the corresponding author KMcG.
Funding: The authors received no financial support for the research, authorship, and/or publication of this article.

Published: February 1, 2025. https://doi.org/10.37549/AR-D-24-0062

Introduction

Endoleaks remain a common complication after endovascular aortic aneurysm repair (EVAR), necessitating follow-up imaging and potential intervention. The most common type of endoleak is type 2, which refers to the enlargement of the aneurysm sac secondary to collateral retrograde flow from a feeding vessel, typically the inferior mesenteric or lumbar arteries.[1] While CTA is widely used for detecting endoleaks, its reliance on radiation and contrast agents presents inherent limitations.[2] Contrast-enhanced US (CEUS) has emerged as a promising alternative, offering real-time imaging without radiation exposure and providing dynamic assessment capabilities that may enhance diagnostic accuracy.[1,3] Existing literature highlights comparable accuracy between CEUS and CTA for detecting endoleaks, including type 2 endoleaks.[4-9] However, the use of CEUS for detecting endoleaks is a relatively recent approach and has not yet gained widespread acceptance for EVAR surveillance, particularly in the United States.[7,10] Therefore, further studies are warranted to establish its efficacy.

Notably, no direct comparison between CEUS, CTA, and conventional angiography has been made to date.[11] This is important as the latter is the imaging modality of choice for diagnosing clinically significant endoleaks that require treatment.[12] Moreover, no study has evaluated whether procedural factors during endoleak repair differ based on whether the diagnosis is made using CEUS or CTA. Therefore, we evaluated the diagnostic efficacy of CEUS compared with CTA in detecting type 2 endoleaks during post-EVAR surveillance. We also determined whether procedural factors during type 2 endoleak repair differed when the diagnosis was based on CEUS versus CTA.

Materials and Methods

Patients

This is a retrospective analysis of all patients with suspected type 2 endoleak on CEUS and/or CTA during routine surveillance after EVAR, who underwent conventional angiography at a tertiary referral center from October 2018 to July 2024. Subjects were included if they underwent conventional angiography by an interventional radiologist after CEUS and/or CTA demonstrated a suspected type 2 endoleak. Patients were excluded if their preprocedural imaging was unavailable in their chart or Picture Archiving and Communication System (PACS), or if endoleaks other than type 2 were suspected on CEUS or CTA. From October 2018 to July 2024, CEUS was performed in 20 cases among 9 patients during routine surveillance after EVAR; type 2 endoleaks were detected in 18 cases. Of those, only 10 subjects underwent conventional angiography and were therefore included in the present study. The institutional review board approved the study and waived the requirement for informed consent.

Contrast-Enhanced US

Grayscale US was initially used to assess the aortic aneurysm sac and locate visible leaks with color Doppler. Subsequently, Lumason (sulfur hexafluoride lipid-type A microspheres, Bracco Diagnostics Inc, Monroe Township, NJ, USA) was administered intravenously, followed by a saline flush. Images were obtained using Siemens or GE US units. The amount of contrast used varied based on the US machine, with newer software requiring less contrast (1 mL followed by a 5 mL saline flush for newer machines, compared with 2.4 mL plus a 5 mL saline flush for older machines). Imaging targeted the sac to confirm the presence of endoleak and evaluate its location to identify potential inflow vessels, such as lumbar arteries or the inferior mesenteric artery.[13,14]

The timing of contrast leak into the aneurysm sac compared with contrast arrival in the stent graft helped distinguish type 2 endoleaks from other types (Figure 1). Type 2 endoleak shows delayed enhancement in the sac through collateral vessels, while type 1 or 3 endoleaks demonstrate simultaneous enhancement in the sac and stent graft lumen.[1]

CTA

CTA of the abdomen and pelvis included a noncontrast CT scan, followed by intravenous administration of iodinated contrast (Omnipaque 350, GE Healthcare Inc, Marlborough, MA, USA). Arterial phase images were acquired using bolus tracking in the aorta, with or without delayed venous phase images obtained 90 seconds after the arterial phase. Multiplanar reconstructions were performed in the coronal and sagittal planes. An endoleak was suspected on CTA when contrast opacification was visualized within the excluded aneurysm sac (Figure 1).

Conventional Angiography

Patients with persistent or recurrent type 2 endoleak and an interval increase in aneurysm sac size of ≥5 mm underwent conventional angiography using the digital subtraction angiography technique for confirmation, followed by transarterial embolization of the feeding vessel(s) upon confirmation of a clinically significant endoleak.[15] Endoleak repair was performed using transarterial coil embolization

Figure 1. (A) Transverse grayscale US image (right) shows a large aneurysm sac with heterogeneous thrombus (green arrow). Transverse contrast-enhanced US image (left) shows contrast enhancement within the aneurysm sac (white arrow), consistent with a type 2 endoleak. (B) Axial delayed-phase CTA shows iodinated contrast opacification within the excluded aneurysm sac (white arrow).

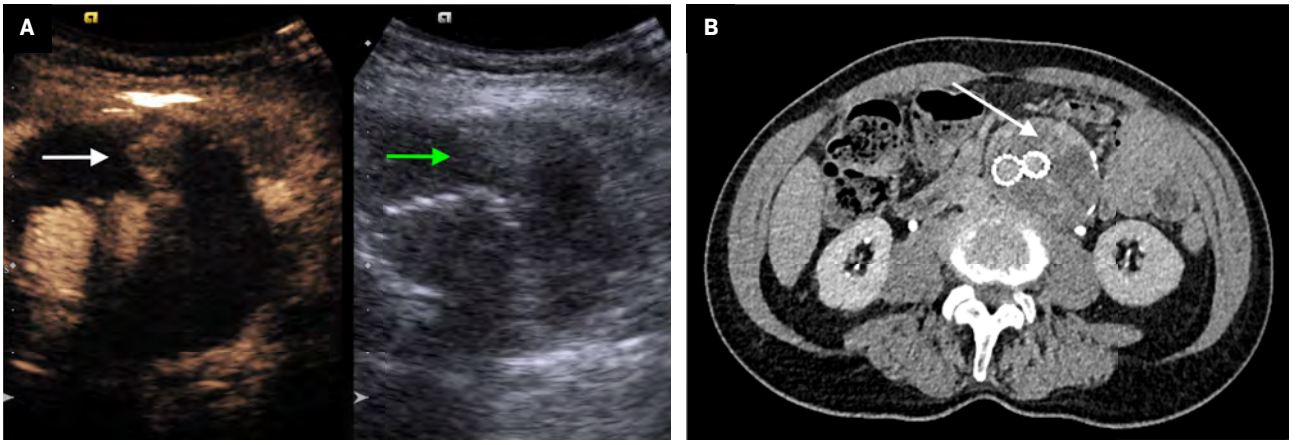

and/or liquid embolic agents such as n-butyl cyanoacrylate or ethylene-vinyl alcohol copolymer. If transarterial embolization was unsuccessful, the patient underwent fluoroscopy-guided direct sac puncture and embolization in a subsequent session.

Study Outcomes

Outcomes of interest included the rate of type 2 endoleak detection on conventional angiography between patients with and without preprocedural CEUS. Additionally, diagnostic performance measures for detecting type 2 endoleaks were calculated for both groups. For this purpose, we included a patient who underwent conventional angiography owing to an interval increase in aneurysm sac size of ≥5 mm without any discrete type 2 endoleak identified on both preprocedural CEUS and CTA . We also included preprocedural CTA scans from patients who underwent CEUS ($n = 10$) in the pool of patients with CTA. This approach was taken to improve the estimation of diagnostic performance of the imaging modalities.

Periprocedural factors, including the time from the last contrast-enhanced imaging (either CEUS or CTA) to conventional angiography, sedation time, contrast dose, and fluoroscopy duration and dose, were also evaluated between patients with and without CEUS prior to conventional angiography.

Statistical Analysis

Continuous variables were reported as median and interquartile range (IQR). Categorical variables were presented as counts and proportions (%). *P* values were determined using the Mann-Whitney test for continuous variables and Fisher's exact test for categorical variables. Diagnostic performance metrics for detecting type 2 endoleaks included sensitivity, specificity, positive predictive value (PPV), negative predictive value (NPV), and accuracy. Statistical analyses were performed using IBM SPSS Statistics for Windows, version 29.0.0 (IBM Corp, Armonk, NY, USA). A P value < .05 was considered statistically significant.

Results

A total of 48 patients, 43 males and 5 females, with suspected type 2 endoleak on CEUS and/or CTA underwent 55 conventional angiography procedures for confirmation and endovascular repair of the endoleak. The median age of patients at the time of conventional angiography was 79 years (IQR: 76-86 years). CEUS detected type 2 endoleaks in 10 cases, with CTA performed prior to CEUS in 9 cases, suggesting type 2 endoleaks in 6 (66.7%) cases and no endoleaks in 3 (33.3%) cases. The median time between CEUS and CTA was 27 days (IQR: 10-28 days).

Conventional angiography confirmed type 2 endoleaks in 9 of 10 CEUS-detected cases (90%), while 1 showed no endoleaks (10%). Of the 45 CTA studies with suspicion for type 2 endoleak, conventional angiography confirmed type 2 endoleaks in 34 cases (75.5%), identified other endoleak types in 2 cases (4.5%), and revealed no endoleak in 9 cases (20%). The rate of type 2 endoleak detection on conventional angiography was similar between patients with and without preprocedural CEUS (90% vs 75.5%; $P = .32$).

To measure diagnostic performance metrics, we included a patient who underwent conventional angiography without a type 2 endoleak detected on both CEUS and CTA. For the CTA group, metrics were calculated for 55 patients,

Figure 2. Sankey diagram illustrating the distribution of cases with type 2 endoleaks detected on contrast-enhanced US (A) or CTA (B), along with subsequent confirmatory conventional angiography using the digital subtraction angiography technique. The numbers on the labels indicate the number of patients.

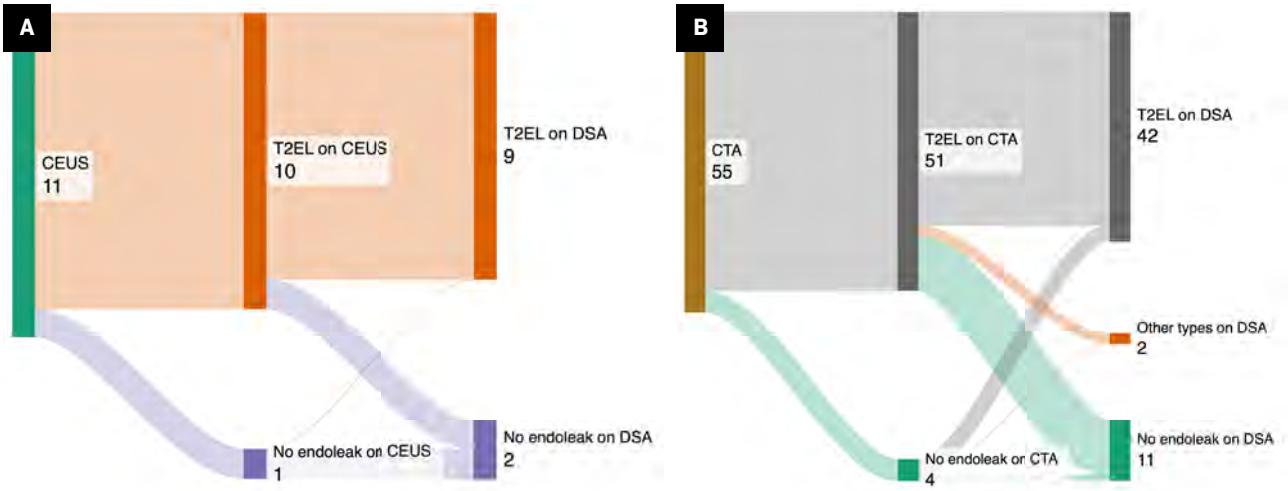

including 10 who underwent CTA and CEUS and 45 who underwent CTA only (Figure 2). The sensitivity, specificity, PPV, NPV, and accuracy of CEUS for detecting endoleaks were 100%, 50%, 90%, 100%, and 90.9%, respectively. The sensitivity, specificity, PPV, NPV, and accuracy of CTA were 93.2%, 9.1%, 80.4%, 25%, and 76.4%, respectively (Table 1).

Periprocedural factors for patients with and without CEUS prior to conventional angiography are listed in Table 2. The median time from the last contrast-enhanced imaging (either CEUS or CTA) to conventional angiography was significantly shorter for patients with preprocedural CEUS (0 days; IQR: 0-15.2 days) compared with those with CTA only (23 days; IQR 13-52 days) ($P <$ .001, Table 2). In 7 of 10 patients with CEUS-detected type 2 endoleaks, imaging for detection and conventional angiography for repair were performed on the same day compared with 3 of 45 patients with CTA-detected endoleaks (70% vs 6.7%, $P <$ .001). Intraprocedural factors, including sedation time, contrast dose, and fluoroscopy duration and dose, were not statistically different between the 2 groups ($P >$ .05, Table 2).

Discussion

The present study showed that the type 2 endoleak detection rate on conventional angiography was similar between CEUS and CTA. However, CEUS demonstrated higher specificity and NPV compared with CTA, suggesting that CEUS is more reliable for ruling out clinically significant type 2 endoleaks. Additionally, patients with endoleaks detected on CEUS underwent confirmatory conventional angiography in a shorter timeframe compared with those with CTA-detected endoleaks. To our knowledge, no previously published studies have investigated the diagnostic efficacy of CEUS versus CTA for detecting type 2 endoleaks using conventional angiography as the gold standard, nor have any studies evaluated periprocedural factors between the 2 modalities.

In our study, CEUS and CTA demonstrated comparable detection rates (90% vs 75.5%), sensitivity (100% vs 93.2%), and PPV (90% vs 80.4%) for type 2 endoleaks. However, CEUS outperformed CTA in specificity (50% vs 9.1%) and NPV (100% vs 25%). A recent systematic review of 5214 patients in 38 studies similarly reported pooled detection rates for all endoleak types of 96.67% (95% CI: 88.72-100%) for CEUS and 92.82% (95% CI: 77.39-100%) for CTA.[8] Previous meta-analysis on CEUS versus CTA for all endoleaks found pooled sensitivity and specificity of 94% (95% CI: 89-97%) and 93% (95% CI: 89%-96%), respectively.[7]

Notably, one recent meta-analysis specifically evaluated CEUS versus CTA for detecting type 2 endoleaks.[5] The included studies reported sensitivity ranging from 50% to 100% and specificity from 55% to 95%, with pooled sensitivity and specificity of 91% (95% CI: 87-95%) and 78% (95% CI: 74-82%), respectively.[5] The authors attributed the lower specificity to either a high number of false positives or to the use of CTA, which may have inaccurately diagnosed some type 2 endoleaks as the reference standard in those studies.[5] In our study, where conventional angiography was used as the reference standard, CEUS and CTA demonstrated specificity of 50% (95% CI: 1.3-98.7%) and 9.1% (95% CI: 0.2-41.3%), respectively. While

Table 1. Diagnostic Performance of Contrast-Enhanced US Versus CTA in Detecting Type 2 Endoleaks: Percentage (95% Confidence Interval)

METRIC	CONTRAST-ENHANCED US	CTA
Sensitivity	100% (66.4-100%)	93.2% (81.3-98.6%)
Specificity	50% (1.3-98.7%)	9.1% (0.2-41.3%)
Positive predictive value	90% (69.2-97.3%)	80.4% (77-83.4%)
Negative predictive value	100% (2.5-100%)	25% (3.7-74.4%)
Accuracy	90.9% (58.7-99.8%)	76.4% (63-87%)

Abbreviations: CTA, computed tomography angiography.

Table 2. Periprocedural Factors Between Patients With and Without Contrast-Enhanced US Prior to Conventional Angiography: Median Interquartile Range (IQR).

VARIABLE	CONTRAST-ENHANCED US (*N* = 10)	CTA (*N* = 45)	*P* value
Aneurysm size change, cm	10.5 (3.7-17.1)	6.1 (1.5-11.1)	.25
Time from last contrast-enhanced image to conventional angiography, days	0 (0-15.2)	23 (13-52)	<.001
Sedation time, minutes	120 (85-168.7)	120 (92.5-148)	.76
Contrast dose, mL	85 (55-121.2)	90 (70-125)	.44
Fluoroscopy time, minutes	42 (28.6-59.2)	32.7 (24.5-47.5)	.37
Fluoroscopy dose, mGy	3695.5 (2731-4796.2)	3091 (1543.2-4422.5)	.40

Abbreviations: CTA, computed tomography angiography.

CEUS showed higher specificity than CTA, the lower-than-expected values and wide CIs could be attributed to the small sample size. Nevertheless, the observed trend aligns with the published meta-analysis, confirming superior diagnostic performance of CEUS compared with CTA in terms of specificity.

The reported NPV for CEUS, compared with CTA (as the standard reference), in detecting all types of endoleaks ranges from 92.86% to 100%.[16-18] Similarly, we found a significantly higher NPV for CEUS compared with CTA (100% vs 25%). This finding further supports CEUS as a valuable modality for ruling out clinically significant type 2 endoleaks without requiring concurrent CTA or additional invasive procedures. In contrast, the low NPV of CTA may result in unnecessary follow-up procedures or interventions owing to the procedure's high false-positive rate.[19]

The current literature lacks evaluation of whether procedural factors during endoleak repair differ based on diagnoses made using CEUS or those made using CTA. In the present study, we found no significant differences in intraprocedural sedation time, contrast dose, fluoroscopy duration, and fluoroscopy dose between patients whose type 2 endoleak was detected by CEUS versus CTA. In contrast, CEUS detection of type 2 endoleak was associated with a shorter time to conventional angiography in our study. The majority of patients with CEUS-detected type 2 endoleaks (70%) underwent conventional angiography for endoleak repair on the same day as the preprocedural imaging compared with a small proportion of patients with CTA-detected endoleaks (6.7%). This was possible because the radiologist performed and interpreted CEUS in near real time for the interventional radiologist. Additionally, there was no concern about administering a "double dose" of iodinated contrast, which typically requires temporal separation between CTA and conventional angiography.

Our study has several limitations. First, it was conducted at a single institution with a retrospective design. Second, the study included a small number of patients whose type 2 endoleak was detected on CEUS and who subsequently underwent conventional angiography, necessitating confirmation of these findings through a larger, multi-institutional study.

However, CEUS has been an uncommon modality for surveillance after EVAR, as evidenced by the 20 cases among 9 patients, with only 10 cases undergoing conventional angiography over the 6-year period in the present study. Moreover, owing to the small number of patients who underwent both CEUS and CTA (n = 9), further statistical measures of agreement, such as Cohen kappa coefficient and McNemar tests, could not be performed between CEUS and CTA pairs. Finally, the diagnostic efficacy of CEUS was compared with a historical control group of patients with suspicious type 2

endoleaks identified on CTA. This comparison may introduce potential selection or temporal biases. Despite these limitations, our study provides a unique comparison between CEUS and CTA using conventional angiography as the gold standard. Furthermore, all CEUS procedures were performed and interpreted by a single radiologist (KM, with 7 years of experience), minimizing interobserver variability in this study.

Conclusion

CEUS demonstrated a significantly higher NPV than CTA, making it more reliable for ruling out clinically significant type 2 endoleaks. Furthermore, patients with type 2 endoleaks detected on CEUS underwent confirmatory conventional angiography in a shorter timeframe compared with those with CTA-detected endoleaks. Detection rates, sensitivity, and procedural factors were similar between the 2 modalities. These findings suggest that CEUS is not only equally accurate as, but also a potentially more efficient alternative to, CTA for post-EVAR surveillance.

References

1) Alexander LF, Overfield CJ, Sella DM, et al. Contrast-enhanced US evaluation of endoleaks after endovascular stent repair of abdominal aortic aneurysm. *Radiographics*. 2022;42(6):1758-1775. doi:10.1148/rg.220046

2) Smith L, Thomas N, Arnold A, et al. Editor's choice—a comparison of computed tomography angiography and colour duplex ultrasound surveillance post infrarenal endovascular aortic aneurysm repair: financial implications and impact of different international surveillance guidelines. *Eur J Vasc Endovasc Surg*. 2021;62(2):193-201. doi:10.1016/j.ejvs.2021.04.005

3) Gilabert R, Buñesch L, Real MI, et al. Evaluation of abdominal aortic aneurysm after endovascular repair: prospective validation of contrast-enhanced US with a second-generation US contrast agent. *Radiology*. 2012;264(1):269-277. doi:10.1148/radiol.12111528

4) Abraha I, Luchetta ML, De Florio R, et al. Ultrasonography for endoleak detection after endoluminal abdominal aortic aneurysm repair. *Cochrane Database Syst Rev*. 2017;6(6):CD010296. doi:10.1002/14651858.CD010296.pub2

5) Chung J, Kordzadeh A, Prionidis I, Panayiotopoulos Y, Browne T. Contrast-Enhanced UltraSound (CEUS) versus Computed Tomography Angiography (CTA) in detection of endoleaks in post-EVAR patients. are delayed type II endoleaks being missed? A systematic review and meta-analysis. *J Ultrasound*. 2015;18(2):91-99. doi:10.1007/s40477-014-0154-x

6) Harky A, Zywicka E, Santoro G, et al. Is Contrast-Enhanced UltraSound (CEUS) superior to Computed Tomography Angiography (CTA) in detection of endoleaks in post-EVAR patients? A systematic review and meta-analysis. *J Ultrasound*. 2019;22(1):65-75. doi:10.1007/s40477-019-00364-7

7) Kapetanios D, Kontopodis N, Mavridis D, et al. Meta-analysis of the accuracy of contrast-enhanced ultrasound for the detection of endoleak after endovascular aneurysm repair. *J Vasc Surg*. 2019;69(1):280-294. doi:10.1016/j.jvs.2018.07.044

8) Karaolanis GI, Antonopoulos CN, Georgakarakos E, et al. Colour duplex and/or contrast-enhanced ultrasound compared with computed tomography angiography for endoleak detection after endovascular abdominal aortic aneurysm repair: a systematic review and meta-analysis. *J Clin Med*. 2022;11(13):3628. doi:10.3390/jcm11133628

9) Mirza TA, Karthikesalingam A, Jackson D, et al. Duplex ultrasound and contrast-enhanced ultrasound versus computed tomography for the detection of endoleak after EVAR: systematic review and bivariate meta-analysis. *Eur J Vasc Endovasc Surg*. 2010;39(4):418-428. doi:10.1016/j.ejvs.2010.01.001

10) Barmparessos E, Stenson K, Holt P. Pros and cons of contrast-enhanced ultrasound in endovascular aneurysm repair surveillance. *HJVES*. 2023;5(3):89-98. doi:10.59037/gbgm4v65

11) Morell-Hofert D, Gruber L, Gruber H, et al. Contrast-enhanced ultrasound after endovascular aortic repair: supplement and potential substitute for CT in early- and long-term follow-up. *Ann Vasc Surg*. 2024;102:9-16. doi:10.1016/j.avsg.2023.11.040

12) Chen JX, Stavropoulos SW. Type 2 endoleak management. *Semin Intervent Radiol*. 2020;37(4):365-370. doi:10.1055/s-0040-1715873

13) Cruz JC, McGillen KL, Pryor W, Esslinger D, Shin B. Novel use of contrast-enhanced ultrasound in the pretreatment planning prior to endovascular repair of endoleak after endovascular aortic aneurysm repair in a patient with chronic renal insufficiency: a case report and literature review. *J Med Ultrasound*. 2022;30(1):54-58. doi:10.4103/JMU.JMU_173_20

14) McGillen K, Aljabban N, Wu R, et al. Addition of contrast in ultrasound screening for hepatocellular carcinoma. *Res Diagn Interv Imaging*. 2024;9:100039. doi:10.1016/j.redii.2023.100039

15) Chaikof EL, Dalman RL, Eskandari MK, et al. The society for vascular surgery practice guidelines on the care of patients with an abdominal aortic aneurysm. *J Vasc Surg*. 2018;67(1):2-77. doi:10.1016/j.jvs.2017.10.044

16) Abbas A, Hansrani V, Sedgwick N, Ghosh J, McCollum CN. 3D contrast enhanced ultrasound for detecting endoleak following EndoVascular Aneurysm Repair (EVAR). *Eur J Vasc Endovasc Surg*. 2014;47(5):487-492. doi:10.1016/j.ejvs.2014.02.002

17) Bredahl KK, Taudorf M, Lönn L, et al. Contrast enhanced ultrasound can replace computed tomography angiography for surveillance after endovascular aortic aneurysm repair. *Eur J Vasc Endovasc Surg*. 2016;52(6):729-734. doi:10.1016/j.ejvs.2016.07.007

18) Curti M, Piacentino F, Fontana F, et al. EVAR follow-up with ultrasound Superb Microvascular Imaging (SMI) compared to CEUS and CT angiography for detection of type II endoleak. *Diagnostics*. 2022;12(2):526. doi:10.3390/diagnostics12020526

19) Guo Q, Zhao J, Huang B, et al. A systematic review of ultrasound or magnetic resonance imaging compared with computed tomography for endoleak detection and aneurysm diameter measurement after endovascular aneurysm repair. *J Endovasc Ther*. 2016;23(6):936-943. doi:10.1177/1526602816664878

Pleural Fluid Volume Estimates and the Actual Volume: A Cross-Sectional Analysis

Luis Lorenzo A. Chan, MD; Jose Gil Archie V. Causing, MD; Katleya Teresa G. Manlapaz, MD

Abstract

Objective and Hypothesis: This study aims to compare the accuracy of 5 ultrasonographic formulae commonly used to estimate pleural effusion volume against actual volumes drained via thoracentesis in noncritically ill patients. We hypothesized that some formulae would yield more accurate estimations.

Materials and Methods: A cross-sectional analytic study was conducted at St. Luke's Medical Center, Quezon City, the Philippines, from January 2022 to December 2022. Adult patients with pleural effusion who underwent chest US within 72 hours prior to thoracentesis were included. Five US formulae—Goecke and Schwerk (GS1 and GS2), Eibenberger, Balik, and conventional ellipsoid volume—were applied to estimate pleural fluid volume. The volume estimates were compared with the actual volume of fluid drained during thoracentesis. Intraclass correlation coefficients (ICCs) were used to measure agreement between the estimated and actual volumes.

Results: The study included 61 patients with a mean age of 67.19 years. The mean volume aspirated was 644.51 mL. The Balik formula exhibited the highest ICC (0.793), indicating the strongest agreement with actual volumes. The conventional ellipsoid volume formula and GS2 also showed good agreement, with ICCs of 0.773 and 0.756, respectively. GS1 and Eibenberger formulae demonstrated moderate accuracy with ICCs of 0.556 and 0.612, respectively.

Conclusion: The Balik, conventional ellipsoid volume, and GS2 formulae provided more accurate pleural fluid volume estimations. Accurate volume estimation is crucial for clinical decision-making, and these findings emphasize the importance of selecting appropriate formulae for ultrasonographic evaluation. Further research is needed to validate these results and explore factors affecting estimation accuracy.

Keywords: pleural effusion, chest US, pleural fluid volume, thoracentesis accuracy, sonographic estimation

Introduction

Pleural effusion is defined as an excessive accumulation of fluid in the pleural space resulting from excess fluid production, decreased absorption, or both.[1] About 1-10 mL of fluid is normally present in the pleural space.[1-5] The daily production of pleural fluid is about 10 mL, which is absorbed continuously.[2] The balance between the hydrostatic and oncotic forces in the pleural vessels of the visceral and parietal pleura and the surrounding lymphatic drainage maintains the normal volume of fluid in the pleural space.[1,3] Pleural effusion results when this equilibrium is disrupted, and it is most associated with heart failure, pneumonia, cancer, pulmonary embolism, viral disease, coronary artery bypass surgery, and cirrhosis with ascites.[5,6]

The use of US in examining the pleural space has become a standard practice worldwide.[7]

Affiliation: St. Luke's Medical Center, Institute of Radiology, Quezon City, The Philippines.
Disclosures: The authors have no conflicts of interest to disclose. None of the authors received outside funding for the production of this original manuscript and no part of this article has been previously published elsewhere.
Data Availability Statement: Data available upon reasonable request. The deidentified participant data and additional protocols can be obtained from Luis Lorenzo A. Chan, MD (llachan@stlukes.com.ph) under conditions of appropriate reuse. No public repository is used for this data.

Published: February 1, 2025. https://doi.org/10.37549/AR-D-24-0063

Compared with radiography and CT, US has the advantage of being noninvasive, cost-effective, readily available, and repeatable. It is also safer because no ionizing radiation is used. Furthermore, chest US demonstrates better sensitivity and reliability than the other 2 modalities.[8-10] While at least 150 mL is required to detect effusion by radiography in the standing position, effusions as small as 5 mL can be detected sonographically.[2,11] In addition, chest CT has difficulty distinguishing small effusions from pleural thickening, dependent atelectasis, or tumor, which lowers its sensitivity in quantifying pleural effusion.[6]

Pleural effusion is typically managed by drainage; thoracentesis is one frequently used method. Owing to discrepancies between the actual volume of pleural effusion with the clinical picture of the patient, clinicians often have difficulty determining whether to drain the pleural fluid.[8]

To this end, various formulae have been devised to estimate the volume of pleural effusion with US.[9,12-16] Goecke and Schwerk proposed the first equation in 1990; 2 popular variants of their formula are used worldwide.[12] The first, GS1, uses the lateral height of the effusion wherein one caliper is placed at the costophrenic angle, and a second caliper is placed at the lung base. The formula is as follows:

$$\text{Pleural effusion volume (mL)} = \text{lateral height (cm)} \times 90$$

The second formula, GS2, utilizes the subpulmonary height and the lateral height of the pleural effusion. The subpulmonary height is obtained by placing one caliper at the lung base and the other caliper at the mid-diaphragm. The formula is as follows:

$$\text{Pleural effusion volume (mL)} = (\text{subpulmonary height} + \text{lateral height})\,\text{(cm)} \times 70$$

A third equation was proposed by Eibenberger and colleagues in 1994.[9] This formula was found to estimate pleural fluid volume more accurately in patients with larger fluid volumes. Volume is obtained by measuring the perpendicular distance between the visceral and parietal pleura, where the calipers are placed at the lung margin and posterior chest wall. The formula is

$$\text{Pleural effusion volume (mL)} = (47.6 \times \text{distance between both pleura}) - 837$$

In 2006, a fourth equation was proposed by Balik and colleagues.[13,14] Like the Eibenberger formula, this equation utilizes the distance between the visceral and parietal pleura to estimate fluid volume. However, the Balik formula is better suited for estimating thinner pleural volumes. The Balik formula is

$$\text{Pleural effusion volume (mL)} = \text{distance between both pleura} \times 20$$

Our institution most often uses a fifth equation known as the conventional ellipsoid volume formula. In addition to the pleural cavity, this formula can be used to measure the volume of various organs such as the spleen or prostate.[15,16] The formula is:

$$\text{Pleural effusion volume (mL)} = \text{length} \times \text{width} \times \text{height (cm)} \times 0.52$$

All 5 of these formulae, summarized in the accompanying chart, are simple, accurate, and easy to perform quickly. In previous studies using these formulae, the acceptable margin of error was set at 5% to define their accuracy.[7,8] However, there remains no consensus among radiologists on which of these should serve as the standard formula. This study aims to determine which of these quantitative US formulae best estimates pleural effusion volume.

METHODS	EQUATION
Goecke and Schwerk (GS1)	H × 90
Goecke and Schwerk (GS2)	(H+D) × 70
Balik et al	C × 20
Eibenberger et al	(C × 47.6) – 837
Conventional ellipsoid volume formula	L × W × H × 0.52

Materials and Methods

This is a cross-sectional analytic study. The target population includes adult patients with pleural effusion who were not mechanically ventilated, had undergone chest US prior to thoracentesis and were admitted to St. Luke's Medical Center, Quezon City, the Philippines, from January 1, 2022, to December 31, 2022. Patients were included in the study if they were able to comply with standard positioning for chest US and underwent the procedure without mechanical ventilation less than 72 hours prior to thoracentesis. Total to near-total drainage of pleural fluid also must have been achieved during thoracentesis (Figure 1) as indicated by data on the operative technique.[7,8]

Patients excluded from the study were those with a diagnosis of loculated pleural effusions or empyema on imaging; low-volume

Figure 1. Pre-thoracentesis (A) and post-thoracentesis (B) US images of the same patient taken 2 days apart showing near-total drainage of pleural fluid during thoracentesis.

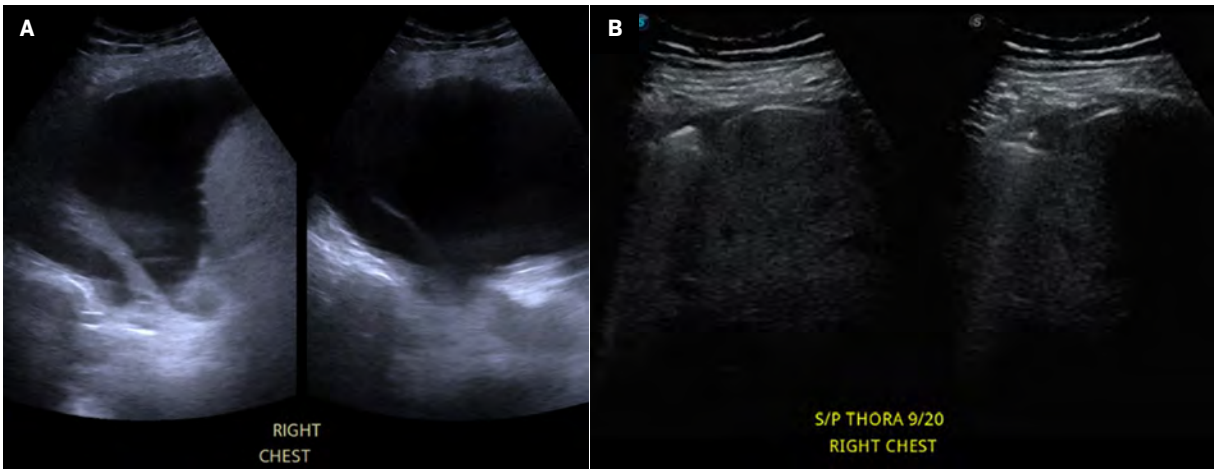

pleural effusion (<500 mL); thoracic deformities, diaphragmatic pathology, or previous chest surgeries. Those who had undergone other surgical drainage interventions, for example, chest pigtail insertion, and those with missing data or images were also excluded from the study. All images of the participants were given a code by the investigator.

Image Evaluation

Low-frequency chest US was performed by radiologic technologists using a low-frequency probe with Siemens, Hitachi, and Sonoscape portable US machines. Patients were asked to maintain standard chest US positioning; that is, an angled supine position with their arms folded across the chest to displace the scapulae.[17] The posterior chest was scanned through the intercostal spaces and the following measurements were obtained: the subpulmonary height in centimeters of the effusion from the lung base to the mid-diaphragm; the maximum perpendicular distance in millimeters between the pulmonary surface and chest wall; and the maximum length, width, and height in centimeters of the pleural effusion.

The results were plotted in the equations for estimating pleural effusion, where D is the subpulmonary height of the effusion in centimeters from the lung base to the mid-diaphragm, C is the maximum perpendicular distance in millimeters between the parietal and visceral pleura, and L, W, and H are the maximum length, width, and height of the pleural effusion in centimeters (Figure 2).

Data Analysis

Demographic data, measurements of pleural fluid volume, laterality of pleural fluid volume, and the total volume of fluid drained from official operative technique were gathered from Carestream picture archiving and communication system, MD Portal, and patient chart review.

Summary statistics are presented (Tables 1–3), with reported means and SDs for quantitative data and frequency distributions for categorical information. This study uses the intraclass correlation coefficient (ICC) to measure the degree of agreement between the volume estimation of each equation with the actual aspirated volume. The ICC is used to assess the reliability of a given instrument to measure the parameter for which it is intended. The results are compared with the actual volume aspirated using ICC. The level of agreement is defined as follows:

- Poor agreement: ICC < 0.5.
- Moderate agreement: ICC 0.5-0.75.
- Good agreement: ICC 0.75-0.9.
- Excellent agreement: ICC > 0.9.

Processing and analysis were performed using Windows SPSS version 19.

Results

The study included 61 patients with a mean age of 67.19 (±17), with nearly equal male-female distribution (52.5% male, 47.5% female). The mean volume aspirated was 644.51 mL (min 500 mL, max 1400 mL). There was likewise an almost equal

Figure 2. Measurements obtained in a chest US of a patient with pleural effusion (A, B), showing distance between parietal and visceral pleura (C), subpulmonary height (D), maximum length (L), maximum width (W), and maximum height (H).

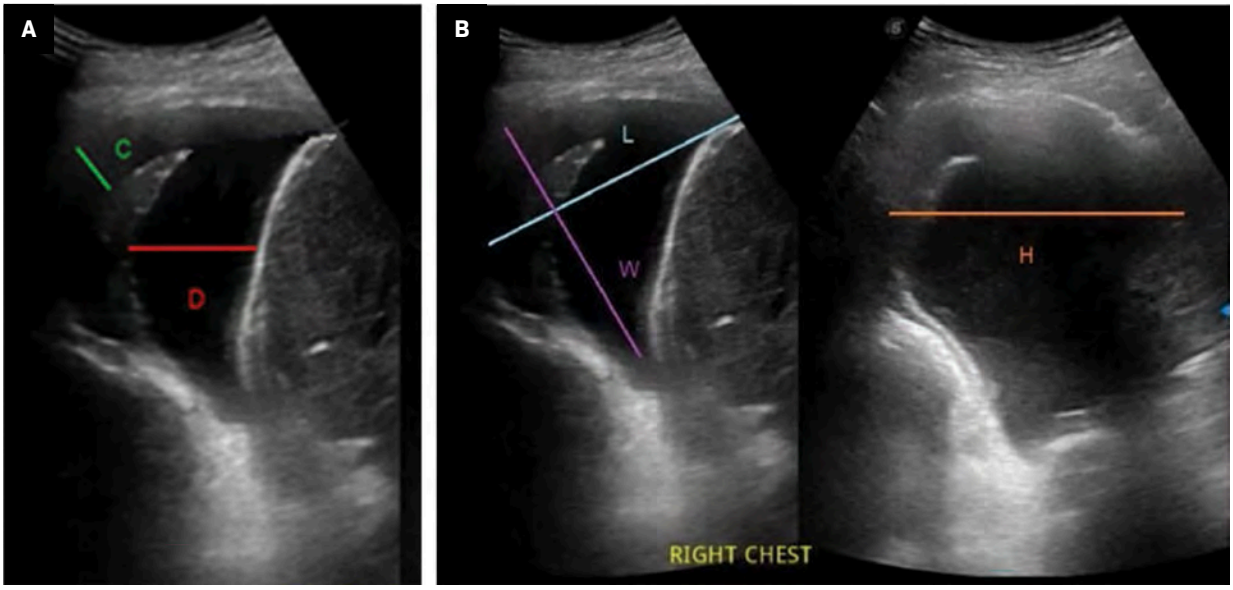

laterality-specific distribution (54% right, 46% left). The mean volume aspirate on the right was 659.85 mL (min 500 mL, max 1300 mL), and 626.43 mL on the left (min 500 mL, max 1400 mL).

Good agreement was noted for the GS2, Balik, and conventional ellipsoid volume formulae, with the Balik formula exhibiting the highest ICC among the 3 equations. Moderate ICC was noted for the GS1 and Eibenberger formulae.

The GS2 and conventional ellipsoid formulae consistently showed good ICC values regardless of laterality. The Balik formula showed moderate ICC in estimating right-sided pleural fluid volume but excellent estimation on the left side. The Eibenberger formula showed moderate ICC in estimating left- and right-sided pleural effusion. The GS1 formula demonstrated moderate estimation capability on right-sided pleural fluid but poor ICC values on the left-sided pleural fluid volume.

Discussion

The successful management of pleural effusion hinges on its prompt identification, accurate estimation of fluid volume, and determination of its cause.[8] Clinically diagnosing pleural effusion is challenging, especially in minor cases and in the presence of concurrent lung consolidation, thus requiring radiologic confirmation.

The assessment of these 5 formulae was centered around their simplicity and speed of application, making them particularly advantageous for routine clinical utilization.[8] Other US formulae documented in the literature often prove to be complex, time consuming, and unsuitable for everyday clinical practice.

Our study revealed varying degrees of correlation between the estimated and actual volumes across the different formulae. Balik, GS2, and the conventional ellipsoid volume formulae demonstrated the highest ICC values, indicating a stronger agreement between the estimated and actual volumes compared with the other formulae. A previous study concluded that the GS2 and Balik formulae yielded good pleural effusion volume estimates, showing a correlation coefficient (r) of 0.81 and 0.63, respectively.[8] Previous studies concluded that the GS2 formula yields a strong correlation with actual volume by taking advantage of the fact that nonloculated pleural fluid descends to the lower pleural space with the patient in the standing position.[8,18]

While previous studies have reported suboptimal correlation

Table 1. Mean Age, Sex, and Volume Aspirated in mL

Age	67.19 (±17)
Sex, *n*, %	
Male	32 (52.5)
Female	29 (47.5)
Volume aspirated	644.51 (±261.58)
Right	659.85 (±276.81)
Left	626.43 (±246.20)

Table 2. Intraclass Correlation Coefficient for the 5 Equations Against Measured Volume

	INTRACLASS CORRELATION COEFFICIENT	95% CONFIDENCE INTERVAL	
		UPPER LIMIT	LOWER LIMIT
Goecke and Schwerk (GS1)	0.556	0.260	0.734
Goecke and Schwerk (GS2)	0.756	0.594	0.854
Balik	0.793	0.655	0.876
Eibenberger	0.612	0.353	0.767
Conventional ellipsoid volume formula	0.773	0.622	0.864

Table 3. Laterality-Specific Intraclass Correlation Coefficient for the 5 Equations Against Measured Volume

EQUATION	RIGHT			LEFT		
	95% CI					
	INTRACLASS CORRELATION COEFFICIENT	UPPER LIMIT	LOWER LIMIT	INTRACLASS CORRELATION COEFFICIENT	UPPER LIMIT	LOWER LIMIT
Goecke and Schwerk (GS1)	0.630	0.251	0.817	0.466	-0.153	0.753
Goecke and Schwerk (GS2)	0.757	0.509	0.880	0.771	0.505	0.894
Balik	0.665	0.322	0.835	0.895	0.773	0.951
Eibenberger	0.561	0.112	0.783	0.647	0.239	0.837
Conventional ellipsoid volume formula	0.778	0.551	0.891	0.761	0.483	0.889

coefficients of the Balik formula, its application in our study yielded a good ICC performance, likely due to its focus on estimating mid- to large-volume pleural effusions, which is similar to the methods and volume ranges assessed in our study.[13] In contrast, other studies applied the formula to a more varied volume range, potentially contributing to its poorer performance in those contexts.[7,8]

The GS1 and Eibenberger formulae exhibited relatively lower ICC values, suggesting poorer accuracy in estimating pleural fluid volume. Previous evidence demonstrated that the primary drawback of the GS1 formula is its tendency to overestimate the volume of minor effusions.[18] Meanwhile, the Eibenberger formula demonstrates a propensity to underestimate pleural fluid volume in individuals with larger thoracic/pleural cavities and overestimate it in those with smaller cavities.[9]

In studying laterality-specific US estimation of pleural effusion volume across the various equations, we found that the GS2 and conventional ellipsoid formulae displayed consistently good correlation coefficients. This is despite findings by Hassan et al that GS2 tends to overestimate effusion on the left side since the left hemithorax is smaller than the right.[7] Meanwhile, the Balik formula demonstrated an even better ICC value on the left side and maintained a good ICC value on the right, which can be attributed to its similarity to the GS2 method. These findings highlight the importance of selecting an appropriate formula to accurately estimate pleural fluid volume and guide clinical decision-making.

Conclusion

This study compared the accuracy of 5 formulae in estimating pleural fluid volume compared with the actual volume drained via thoracentesis. The findings suggest that the Balik, conventional ellipsoid volume, and the GS2 formulae offer more accurate pleural fluid volume estimations compared with the GS1 and Eibenberger formulae.

By emphasizing the importance of selecting an appropriate formula to guide clinical decision-making in patients with pleural effusion, these findings have important implications for clinical practice. Further research is warranted to validate these

findings and explore additional factors influencing the accuracy of pleural fluid volume estimation.

References

1) Diaz-Guzman E, Dweik RA. Diagnosis and management of pleural effusions: a practical approach. *Compr Ther*. 2007;33(4):237-246. doi:10.1007/s12019-007-8016-5

2) Müller NL. Imaging of the pleura. *Radiology*. 1993;186(2):297-309. doi:10.1148/radiology.186.2.8421723

3) Noppen M. Normal volume and cellular contents of pleural fluid. *Curr Opin Pulm Med*. 2001;7(4):180-182. doi:10.1097/00063198-200107000-00002

4) Na MJ. Diagnostic tools of pleural effusion. *Tuberc Respir Dis (Seoul)*. 2014;76(5):199-210. doi:10.4046/trd.2014.76.5.199

5) Light RW. *Pleural Diseases*. 6th ed. Lippincott Williams & Wilkins; 2013.

6) Soni NJ, Franco R, Velez MI, et al. Ultrasound in the diagnosis and management of pleural effusions. *J Hosp Med*. 2015;10(12):811-816. doi:10.1002/jhm.2434

7) Hassan M, Rizk R, Essam H, Abouelnour A. Validation of equations for pleural effusion volume estimation by ultrasonography. *J Ultrasound*. 2017;20(4):267-271. doi:10.1007/s40477-017-0266-1

8) Ibitoye BO, Idowu BM, Ogunrombi AB, Afolabi BI. Ultrasonographic quantification of pleural effusion: comparison of four formulae. *Ultrasonography*. 2018;37(3):254-260. doi:10.14366/usg.17050

9) Eibenberger KL, Dock WI, Ammann ME, et al. Quantification of pleural effusions: sonography versus radiography. *Radiology*. 1994;191(3):681-684. doi:10.1148/radiology.191.3.8184046

10) Azoulay E. Pleural effusions in the intensive care unit. *Curr Opin Pulm Med*. 2003;9(4):291-297. doi:10.1097/00063198-200307000-00008

11) Colins JD, Burwell D, Furmanski S, Lorber P, Steckel RJ. Minimal detectable pleural effusions. a roentgen pathology model. *Radiology*. 1972;105(1):51-53. doi:10.1148/105.1.51

12) Goecke W, Schwerk WB. *Die Real-Time-Sonographie in Der Diagnostic von Pleuraergüssen*. Springer; 1990:89. doi:10.1007/978-3-642-93467-4_98

13) Balik M, Plasil P, Waldauf P, et al. Ultrasound estimation of volume of pleural fluid in mechanically ventilated patients. *Intensive Care Med*. 2006;32(2):318. doi:10.1007/s00134-005-0024-2

14) Cerquitella M, Saccomandi P, Schena E, et al. Ultrasound estimation of pleural effusion in geriatric patients. Paper presented at: 2016 IEEE International Symposium on Medical Measurements and Applications (MeMeA); Benevento, Italy. doi:10.1109/MeMeA.2016.7533735

15) Yetter EM, Acosta KB, Olson MC, Blundell K. Estimating splenic volume: sonographic measurements correlated with helical CT determination. *AJR Am J Roentgenol*. 2003;181(6):1615-1620. doi:10.2214/ajr.181.6.1811615

16) Canals M, Olivares R, Rosenmann M. A radiographic method to estimate lung volume and its use in small mammals. *Biol Res*. 2005;38(1). doi:10.4067/s07169760200500010006

17) Koegelenberg C, Diacon AH, Bolliger CT. Transthoracic ultrasound for chest wall, pleura, and the peripheral lung. In: Bolliger CT, Herth FJF, Mayo PH, Miyazawa T, Beamis JF, eds. *Clinical Chest Ultrasound: From the ICU to the Bronchoscopy Suite*. Karger; 2009:22-33. doi:10.1159/isbn.978-3-8055-8643-6

18) Mathis G. Pleura. In: Mathis G, ed. *Chest Sonography*. 3rd ed. Springer-Verlag; 2011:30-32. doi:10.1007/978-3-642-21247-5

Ankle Impingement Syndromes: What the Radiologist Needs to Know

Hira Qureshi, MD; Alex Sobotie, MD; Alexander Hallwachs, MD; Kacey Pagano, MD; Robert DeVita, MD; Richard Barger, MD; Vijaya Kosaraju, MD; Shana Miskovsky, MD; Navid Faraji, MD

Ankle impingement syndromes (AISs) compress the osseous and soft-tissue structures about the tibiotalar joint as a sequela of acute traumatic injury or repetitive microtrauma. They typically affect athletes who present with ankle pain and swelling that are relieved with rest. A chronic course may ensue with signs of ankle instability and/or limited range of motion (ROM), along with pain while squatting, sprinting, and climbing stairs. AISs are classified according to their location relative to the joint: anterior, anterolateral, anteromedial, posteromedial, or posterior.

While diagnosis is typically made with clinical examination, imaging plays an important role in localizing pathology and guiding treatment options, including surgery. Here, we review the anatomy, pathophysiology, physical exam, imaging characteristics, and management of AISs.

Anatomy Overview

A basic understanding of ankle anatomy is integral to understanding the structures that may be involved in the various impingement syndromes.

The tibiotalar joint comprises the articulation of the tibia, fibula, and talus (Figure 1). The tibia and fibula collectively form a mortise that houses the trochlea of the talus, while the tibia forms the medial malleolus and the fibula forms the lateral malleolus. The malleoli constrain the talus into essentially a hinge joint with inherent stability in neutral alignment. Together with the wider anterior geometry of the talar trochlea, this imparts stability to the joint such that the bony constraints resist eversion in standing alignment. However, as the joint moves through the arc of motion along its oblique axis, the soft tissues become critical in maintaining ankle stability.

The syndesmotic complex restrains motion between the distal tibia and fibula to maintain the bony mortise geometry through dynamic motion. The complex comprises the anterior tibiofibular ligament (AITFL), posterior tibiofibular ligament, and the interosseous ligament. This complex is also referred to as the "high-ankle ligaments."

Inferior to these structures are the "low-ankle ligaments," including the deltoid ligament complex and the lateral ligament complex. The medial aspect of the ankle is supported by the former, which spans the medial malleolus to the calcaneus, navicular, and talus, and consists of a superficial and a deep layer. The superficial layer consists of the tibiocalcaneal, tibionavicular, and superficial posterior tibiotalar ligaments (PTTLs). The anterior tibiotalar (ATTL) and PTTL make up the deep layer (Figure 1). The deltoid ligamentous complex has a wide range of anatomical variations.[1]

The lateral ligament complex consists of 3 ligaments: anterior talofibular ligament (ATFL), calcaneofibular ligament (CFL), and posterior talofibular ligament (PTFL). The ATFL and PTFL attach the talus to the fibula anteriorly and posteriorly, respectively, while the CFL attaches the calcaneus to the fibula (Figure 1).

Anterior Impingement

Pathophysiology

The primary mechanism of anterior impingement syndrome is direct and/or repetitive microtrauma between the anterior tibial joint line and talar neck, resulting in the formation of osseous spurs.[2,3] These spurs can entrap soft tissue, causing acute swelling

Affiliations: Department of Radiology, Henry Ford Hospital, Detroit, Michigan (Qureshi). Department of Internal Medicine, University Hospital Cleveland Medical Center, Cleveland, Ohio (Sobotie). Department of Orthopedic Surgery, University Hospital Cleveland Medical Center, Cleveland, Ohio (Hallwachs, Miskovsky). Northeast Ohio Medical University, Rootstown, Ohio (Pagano). Department of Radiology, Medical University of South Carolina, Charleston, South Carolina (DeVita). Department of Radiology, University Hospital Cleveland Medical Center, Cleveland, Ohio (Barger, Kosaraju, Faraji).
Disclosure: The authors have no conflicts of interest to disclose. None of the authors received outside funding for the production of this original manuscript and no part of this article has been previously published elsewhere.

Published: February 1, 2025. https://doi.org/10.37549/AR-D-24-0064

Figure 1. From left to right: frontal, posteromedial, and lateral depictions of relevant ankle joint anatomy created on complete anatomy.

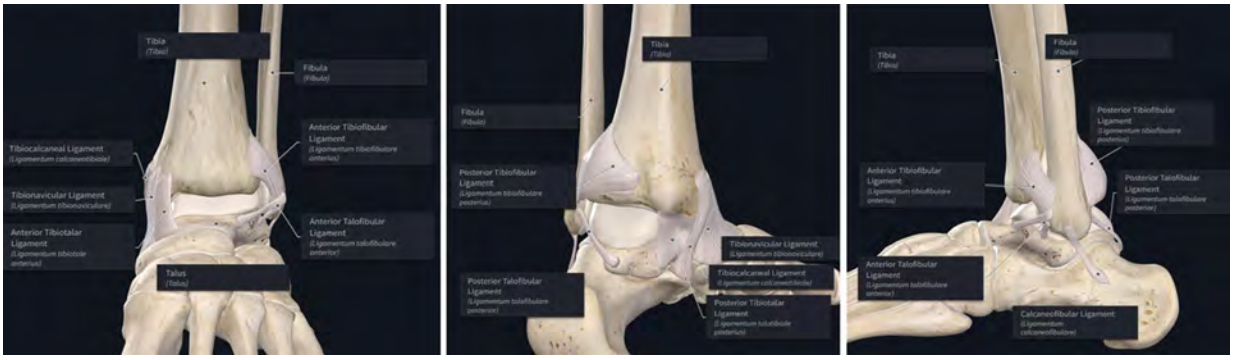

or long-term development of hypertrophic synovial plicae or adhesions and degenerative sequelae that further limit motion.[4,5]

Physical Exam

Palpating the anterior joint line in slight plantarflexion may reveal tenderness over the ankle anterior to bony osteophytes. The anterior impingement test involves hyperdorsiflexion of the joint, eliciting tenderness across the front of the ankle.[6-8] Generally, patients may sustain loss of dorsiflexion ROM compared with the contralateral side. The Silfverskiöld test is also performed to rule out isolated gastrocnemius contracture, which can also cause loss of dorsiflexion, displaying increased ankle joint dorsiflexion when the knee is flexed compared with when it is extended as a positive sign.[9-11]

Imaging Characteristics

Conventional weight-bearing radiography demonstrates characteristic spurs, which appear as beaklike osseous outgrowths from the anterior margin of the tibial plafond. These can also be accompanied by spurs at the dorsal talar neck (Figure 2). A weight-bearing lateral radiograph with the ankle in maximum dorsiflexion can demonstrate the opposing osseous spurs as seemingly overlapping at the anterior margins of the tibial plafond and talar neck.[12] Although previously described as "kissing osteophytes," morphological analyses with CT have suggested that talar and tibial spurs do not actually impinge upon each other as they are located medial and lateral to the talar dome, respectively.[13] Radiography is usually sufficient to locate and quantify the size of the relative spurs. Talar spur length as determined on plain radiographs correlates positively with talar spur width as measured by CT.[12]

Two grading systems, Anterior Impingement Classification (AIC) and Osteoarthritic Classification (OAC), have been used to assess AIS based on radiography.[14-16]

MRI may also help localize bone spurs.[17] More importantly, however, MRI helps identify intra-articular fibrous bands, which may contribute to impingement, and detect any signs of synovial reactivity such as synovitis, capsular thickening, and formation of scar and granulation tissue (Figures 3, 4).[18-20] Synovial inflammation is optimally seen on fat-suppressed T2 and contrast-enhanced fat-suppressed T1 images as an enhanced signal. MRI can also be useful in excluding other causes of pain that may clinically mimic anterior impingement such as an occult stress fracture of the anterior aspect of the distal tibia or an osteochondral lesion at the medial talar dome.[12]

Anterolateral Impingement

Pathophysiology

Anterolateral impingement (ALI) syndrome occurs when there is decreased space in the anterolateral recess—a space bounded by the ATFL and PTFL. A sprain of the ATFL is a common injury that can result in hemarthrosis and subsequent synovitis, contributing to a hyalinized fibroid mass within the recess known as a "meniscoid lesion."[21] Additionally, post-traumatic ligamentous hypertrophy and/or hyperlaxity leads to abnormal contact between the ATFL and osseous structures during movement, altering the normal biomechanics of talus extension into the recess during dorsiflexion.[22,23] Adjacent abnormalities to this recess, such as thickening of the AITFL, the presence of Basset ligament in ankle injury, or spurs at the anterolateral tibia or anterolateral talar neck, can lead to obliteration of the recess.[24-26]

Physical Exam

Patients typically demonstrate swelling and pain on palpation over the anterolateral joint line; however, most have normal ankle ROM.[27] The anterior impingement test is performed with the patient sitting and the ipsilateral knee bent to 90° while the examiner passively hyperdorsiflexes the affected ankle.

Figure 2. Conventional lateral ankle radiographs demonstrate characteristic spurs at the anterior tibial plafond and talar neck.

Figure 3. (A) T1 sagittal image demonstrates osteophytic spurring projecting from the anterior distal tibia and talar neck with surrounding region of soft-tissue fibrosis or focal synovitis. (B) T2 sagittal fat-saturated image demonstrates talar neck and anterior tibial marrow edema-like signal and intra-articular soft-tissue synovitis/fibrosis. (C) T2 coronal fat-saturated image demonstrates intra-articular soft-tissue synovitis/fibrosis.

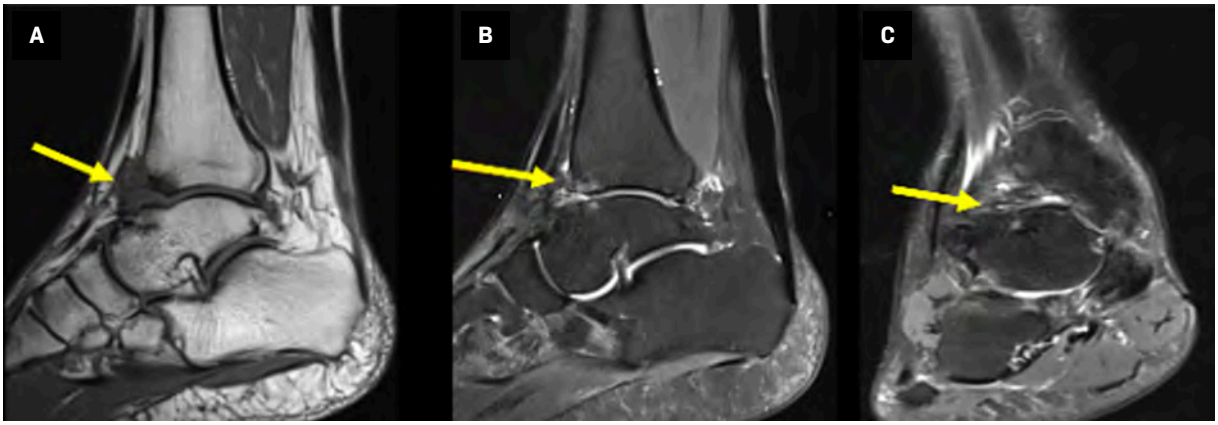

The test is considered positive if pain is elicited over the anterolateral ankle joint line (Figure 5). The anterior drawer test and talar tilt test are also performed to assess integrity of the lateral ligaments and detect possible concomitant instability.

Imaging Characteristics

Conventional radiography may help identify osteophytes contributing to anterolateral recess obstruction (Figure 6). However, given the etiology of this impingement is primarily related to soft tissue, MRI is often the modality of choice despite its variable sensitivity, which ranges from 42% to 83%.[28] Ligamentous abnormalities such as thickening of ATFL and AITFL, synovial hypertrophy, and scarring in the anterolateral recess may be seen.[28,29] In advanced cases, the fibrotic scar tissue can hyalinize into a meniscoid lesion, which has an intermediate-to-low signal intensity with peripheral rim enhancement on T1 and T2 imaging (Figure 7).[12]

MRI can be used with contrast-enhanced 3D fast spoiled gradient-echo protocols to visualize enhanced vascularized synovial and granulation tissue in the anterolateral recess with sensitivity upward of 91% and accuracy of 87%. These results are comparable to MR arthrography without being as invasive.[30,31] Bone

Figure 4. (A) Lateral radiograph of the ankle (top left) demonstrates a large intra-articular body and osteophytic spurring of the anterior talus and anterior distal tibia. (B) T2 fat-saturated sequence sagittal image (top right) demonstrates distal tibial edema-like signal and intra-articular soft-tissue synovitis/fibrosis. (C) T2 fat-saturated sequence axial image (bottom left) demonstrates anterior tibiotalar intra-articular soft-tissue synovitis/fibrosis. (D) T1 sagittal image (bottom right) demonstrates the radiographically large intra-articular body as a hypointense structure (yellow arrow).

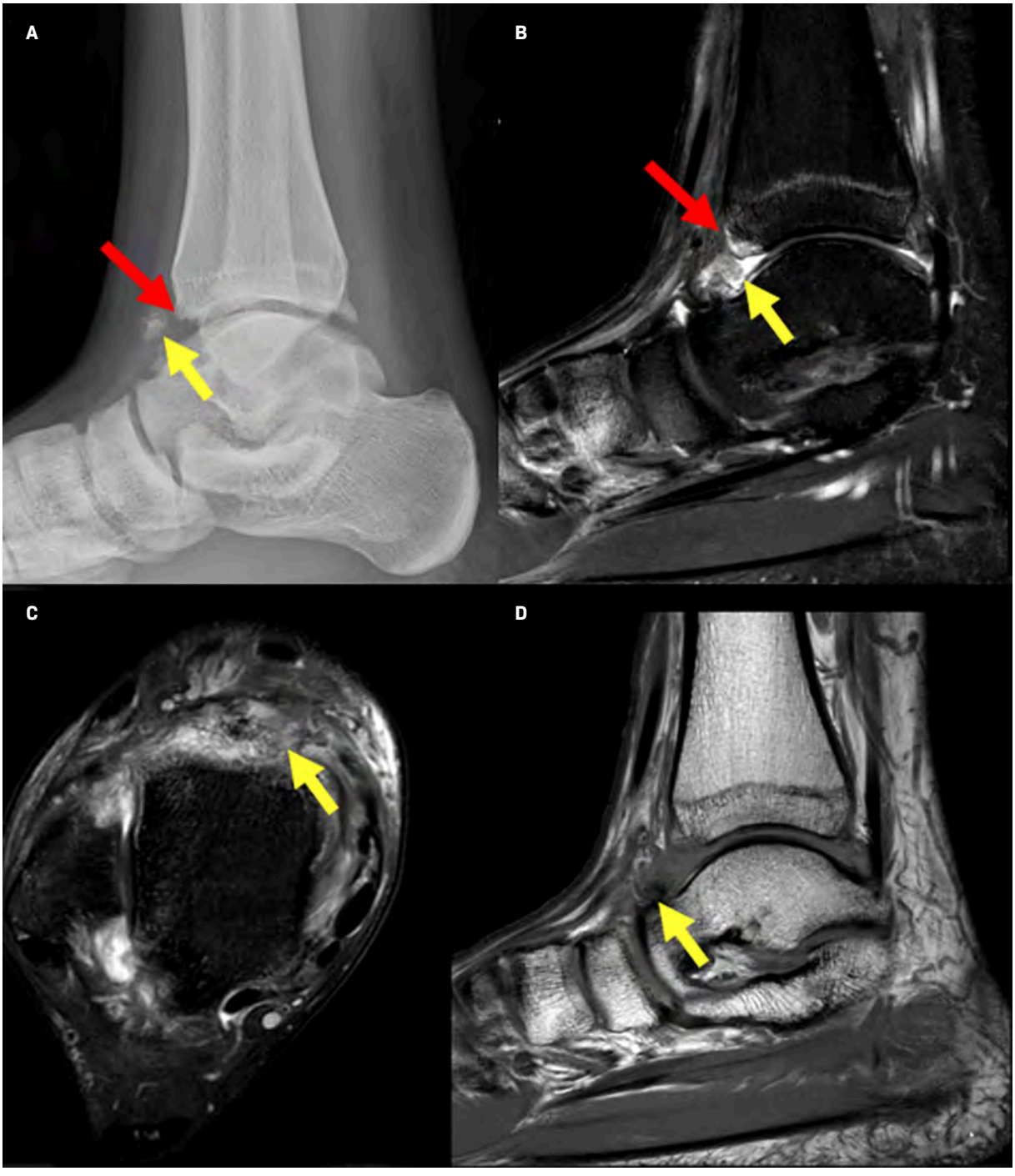

Figure 5. Anterior impingement test demonstrated with passive hyper dorsiflexion to elicit pain in the anterior ankle joint.

Figure 6. (A) Sagittal CT image demonstrates osseous spur in the anterior talar neck. (B) Sagittal CT image demonstrates osseous spur in the anterior tibial plafond.

marrow edema is rarely found.[12] It is important to remember that physical exam findings play a particularly crucial role in diagnosing anterolateral ankle impingement. Liu et al demonstrated that physical examination, with a sensitivity and specificity of 94% and 75%, respectively, was more reliable than MRI, at 39% and 50%, for the diagnosis of suspected ALI compared against intra-operative confirmation.[27]

Anteromedial Impingement

Pathophysiology

Anteromedial impingement (AMI) has been the focus of little research, owing to its rarity relative to other such syndromes, the strength of the anteromedial joint, and the destabilizing forces required to cause impingement pathologies.[32] Generally, AMI occurs with disruption of the anteromedial recess, which is bounded inferiorly by the ATTL. This can occur in the setting of ATTL thickening or hypertrophic synovial plica resulting from previous trauma or microtrauma, leading to the formation of spurs at the dorsal medial talar neck or anterior aspect of the tibia. Spurs alone are not sufficient for diagnosis.[1,33] Medial malleolar avulsion ossicles (nonunions), common in gymnasts and other athletes in high-stress sports, can also contribute to AMI.[34,35] Nonunion micromotion increases scarring and inflammation, essentially obliterating the medial ankle joint recess between the talus and medial malleolus.

Physical Exam

Palpation demonstrates pain and swelling over the medial anterior joint line. A forced anterior impingement test may also exacerbate pain, but the test has overall low sensitivity.[34] Important to assess general joint laxity or restriction, ROM testing may also reveal the presence of subtle osteophytes. Ankle valgus stress testing is used to check

Figure 7. (A) Axial T1 image and (B) coronal proton density image of the ankle demonstrate scarring in the region of the anterior talofibular ligament with a low-to-intermediate signal meniscoid-shaped mass extending into the lateral ankle gutter.

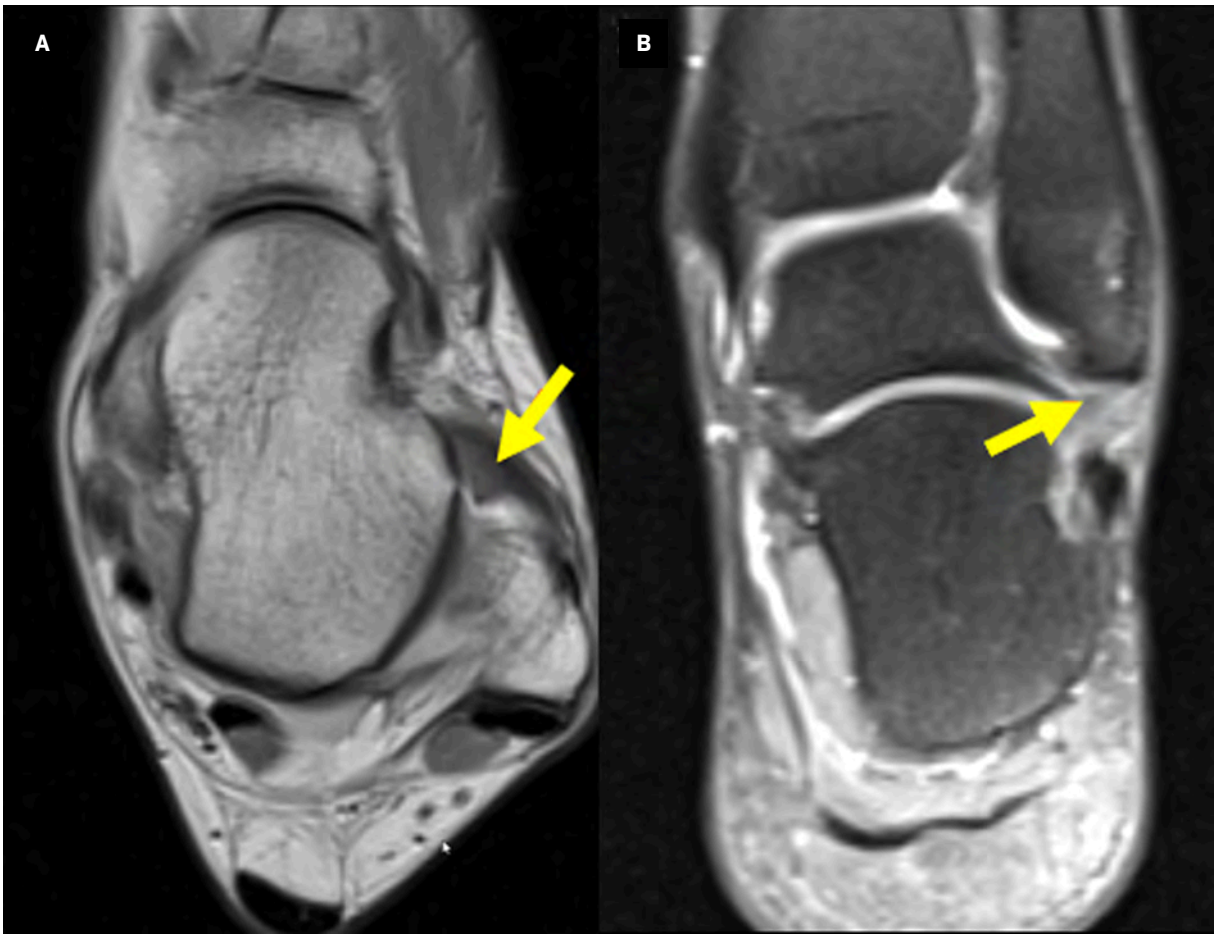

the integrity of the deltoid ligament complex compared with the contralateral ankle; increased laxity or lack of a firm endpoint may indicate more severe injury and instability.

Imaging Characteristics

Spurs often appear along the most anterior portion of the medial talar facet, along with a corresponding "kissing" osteophyte just anterior to the corner of the medial mortise and the front of the medial malleolus.[36] Anteroposterior and lateral radiographs are limited in diagnostic value because the anteromedial aspect of the tibiotalar joint is concealed by projection of the lateral aspect of the tibia. Instead, a lateral view with a craniocaudal inclination of 45°, with the foot in plantarflexion and the leg rotated 30° externally, is preferred.[14] This nearly doubles the sensitivity for tibial and talar bone spurs (Figure 8).[11]

The role of MRI in detecting AMI has not been established. Images are aimed at visualizing ancillary soft-tissue pathology such as synovitis and deltoid ligament and capsular thickening (Figures 9, 10).[37] The anteromedial recess itself may appear normal.[38] Capsular thickening may be more subtle and can be better detected with intra-articular contrast-enhanced CT or MRI.[37] MRI also plays a role in excluding other abnormalities, such as talar osteochondral injuries, in patients presenting with similar symptoms.

Posteromedial Impingement

Pathophysiology

Posteromedial impingement (PMI) is often related to damage to the PTTL, which lies anterior to the posteromedial recess. Swelling from hypertrophy caused by healing of the PTTL can lead to entrapment of the posteromedial tibiotalar joint capsule.[39] One arthroscopic study

Figure 8. Anteroposterior radiograph of the ankle demonstrates medial malleolar bone spur formation.

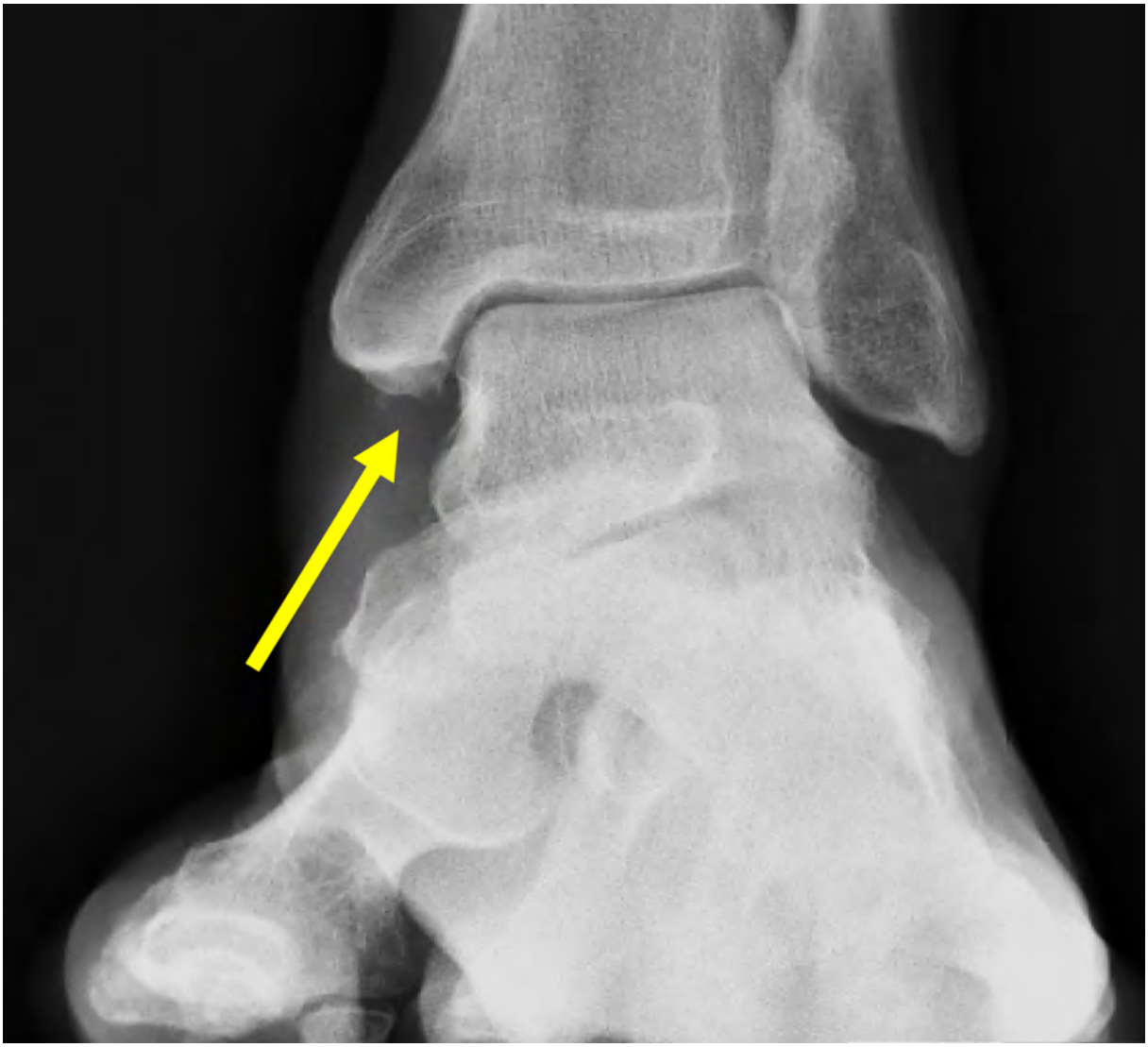

found concurrent distal medial malleolus and talar facet articular cartilage injuries in affected patients, indicating a possible association.[40]

Physical Exam

Clinical history and radiography are more useful in diagnosing PMI, owing to the challenges in examining the deeper posterior ankle tendons and ligaments.[41,42] Posteromedial pressure during ankle inversion and plantarflexion enhances identifying pain in the posteromedial corner; gait analysis is also useful as it can help differentiate true posterior tibial tendon dysfunction from PMI, which is associated with entrapment of the PTTL portion of the deltoid ligament.[43]

Imaging Characteristics

As pathophysiology is largely related to soft-tissue pathology, radiography plays a little role in imaging for PMI syndromes. Radiographs may show periosteal new bone formation along the posteromedial wall of the talus and along the medial malleolus.[43] On MRI, signs can vary based on chronicity; in the subacute stage (within 4 weeks post-injury), the primary finding can be increased signal in the posteromedial capsule and the PTFL, whereas chronic stages (greater than 14 weeks post-injury) demonstrate a higher incidence of PTTL disruption with thickening and loss of normal fibrillar pattern, resulting in an amorphous appearance (Figure 11).[42] Fluid-sensitive sequences increase the conspicuity of synovitis, which may be seen as a focal increased signal relative to adjacent tissue.[44] Marrow

Figure 9. (A, B) Axial proton density and proton density fat-saturated images demonstrate thickening and increased signal intensity of anteromedial ankle soft tissues, including the tibial spring ligament and the superficial portion of the deltoid ligament. Note that the tibialis posterior tendon (green arrow) demonstrates a normal appearance, arguing against a sequela of posterior tibial tendon dysfunction. (C) Coronal proton density fat-saturated image demonstrates thickening and edema of the anteromedial ankle soft tissues.

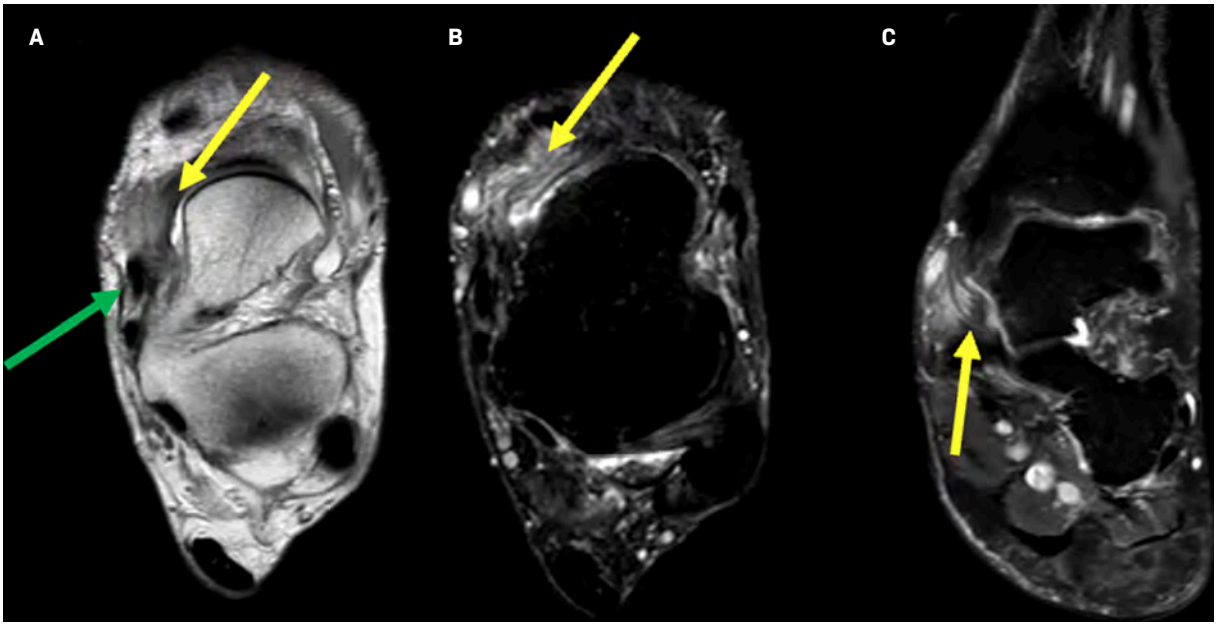

Figure 10. (A) Anteroposterior radiograph of the foot shows osteophytic spurring of the medial talar neck and the distal tip of the medial malleolus. (B) Axial T2 fat-saturated image of the ankle demonstrates a reactive marrow edema-like signal of the medial talus and focal synovitis in the anteromedial gutter. (C) Coronal proton density fat-saturated image of the ankle demonstrates thickening of the deltoid ligament, focal synovitis in the anteromedial gutter, and reactive marrow edema-like signal of the talus.

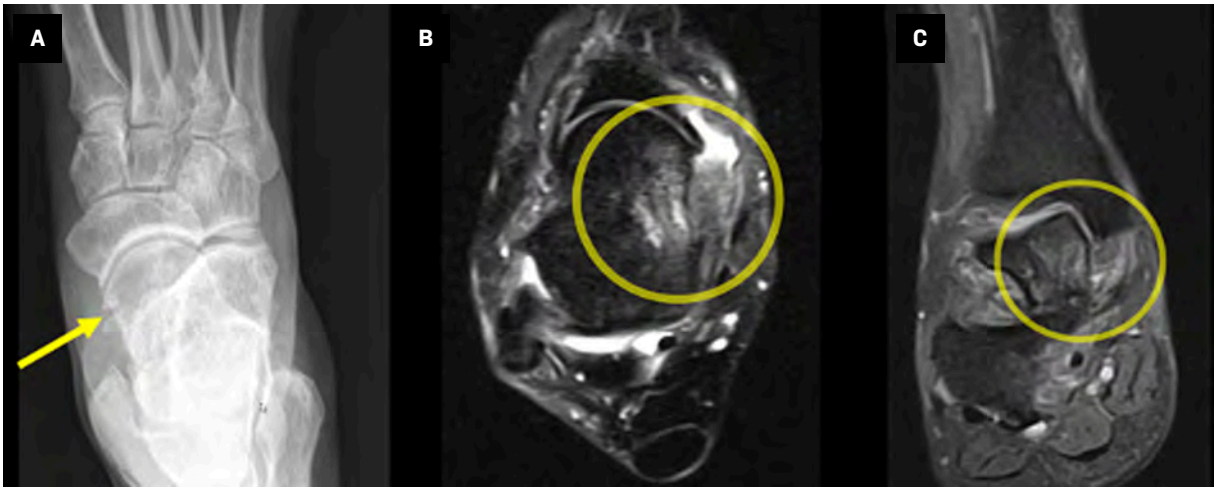

edema can be seen infrequently and has no specific distribution.[45] In general, bone changes are less common in PMI; however, small cortical avulsion fractures may be present in the PTTL and are best demonstrated on CT.[44]

Posterior Impingement

Pathophysiology

The posterior ankle is bordered by the posterior tibia and calcaneus and extends to the Kager fat pad. Compression within this region during plantar flexion is characteristic of posterior impingement (PI) syndrome.

In particular, os trigonum is a common finding, seen in up to 63% of patients with PI.[46] Normally, the

Figure 11. (A) Coronal T2 fat-saturated image of the ankle demonstrates reactive edema-like signal and fluid within the posteriomedial ankle, likely owing to impingement by prominent talocalcaneal osteophytes. (B) Axial T2 fat-saturated image of the ankle demonstrates thickening and loss of the normal deltoid ligament striations and marked posteromedial soft-tissue swelling.

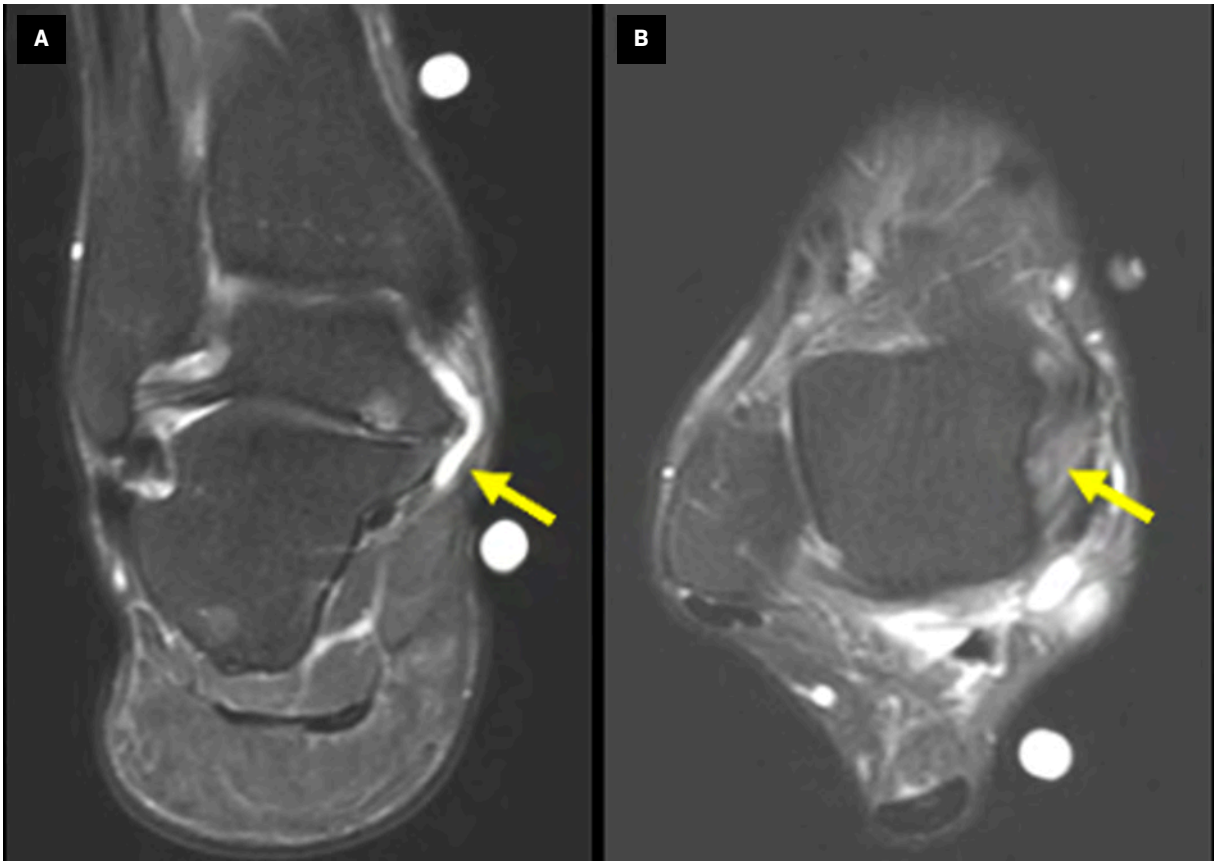

Weight-bearing radiography in the anteroposterior, latera.

secondary ossification center of the posterolateral talus forms between the ages of 8 and 13 years and fuses within 1 year; however, 7 % of the time a lack of fusion can result in an os trigonum.[47] Other osseous pathologies, such as chronic fracture nonunion of the medial tubercle of the posterior talus, can present with a similar clinical picture or a congenital Stieda process, which is a fusion of a secondary ossification center, resulting in posterolateral elongation of the talus.[46]

Physical Exam

Examination involves passive hyperplantarflexion of the ankle while using 2 fingers to palpate just lateral to the Achilles tendon at the level of the distal fibula; PI is suspected if the patient's pain is reproduced. Contributing pathology can be delineated with maneuvers such as the Tomassen test, in which a positive result reveals decreased ROM of the great toe metatarsophalangeal joint with the ankle dorsiflexed. This can suggest FHL pathology (Figure 12). Additional maneuvers, such as a calcaneal squeeze test, which involves squeezing both sides of the posterior tuberosity, can raise concern for differential diagnoses such as a calcaneal stress fracture involving the posterior tuberosity.

Imaging Characteristics

Weight-bearing radiography in the anteroposterior, lateral, and mortise views, along with an oblique view of the foot, is important for treatment planning. The oblique view, with the foot in 25° of external rotation, can help differentiate hypertrophy of the posterior talar process from os trigonum in cases of bony impingement.[48] Advanced imaging may also be necessary in equivocal cases.

Os trigonum in the lateral view is the most pertinent radiographic finding when assessing for PI; however, its presence

Figure 12. Normal examination of great toe metatarsophalangeal joint pathology range of motion, which is greater in ankle plantarflexion than ankle dorsiflexion. Alternative findings can be suggestive of flexor hallucis longus pathology.

Figure 13. (A) Axial T2 fat-saturated image demonstrates thickening of the posterior talofibular ligament. (B) Axial T2 fat-saturated image demonstrates thickening of the posterior intermalleolar ligament. (C) Sagittal T2 fat-saturated image demonstrates abnormal edema adjacent to the posterior talus suggestive of posterior ankle impingement. (D) Sagittal T1 image demonstrates a prominent os trigonum.

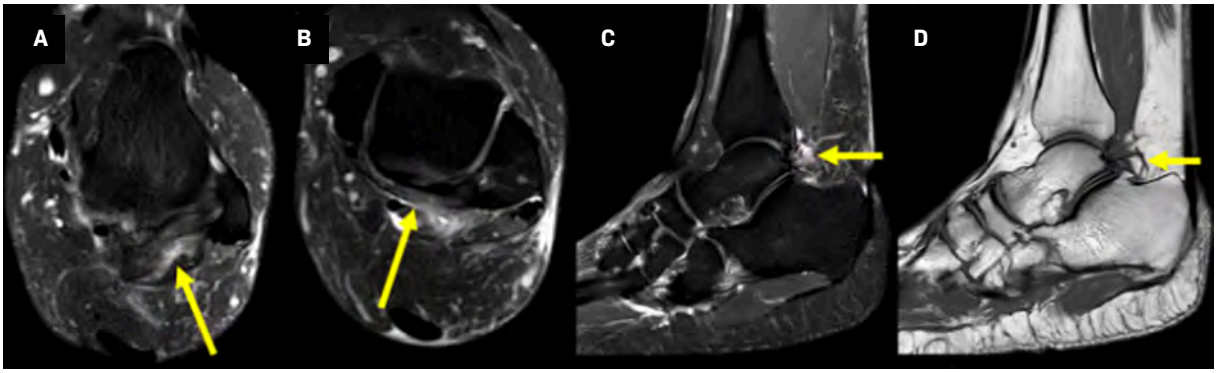

alone is not sufficient to cause impingement, but it can contribute to symptomatology.[18] Up to 14% of the asymptomatic population may have an os trigonum.[49]

CT facilitates the assessment of osseous changes between the os trigonum and talus, such as fragmentation of the os and pressure-related erosions along the talus.[49] On MRI, PI can present with bone marrow edema within the talus, os trigonum, increased signal at synchondrosis, fluid accumulation around the posterior talus and tibia, and synovitis with thickening of posterior ligaments (Figures 13, 14).[50] In certain populations such as ballet dancers, who frequently practice maximal plantar flexion, hyaline-like cartilage can form on the posterior talus, appearing as low-signal intensity on T2 images.[51]

Treatment

Despite mixed study findings in the literature, standard initial therapy of AISs consists of nonsteroidal anti-inflammatory drugs, physical therapy, and intra-articular steroid injections for 3-6 months to reduce stress on the joint and promote healing.[8,9,11,52]

Surgical intervention may be warranted if pain or restriction persists beyond 6 months. Surgery aims to remove osteophytes, debride inflamed soft tissue and loose fragments in the joint space, and correct coexisting contributing conditions.[6-811,15,22,,34] While open arthrotomy was once considered the standard procedure, complications such as cutaneous nerve entrapment, long extensor tendon damage, wound dehiscence, and hypertrophic scar tissue formation led to a shift toward arthroscopy, reducing recovery times and complication rates (Figures 15–19).[6,11,16,53-55]

Conclusion

Imaging plays an important role in localizing pathology and guiding treatment of AISs. Choice of modality is based largely on the pathophysiology of the impingement.

Radiography is particularly useful in cases caused by ossesous abnormalities such as AI. As mentioned earlier, 2 commonly

Figure 14. (A) Lateral radiograph of the ankle demonstrates an os trigonum. (B) Axial T2 fat-saturated image shows reactive marrow edema-like signal of the os trigonum, fluid across the synchondrosis, and marked posterior synovitis. (C) Sagittal T2 image shows reactive marrow edema-like signal of the talus and os trigonum with reactive posterior tibiotalar and subtalar joint effusions.

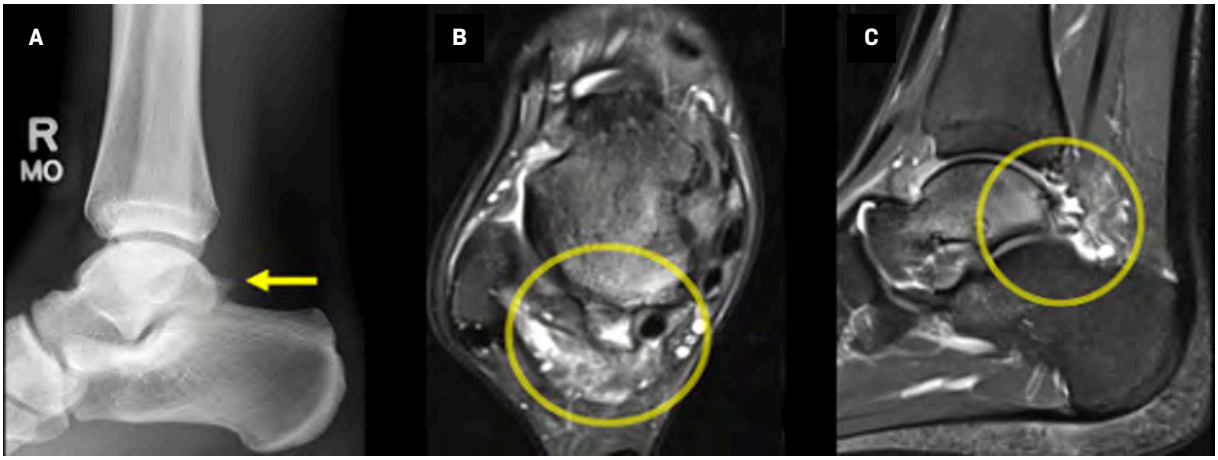

Figure 15. Surgical management of anterior impingement. (A) Anterolateral arthroscopic view shows talar spur, with arrows pointing at approximate demarcation from the talus neck and shaver burr holding up the joint capsule. (B) Medial arthroscopic view after debridement with arrows demonstrates a restoration of the concavity of the talar neck with restoration of normal anatomic profile.

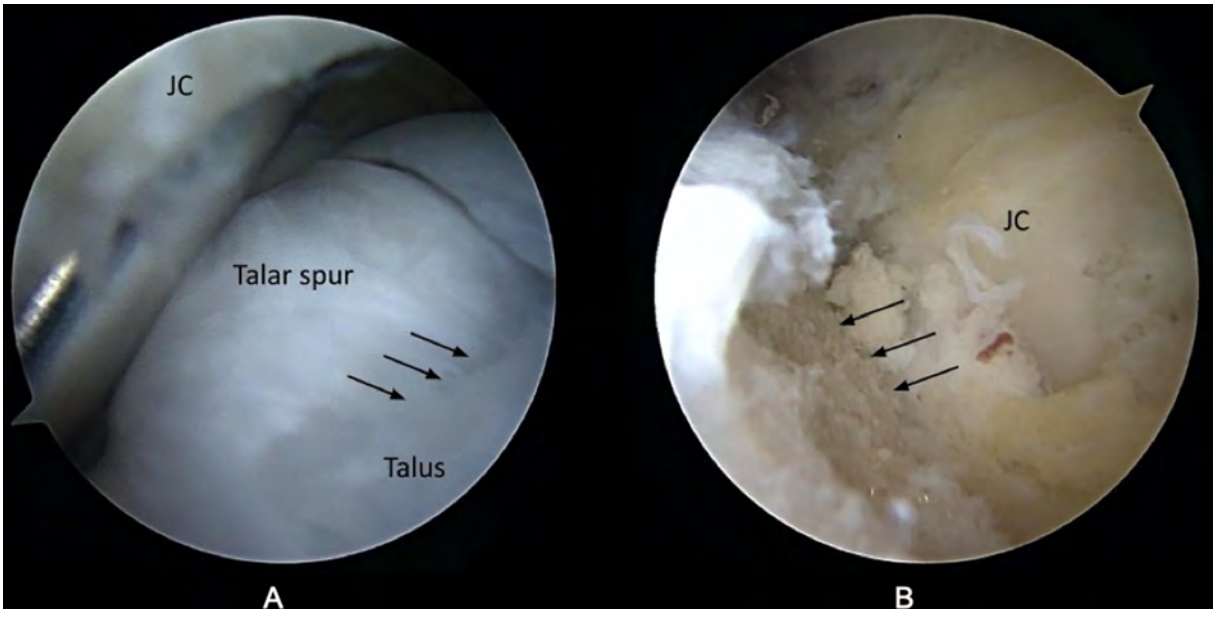

used classification systems for AI are the AIC and OAC. Preoperative staging, especially regarding the extent of degenerative changes, is a significant factor in predicting treatment outcomes in anterior impingement types. When using AIC, arthroscopic surgical interventions have demonstrated good outcomes in type I and II AI, with less successful outcomes in type III and IV cases.[19,20] The OAC can also be predictive of outcomes; arthroscopic surgical interventions have been reported to deliver good outcomes in patients with grade O/I impingements, while not faring as well in patients with grade II/III impingments.[19,53] Van Dijk et al found that the OAC classification was a better predictor of surgical outcomesl[19]; however, Coull et al concluded that the OAC system did not provide enough detail and that patients were too broadly grouped.[14] Further studies comparing the 2 classification systems as well as developing additional systems for other impingement syndromes would be useful in quantifying image findings for surgical planning.

In some cases, CT can permit a more detailed assessment of the

Figure 16. Surgical management of anterior impingement. (A) Anterolateral arthroscopic view of relative anatomy shows a loose body encased in arthrofibrotic bands with the tibia seen behind. (B) Central arthroscopic view of deformation after the loose body and arthrofibrotic band were debrided showing chondromalacia on the tibia.

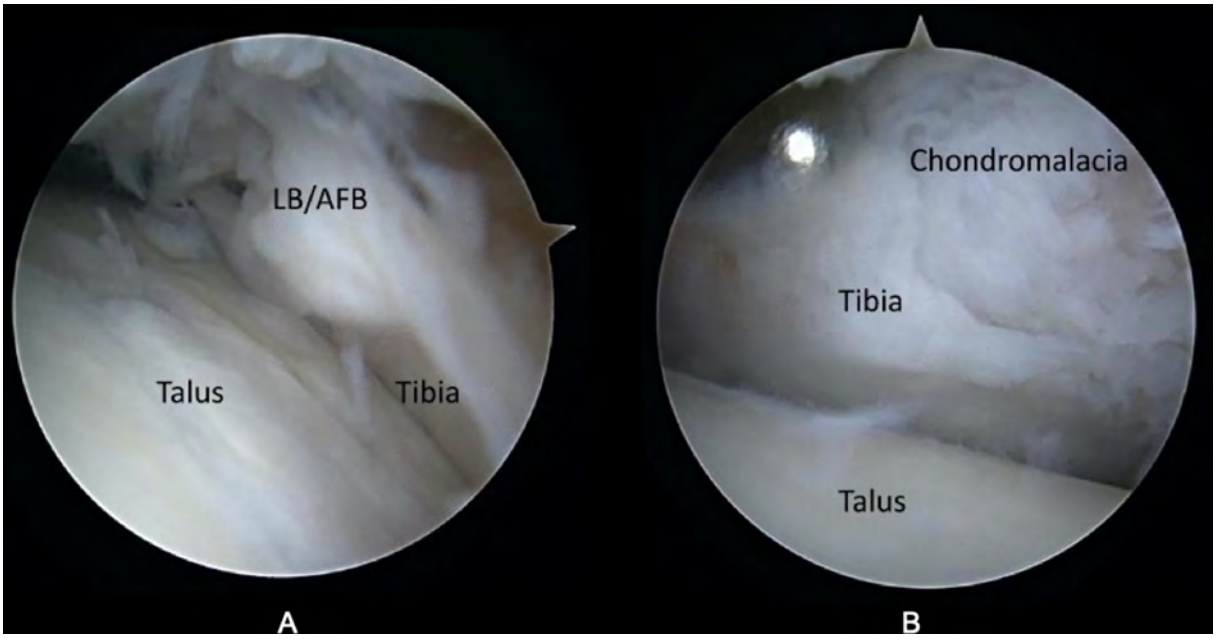

Figure 17. : Surgical management of anterolateral impingement. (A) Anterolateral arthroscopic view with meniscoid lesion in syndesmosis. (B) Arthroscopic view of anatomy after debridement of syndesmotic meniscoid lesion.

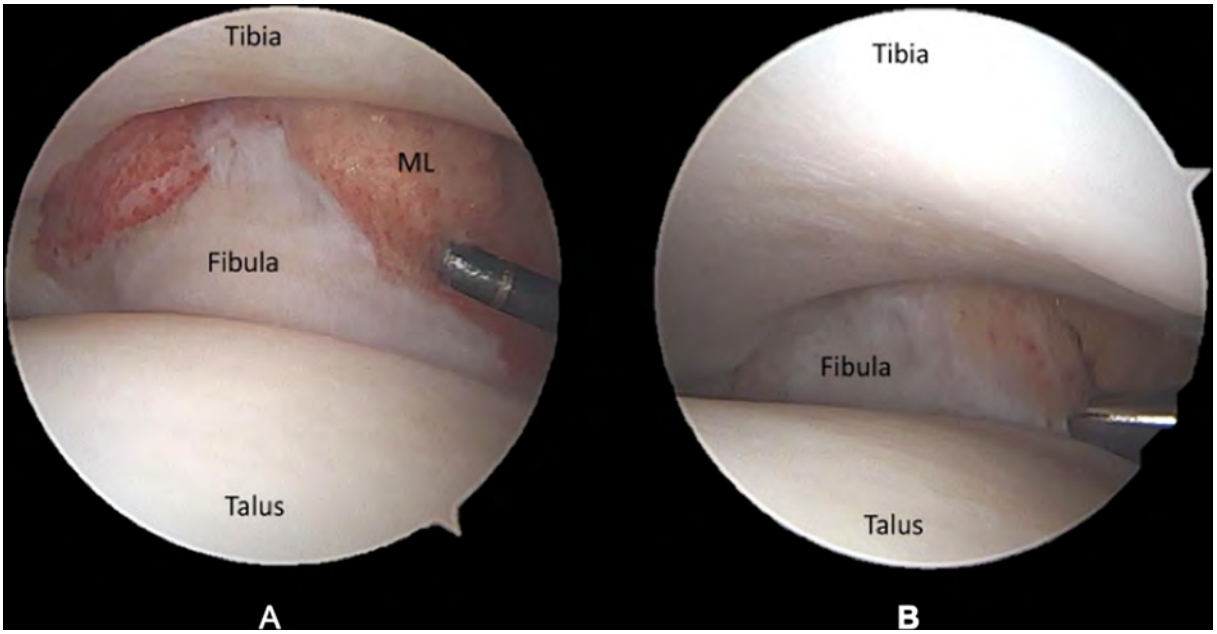

Figure 18. Surgical management of anteromedial impingement. (A) Arthroscopic view of hypertrophied anteromedial plica band. (B) Arthroscopic view after the removal of plica band and debridement shows medial malleolus and restoration of relative anatomy.

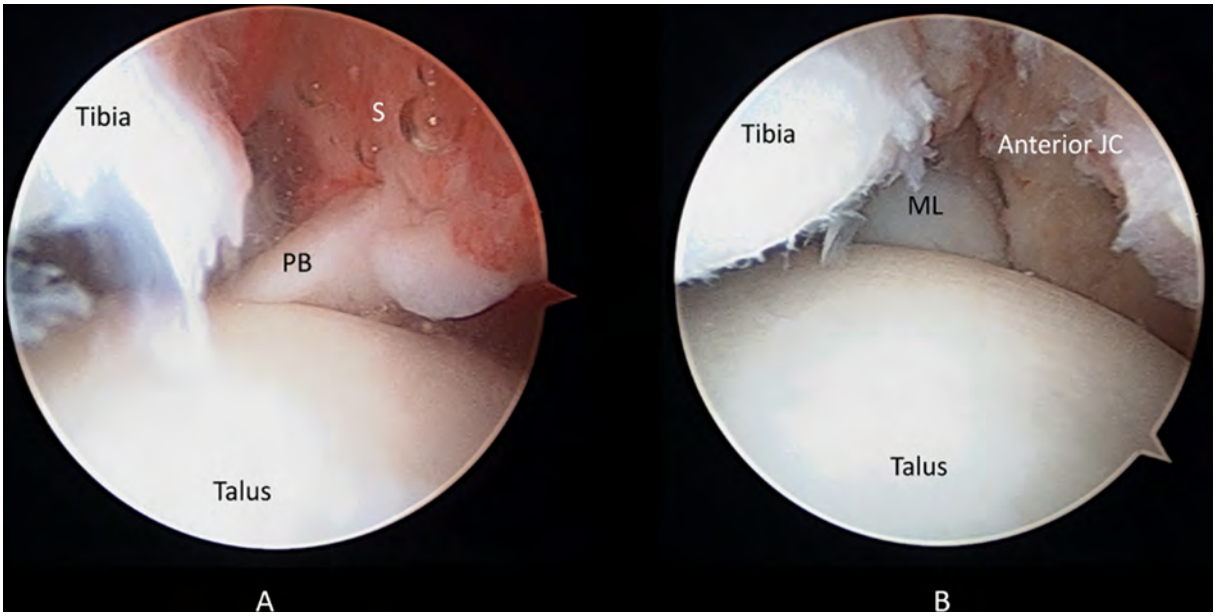

Figure 19. Surgical management of posterior impingement. (A) Relative osseus anatomy demonstrates os trigonum, calcaneus, and talus. (B) Hindfoot endoscopy view shows complete os trigonum removal after resection of medial and lateral attachments.

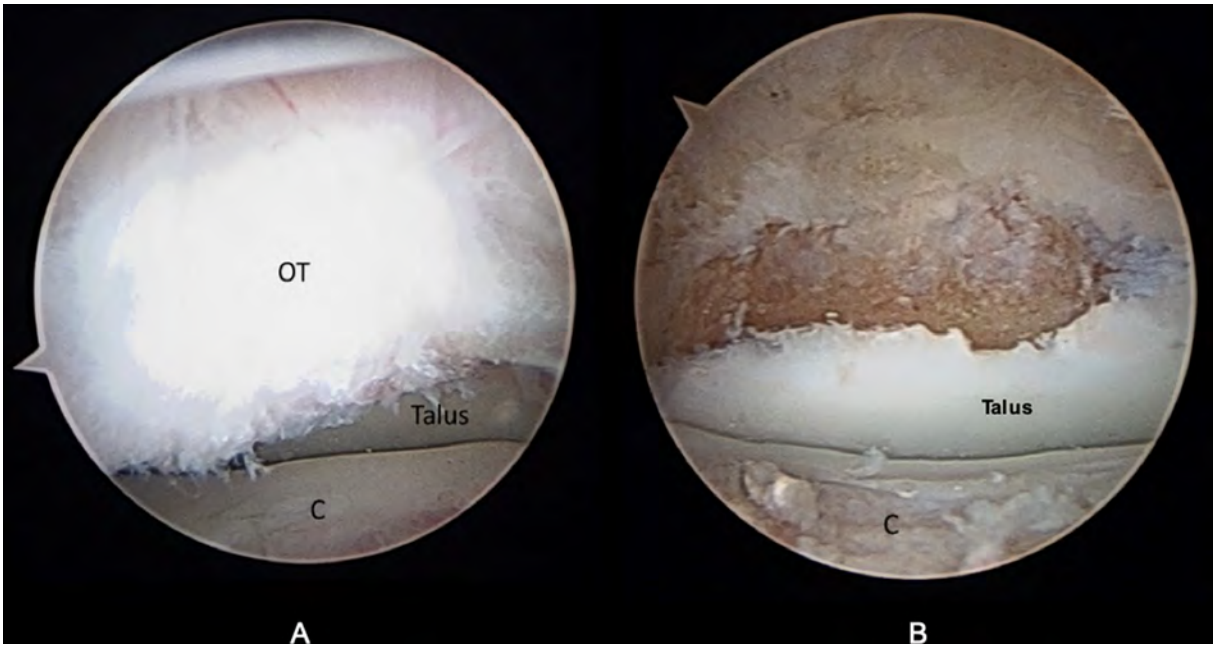

location and burden of osteophytes and other osseous abnormalities, particularly in cases where the physical exam and history are not consistent with initial imaging findings. Indeed, more detailed imaging can sometimes change the diagnosis from a single form of impingement to a combined type, potentially redirecting the approach to treatment.[56]

As CT provides limited information on bone marrow and soft-tissue abnormalities, MRI can be useful in syndromes caused predominantly by soft-tissue pathology. Alternatively, patients without clinical symptoms or signs of AIS have been found to have incidental abnormalities on MR arthrography that are then confirmed at surgery.[57] Thus, a thorough history and physical examination are important to accurately correlate imaging features and treat only symptomatic cases of AISs.

References

1) Glenzer SR, Domingue GA, Perry MD. Anteromedial ankle impingement due to a talar cam lesion and anterior deep deltoid ligament with variant anatomy: a case report. *Foot Ankle Orthop*. 2020;5(4). doi:10.1177/2473011420977427

2) Yang Q, Zhou Y, Xu Y. Arthroscopic debridement of anterior ankle impingement in patients with chronic lateral ankle instability. *BMC Musculoskelet Disord*. 2018;19(1):239. doi:10.1186/s12891-018-2168-6

3) Mosca M, Caravelli S, Fuiano M, et al. Management of early ankle osteoarthritis through anterior joint-preserving surgery: a retrospective evaluation at mid- to long-term follow-up. *Eur J Orthop Surg Traumatol*. 2020;30(7):1171-1178. doi:10.1007/s00590-020-02691-6

4) Viehöfer AF, Casari F, Waibel FWA, et al. Smoking is associated with anterior ankle impingement after isolated autologous matrix-induced chondrogenesis for osteochondral lesions of the talus. *Cartilage*. 2021;13(1_suppl):1366S-1372S. doi:10.1177/1947603520959405

5) Morelli F, Princi G, Rossato A, Iorio R, Ferretti A. Pigmented villonodular synovitis: a rare case of anterior ankle impingement. *J Orthop Case Rep*. 2019;10(1):16-18. doi:10.13107/jocr.2019.v10.i01.1618

6) Hawkins RB. Arthroscopic treatment of sports-related anterior osteophytes in the ankle. *Foot Ankle*. 1988;9(2):87-90. doi:10.1177/107110078800900205

7) McMurray TP. Footballer's ankle. *J Bone Joint Surg Br*. 1950;32-B(1):68-69. doi:10.1302/0301-620X.32B1.68

8) Talusan PG, Toy J, Perez JL, Milewski MD, Reach JS Jr. Anterior ankle impingement: diagnosis and treatment. *J Am Acad Orthop Surg*. 2014;22(5):333-339. doi:10.5435/JAAOS-22-05-333

9) Branca A, Di Palma L, Bucca C, Visconti CS, Di Mille M. Arthroscopic treatment of anterior ankle impingement. *Foot Ankle Int*. 1997;18(7):418-423. doi:10.1177/107110079701800708

10) Sanders TG, Rathur SK. Impingement syndromes of the ankle. *Magn Reson Imaging Clin N Am*. 2008;16(1):29-38. doi:10.1016/j.mric.2008.02.005

11) Tol JL, van Dijk CN. Anterior ankle impingement. *Foot Ankle Clin*. 2006;11(2):297-310. doi:10.1016/j.fcl.2006.02.002

12) Al-Riyami AM, Tan HK, Peh WCG. Imaging of ankle impingement syndromes. *Can Assoc Radiol J*. 2017;68(4):431-437. doi:10.1016/j.carj.2017.04.001

13) Berberian WS, Hecht PJ, Wapner KL, DiVerniero R. Morphology of tibiotalar osteophytes in anterior ankle impingement. *Foot Ankle Int*. 2001;22(4):313-317. doi:10.1177/107110070102200407

14) van Dijk CN, Tol JL, Verheyen CC. A prospective study of prognostic factors concerning the outcome of arthroscopic surgery for anterior ankle impingement. *Am J Sports Med*. 1997;25(6):737-745. doi:10.1177/036354659702500603

15) Scranton PE Jr, McDermott JE. Anterior tibiotalar spurs: a comparison of open versus arthroscopic debridement. *Foot Ankle*. 1992;13(3):125-129. doi:10.1177/107110079201300303

16) Coull R, Raffiq T, James LE, Stephens MM. Open treatment of anterior impingement of the ankle. *J Bone Joint Surg Br*. 2003;85(4):550-553. doi:10.1302/0301-620x.85b4.13871

17) Shim DW, Kim S, Hwang Y, et al. Detection of the tram track lesion in the ankle joint: comparing 3.0-tesla magnetic resonance imaging and arthroscopy. *Arthroscopy*. 2018;34(3):866-871. doi:10.1016/j.arthro.2017.09.014

18) Berman Z, Tafur M, Ahmed SS, Huang BK, Chang EY. Ankle impingement syndromes: an imaging review. *Br J Radiol*. 2017;90(1070):20160735. doi:10.1259/bjr.20160735

19) Haller J, Bernt R, Seeger T, et al. MR-imaging of anterior tibiotalar impingement syndrome: agreement, sensitivity and specificity of MR-imaging and indirect MR-arthrography. *Eur J Radiol*. 2006;58(3):450-460. doi:10.1016/j.ejrad.2006.03.008

20) Zbojniewicz AM. Impingement syndromes of the ankle and hindfoot. *Pediatr Radiol*. 2019;49(12):1691-1701. doi:10.1007/s00247-019-04459-5

21) Wolin I, Gassmani F, Sheinman S, Levinthal DH. Internal derangement of the talofibular component of the ankle. *Surg Gynecol Obstet*. 1950;91(2):193-200.

22) Bassett FH 3rd, Gates HS 3rd, Billys JB, Morris HB, Nikolaou PK. Talar impingement by the anteroinferior tibiofibular ligament. A cause of chronic pain in the ankle after inversion sprain. *J Bone Joint Surg*. 1990;72(1):55-59. doi:10.2106/00004623-199072010-00009

23) van den Bekerom MPJ, Raven EEJ. The distal fascicle of the anterior inferior tibiofibular ligament as a cause of tibiotalar impingement syndrome: a current concepts review. *Knee Surg Sports Traumatol Arthrosc*. 2007;15(4):465-471. doi:10.1007/s00167-006-0275-7

24) Odak S, Ahluwalia R, Shivarathre DG, et al. Arthroscopic evaluation of impingement and osteochondral lesions in chronic lateral ankle instability. *Foot Ankle Int*. 2015;36(9):1045-1049. doi:10.1177/1071100715585525

25) Talbot CE, Knapik DM, Miskovsky SN. Prevalence and location of bone spurs in anterior ankle impingement: a cadaveric investigation. *Clin Anat*. 2018;31(8):1144-1150. doi:10.1002/ca.23216

26) Edama M, Kageyama I, Kikumoto T, et al. Morphological features of the anterior talofibular ligament by the number of fiber bundles. *Ann Anat*. 2018;216:69-74. doi:10.1016/j.aanat.2017.11.001

27) Liu SH, Raskin A, Osti L, et al. Arthroscopic treatment of anterolateral ankle impingement. *Arthroscopy*. 1994;10(2):215-218. doi:10.1016/S0749-8063(05)80097-0

28) Duncan D, Mologne T, Hildebrand H, et al. The usefulness of magnetic resonance imaging in the diagnosis of anterolateral impingement of the ankle. *J Foot Ankle Surg*. 2006;45(5):304-307. doi:10.1053/j.jfas.2006.06.003

29) De Maeseneer M, Wuertzer S, de Mey J, Shahabpour M. The imaging findings of impingement syndromes of the lower limb. *Clin Radiol*. 2017;72(12):1014-1024. doi:10.1016/j.crad.2017.07.018

30) Choo HJ, Suh J-S, Kim S-J, et al. Ankle MRI for anterolateral soft tissue impingement: increased accuracy with the use of contrast-enhanced fat-suppressed 3D-FSPGR MRI. *Korean J Radiol*. 2008;9(5):409-415. doi:10.3348/kjr.2008.9.5.409

31) Lee JW, Suh JS, Huh YM, Moon ES, Kim SJ. Soft tissue impingement syndrome of the ankle: diagnostic efficacy of MRI and clinical results after arthroscopic treatment. *Foot Ankle Int*. 2004;25(12):896-902. doi:10.1177/107110070402501209

32) Shane AM, Reeves CL, Vazales R, Farley Z. Soft tissue impingement of the ankle: pathophysiology, evaluation, and arthroscopic treatment. *Clin Podiatr Med Surg*. 2016;33(4):503-520. doi:10.1016/j.cpm.2016.06.003

33) Massada JL. Ankle overuse injuries in soccer players. morphological adaptation of the talus in the anterior impingement. *J Sports Med Phys Fitness*. 1991;31(3):447-451.

34) Ross KA, Murawski CD, Smyth NA, et al. Current concepts review: arthroscopic treatment of anterior ankle impingement. *Foot Ankle Surg*. 2017;23(1):1-8. doi:10.1016/j.fas.2016.01.005

35) Vann MA II, Manoli A II. Medial ankle impingement syndrome in female gymnasts. *Oper Tech Sports Med*. 2010;18(1):50-52. doi:10.1053/j.otsm.2009.11.003

36) Russo A, Zappia M, Reginelli A, et al. Ankle impingement: a review of multimodality imaging approach. *Musculoskelet Surg*. 2013;97 Suppl 2:S161-8. doi:10.1007/s12306-013-0286-8

37) Donovan A, Rosenberg ZS. MRI of ankle and lateral hindfoot impingement syndromes. *AJR Am J Roentgenol*. 2010;195(3):595-604. doi:10.2214/AJR.09.4199

38) Robinson P, White LM, Salonen D, Ogilvie-Harris D. Anteromedial impingement of the ankle: using MR arthrography to assess the anteromedial recess. *Am J Roentgenol*. 2002;178(3):601-604. doi:10.2214/ajr.178.3.1780601

39) Song W, Liu W, Chen B, et al. Posteromedial ankle impingement caused by hypertrophy of talocalcaneal coalition: a report of five cases and introduction of a novel index system. *J Foot Ankle Surg*. 2016;55(6):1312-1317. doi:10.1053/j.jfas.2016.01.005

40) van Dijk CN, Wessel RN, Tol JL, Maas M. Oblique radiograph for the detection of bone spurs in anterior ankle impingement. *Skeletal Radiol*. 2002;31(4):214-221. doi:10.1007/s00256-002-0477-0

41) Giannini S, Buda R, Mosca M, Parma A, Di Caprio F. Posterior ankle impingement. *Foot Ankle Int*. 2013;34(3):459-465. doi:10.1177/1071100713477609

42) Koulouris G, Connell D, Schneider T, Edwards W. Posterior tibiotalar ligament injury resulting in posteromedial impingement. *Foot Ankle Int*. 2003;24(8):575-583. doi:10.1177/107110070302400802

43) Paterson RS, Brown JN. The posteromedial impingement lesion of the ankle. A series of six cases. *Am J Sports Med*. 2001;29(5):550-557. doi:10.1177/03635465010290050501

44) LiMarzi GM, Scherer KF, Richardson ML, et al. CT and mr imaging of the postoperative ankle and foot. *Radiographics*. 2016;36(6):1828-1848. doi:10.1148/rg.2016160016

45) Messiou C, Robinson P, O'Connor PJ, Grainger A. Subacute posteromedial impingement of the ankle in athletes: MR imaging evaluation and ultrasound guided therapy. *Skeletal Radiol*. 2006;35(2):88-94. doi:10.1007/s00256-005-0049-1

46) Srirangarajan T, Abbasian A. Chronic fracture of the posteromedial tubercle of the talus masquerading as os trigonum syndrome. *Case Rep Orthop*. 2021;2021:6637081. doi:10.1155/2021/6637081

47) Özer M, Yıldırım A. Evaluation of the prevalence of os trigonum and talus osteochondral lesions in ankle magnetic resonance imaging of patients with ankle impingement syndrome. *J Foot Ankle Surg*. 2019;58(2):273-277. doi:10.1053/j.jfas.2018.08.043

48) Gasparetto F, Collo G, Pisanu G, et al. Posterior ankle and subtalar arthroscopy: indications, technique, and results. *Curr Rev Musculoskelet Med*. 2012;5(2):164-170. doi:10.1007/s12178-012-9118-y

49) Karasick D, Schweitzer ME. The os trigonum syndrome: imaging features. *AJR Am J Roentgenol*. 1996;166(1):125-129. doi:10.2214/ajr.166.1.8571860

50) Bureau NJ, Cardinal E, Hobden R, Aubin B. Posterior ankle impingement syndrome: MR imaging findings in seven patients. *Radiology*. 2000;215(2):497-503. doi:10.1148/radiology.215.2.r00ma01497

51) Kinugasa K, Shimomura K, Tachibana Y, et al. Posterior ankle impingement caused by hyaline-like cartilage generation in ballet dancers-a report of 2 cases. *J Foot Ankle Surg*. 2022;61(4):e9-e14. doi:10.1053/j.jfas.2021.10.015

52) Ogilvie-Harris DJ, Mahomed N, Demazière A. Anterior impingement of the ankle treated by arthroscopic removal of bony spurs. *J Bone Joint Surg Br*. 1993;75(3):437-440. doi:10.1302/0301-620X.75B3.8496216

53) Martin DF, Baker CL, Curl WW, et al. Operative ankle arthroscopy. *Am J Sports Med*. 1989;17(1):16-23. doi:10.1177/036354658901700103

54) O'Donoghue DH. Impingement exostoses of the talus and tibia. *J Bone Joint Surg Am*. 1957;39-A(4):835-852.

55) Parkes JC II, Hamilton WG, Patterson AH, Rawles JG. The anterior impingement syndrome of the ankle. *J Trauma*. 1980;20(10):895-898. doi:10.1097/00005373-198010000-00015

56) Cosma DI, Vasilescu DE, Corbu A, et al. Combined anterolateral, anterior, and anteromedial ankle impingement in an adolescent soccer player: a case report and review of the literature. *Clin J Sport Med*. 2019;29(6):e80-e82. doi:10.1097/JSM.0000000000000576

57) Robinson P, White LM, Salonen DC, Daniels TR, Ogilvie-Harris D. Anterolateral ankle impingement: MR arthrographic assessment of the anterolateral recess. *Radiology*. 2001;221(1):186-190. doi:10.1148/radiol.2211001666

CT-Like Images from MRI: A Comprehensive Review of the Zero-Echo-Time Sequence

Yesim Yekta Yuruk, MD; Mehmet Simsar, MD; Yeliz Pekcevik, MD

MRI is a noninvasive imaging modality that provides excellent soft-tissue contrast and high resolution of anatomic detail in the body structures without ionizing radiation.[1,2] Despite these advantages, conventional MRI sequences are not as successful as CT in depicting the bone cortex and calcified structures owing to these structures' low proton density (approximately 20% water) and short T2 relaxation times (approximately 390milliseconds at 3 T MRI).[3]

CT is more successful in imaging bone structures and calcifications, owing to the modality's high spatial resolution, fast acquisition, and high availability. However, poor soft-tissue resolution and radiation exposure are the major disadvantages of CT.[4,5]

Therefore, MRI may be a more ideal modality if better cortical bone and calcific structure image quality are provided. This is possible with the zero-echo-time (ZTE) MRI sequence, a new technique that uses ultra-fast readouts to capture signals from short-T2 tissues and aims to capture cortical bone and calcific structure images without ionizing radiation. This sequence provides "CT-like" images with the additional benefits of fast scan time, silent scanning, and artifact resistance.[6-10]

Imaging Technique of the ZTE Sequence

The basis of the ZTE sequence is to focus on very short T2 time tissues and structures considered invisible on MRI. The bone cortex and calcified structures have low proton density and short T2 relaxation times.[3] Therefore, the appearance of these structures results in signal voids on conventional MRI sequences.

The ZTE sequence is based on nonselective volume excitation and 3D radial center-out k-space encoding. Gradients are used continuously, and progressively reorienting in the x, y, and z axes between repetitions. Thus, the data are sampled along purely frequency-encoded center-out 3D radial trajectories in k-space (Figure 1).[11,12]

The acquisition of the free induction decay signal occurs immediately after excitation. The fast radiofrequency (RF) switch from transmit to receive enables acquisition of the quickly decaying signal starting at near-zero-echo time. The principle of capturing the small amount of signal found in cortical bone and calcific structures is based on this MRI physics.

In contrast to conventional pulse sequences, ZTE utilizes a readout gradient amplitude that is kept consistent throughout scanning with small directional changes between repetitions. This method outputs unique properties regarding silent scanning and nominal zero echo time.[12]

In ZTE, the RF excitation is entangled with the image encoding readout gradient. The RF block pulses are able to achieve consistent excitation because the RF excitation bandwidth covers the full RF imaging bandwidth, regardless of the readout gradient. As a result, the RF pulse width must be shorter than the RF sampling period, thereby limiting the maximum possible flip angle. If the RF pulse width is longer than the RF sampling period, the readout gradient may cause sinc-shape modulation of the RF excitation profile along the readout direction. Owing to the changing readout direction throughout the sequence, this would cause blurring that scales with increasing distance from the center of the imaging field of view (FOV).[13]

Chemical shift artifacts lead to image blurring and signal interference at fat-water interfaces, thus degrading the clarity of cortical bone depiction. To prevent this

Affiliations: Department of Radiology, Izmir Tepecik Education and Research Hospital, University of Health Sciences, Izmir, Turkey (Yuruk). Department of Radiology, Izmir City Hospital, Izmir, Turkey (Yuruk, Simsar, Pekcevik). Department of Radiology, Izmir Faculty of Medicine, University of Health Sciences, Izmir, Turkey (Pekcevik).

Disclosure: The authors have no conflicts of interest to disclose. None of the authors received outside funding for the production of this original manuscript and no part of this article has been previously published elsewhere.

Published: February 1, 2025. https://doi.org/10.37549/AR-D-24-0065

Figure 1. Illustration of zero-echo-time sequence. Gradients (G) are ramped up before the initial radiofrequency (RF) pulse. Gradients are continuously on with modulations prior to individual RF excitations and switched off at the end of the sequence. As a result of the dead-time (Δt) following the RF (while the signal cannot be acquired), there is a spherical gap at the center of the k-space, resulting in the missed data points.

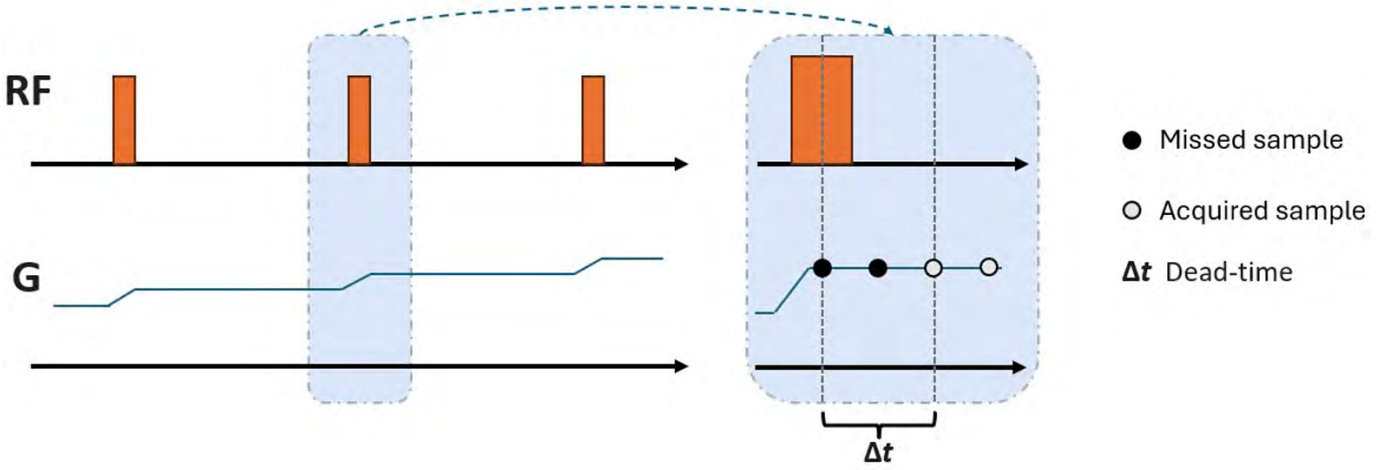

degradation, a pixel bandwidth larger than the oil-water chemical shift (i.e., 3.5 ppm) should be used.[13]

Robust coil bias correction along with grayscale inversion may assist in differentiating cortical bone from other short-T2, collagen-rich structures (the joint capsule, labra, or menisci) by producing CT-like images. Another advantage of the ZTE is that it allows the use of intensity projection to produce CT-like images and multiplanar and radial reformatting as in CT. The spatial resolution of ZTE is lower than that of CT. Today, the spatial resolution of ZTE is 0.8-1.2 cm, while the current highest value of CT is 0.625 mm. Despite the low spatial resolution of ZTE, CT-like images may be obtained by grayscale inversion automatically or with a single click via the picture archiving and communication system.[13-15]

Ultimately, several factors play a role in determining the usability of ZTE images for clinical purposes. Of these factors, receiver bandwidth (50 kHz at 1.5 T and 62.5 or 83.33 kHz at 3 T), flip angle (1° or 2°), and FOV (180×180 mm through 420×420 mm) are particularly important.[13] Knowing all these imaging features allows for better-quality images to be obtained.

Clinical Feasibility of the ZTE Sequence

Musculoskeletal Imaging

Computed tomography and radiography are often used to evaluate bone and calcific structures, while MRI is typically used to evaluate soft tissues such as muscles and tendons (Figure 2). Radiography or CT is used when conventional MRI is unable to distinguish pathology from bone and soft tissue. In addition, diagnosis may be difficult in cases where the patient has not had previous CT or radiography (Figure 3).

MRI, which includes the ZTE sequence, provides great benefit in terms of clinical use as it displays bone tissue and calcifications along with soft tissues (Figure 4).[3,6] With this method, many pathologies such as rheumatoid arthritis, osteoarthritis, spondylolysis, spondylolisthesis, fracture, joint dislocation, and metastases can be diagnosed with MRI instead of CT.[10,16] Moreover, MRI with the ZTE sequence is especially useful in cases where radiation should be avoided, such as in children, pregnant women, and patients with cancer.[17,18]

Head and Neck Imaging

Despite the increasing use of ZTE in musculoskeletal and body imaging, neuroimaging applications have been limited by the complexity of the head and neck anatomy and pathology.[19,20] Therefore, using the ZTE sequence in the head and neck is generally limited to acute trauma, pediatric patients, pregnant patients, metastasis screening, craniofacial malformations, and patients with genetic disorders who should not be exposed to radiation (Figure 5).[19]

Apart from these exceptions, there are examples in the literature that use MR angiography (MRA) with the ZTE sequence. ZTE imaging can be used in conjunction with an arterial spin labeling preparation module to achieve higher contrast during MRA.[21] ZTE-MRA may reduce artifacts around areas of magnetic

Figure 2. Sagittal plane x-ray image (A), zero-echo-time (ZTE)-grayscale inversion (B), T2 (C), and ZTE (D) MRI images from a normal left ankle. In ZTE-MRI, cortical bone structures are better demarcated and evaluated to the T2 sequence and are more like radiography.

Figure 3. Coronal plane T1 (A), zero-echo-time (ZTE)-grayscale inversion (B), and ZTE (C) MR images from the normal bilateral hip joints. In ZTE, the joint structure, acetabular roof, and cortical bone structures are evaluated more clearly compared with conventional MRI sequences.

Figure 4. Coronal plane T1 (A) and axial plane proton density (B) images demonstrate a thickness in the supraspinatus tendon at the level of its attachment to the humerus (arrows). Zero-echo-time-grayscale inversion (C) MR image clearly shows calcifications within the thickened tendon (arrowhead).

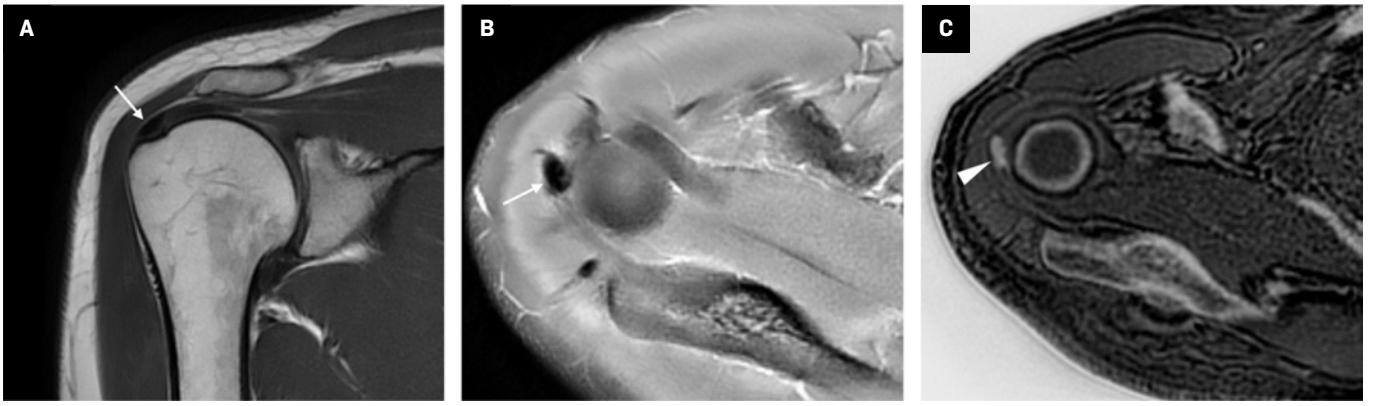

Figure 5. Axial (A) and coronal plane T1 (D) MR images show a low-signal lesion adjacent to the left mandible ramus (arrows). Axial (B) and coronal plane (E) zero-echo-time (ZTE)-grayscale inversion images show that the lesion originates from the ramus of the mandible. Axial (C) and coronal plane CT (F) images show similar features to the ZTE images and clearly show that the mass originates from the mandibular ramus. The lesion was diagnosed as an osteoma.

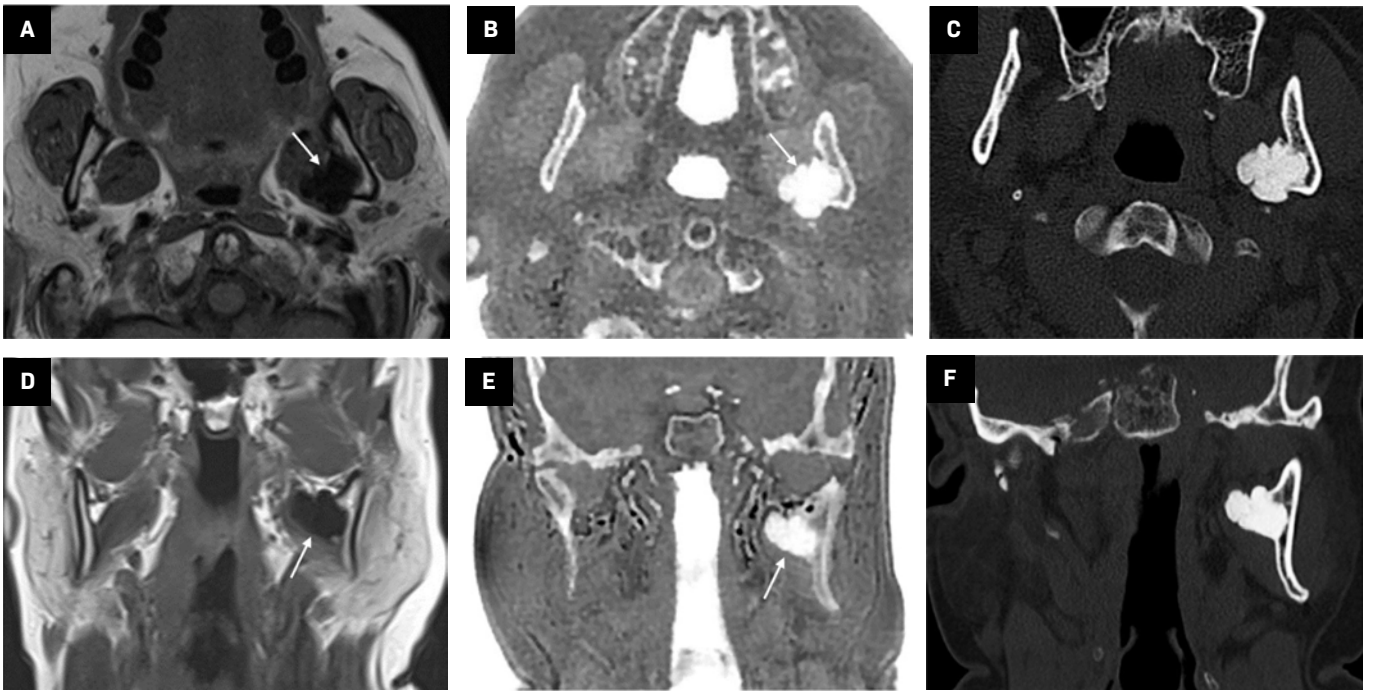

susceptibility gradients, which is important for imaging around stents and coils. Several studies have demonstrated improved vessel visualization around stents and coils with ZTE-MRA compared with conventional gradient echo-based TOF-MRA.[22-25]

Pediatric Imaging

Because it can image bone and soft-tissue pathologies without ionizing radiation, ZTE-MRI is expected to increase in popularity in pediatric imaging (Figure 6). Indeed, it is beginning to be used in some centers to image for suspected pathologies such as renal stones, ureteral stones, and bladder stones.[18]

Lung Imaging

Although high-resolution CT is primarily used for lung imaging, MRI with the ZTE sequence is being used

Figure 6. A 1-year-old with left-leg swelling. x-ray (A) shows a periosteal reaction at the lower end of the femur (arrows). However, no bone lesion could be distinguished on x-ray. Zero-echo-time-grayscale inversion (B) MR images clearly demonstrate a lytic bone lesion (arrowhead). The lesion was diagnosed as osteomyelitis.

Figure 7. Coronal plane zero-echo-timeMRI lung image.

in some centers as a radiation-free imaging method to diagnose and manage cystic fibrosis (Figure 7). MRI has the unique ability to distinguish scar tissue from active inflammation, making it particularly useful in this condition.[25]

Conclusion

The ZTE MRI sequence is a new technique that uses ultra-fast readouts to capture signals from short-T2 tissues to image cortical bone and calcific structures without ionizing radiation. This presents significant advantages over CT in pediatric patients, pregnant persons, and metastasis screening. It also represents a significant alternative to CT owing to its rapid screening speed, silent scanning, and artifact resistance. All-in-one MRI, including "CT-like images," appears poised to be used increasingly more often in the near future.

References

1) Lauterbur PC. Image formation by induced local interactions: examples employing nuclear magnetic resonance. *Nature*. 1973;242(5394):190-191. doi:10.1038/242190a0

2) Mansfield P. Multi-planar image formation using NMR spin echoes. *J Phys C: Solid State Phys*. 1977;10(3):L55-L58. doi:10.1088/0022-3719/10/3/004

3) Du J, Carl M, Bydder M, et al. Qualitative and quantitative Ultrashort Echo Time (UTE) imaging of cortical bone. *J Magn Reson*. 2010;207(2):304-311. doi:10.1016/j.jmr.2010.09.013

4) Zeman RK, Fox SH, Silverman PM, et al. Helical (spiral) CT of the abdomen. *AJR Am J Roentgenol*. 1993;160(4):719-725. doi:10.2214/ajr.160.4.8456652

5) Mettler FA Jr, Bhargavan M, Faulkner K, et al. Radiologic and nuclear medicine studies in the united states and worldwide: frequency, radiation dose, and comparison with other radiation sources—1950-2007. *Radiology*. 2009;253(2):520-531. doi:10.1148/radiol.2532082010

6) Wiesinger F, Sacolick LI, Menini A, et al. Zero TE MR bone imaging in the head. *Magn Reson Med*. 2016;75(1):107-114. doi:10.1002/mrm.25545

7) Endo Y. Diagnostic accuracy of zero-echo time MRI for the evaluation of cervical neural foraminal stenosis. *Spine*. 1976;43(13):928-933. doi:10.1097/BRS.0000000000002462

8) Breighner RE, Endo Y, Konin GP, et al. Technical developments: zero echo time imaging of the shoulder: enhanced osseous detail by using MR imaging. *Radiology*. 2018;286(3):960-966. doi:10.1148/radiol.2017170906

9) Breighner RE, Bogner EA, Lee SC, Koff MF, Potter HG. Evaluation of osseous morphology of the hip using zero echo time magnetic resonance imaging. *Am J Sports Med*. 2019;47(14):3460-3468. doi:10.1177/0363546519878170

10) Cho SB, Baek HJ, Ryu KH, et al. Clinical feasibility of zero TE skull MRI in patients with head trauma in comparison with CT: a single-center study. *AJNR Am J Neuroradiol*. 2019;40(1):109-115. doi:10.3174/ajnr.A5916

11) Weiger M, Pruessmann KP, Hennel F. MRI with zero echo time: hard versus sweep pulse excitation. *Magn Reson Med*. 2011;66(2):379-389. doi:10.1002/mrm.22799

12) Mastrogiacomo S, Dou W, Jansen JA, Walboomers XF. Magnetic resonance imaging of hard tissues and hard tissue engineered bio-substitutes. *Mol Imaging Biol*. 2019;21(6):1003-1019. doi:10.1007/s11307-019-01345-2

13) Aydıngöz Ü, Yıldız AE, Ergen FB. Zero echo time musculoskeletal MRI: technique, optimization, applications, and pitfalls. *Radiographics*. 2022;42(5):1398-1414. doi:10.1148/rg.220029

14) Froidevaux R, Weiger M, Rösler MB, Brunner DO, Pruessmann KP. HYFI: hybrid filling of the dead-time gap for faster zero echo time imaging. *NMR Biomed*. 2021;34(6):e4493. doi:10.1002/nbm.4493

15) Ilbey S, Jungmann PM, Fischer J, et al. Single point imaging with radial acquisition and compressed sensing. *Magn Reson Med*. 2022;87(6):2685-2696. doi:10.1002/mrm.29156

16) Bessa FS, Williams BT, Polce EM, et al. No differences in hip joint space measurements between weightbearing or supine anteroposterior pelvic radiographs. *Arthroscopy*. 2020;36(11):2843-2848. doi:10.1016/j.arthro.2020.07.009

17) Larson PEZ, Han M, Krug R, et al. Ultrashort echo time and zero echo time MRI at 7T. *MAGMA*. 2016;29(3):359-370. doi:10.1007/s10334-015-0509-0

18) Ozcan HN, Ozer G, Dogan HS, et al. Zero-echo time MRI: an alternative method for the diagnosis of urinary stones in children. *Eur Radiol*. 2025;35(1):289-296. doi:10.1007/s00330-024-10950-x

19) Wiesinger F, Ho M-L. Zero-TE MRI: principles and applications in the head and neck. *Br J Radiol*. 2022;95(1136):20220059. doi:10.1259/bjr.20220059

20) Zheng W, Kim JP, Kadbi M, et al. Magnetic resonance-based automatic air segmentation for generation of synthetic computed tomography scans in the head region. *Int J Radiat Oncol Biol Phys*. 2015;93(3):497-506. doi:10.1016/j.ijrobp.2015.07.001

21) Shang S, Ye J, Dou W, et al. Validation of zero TE-MRA in the characterization of cerebrovascular diseases: a feasibility study. *AJNR Am J Neuroradiol*. 2019;40(9):1484-1490. doi:10.3174/ajnr.A6173

22) Irie R, Suzuki M, Yamamoto M, et al. Assessing blood flow in an intracranial stent: a feasibility study of MR angiography using a silent scan after stent-assisted coil embolization for anterior circulation aneurysms. *AJNR Am J Neuroradiol*. 2015;36(5):967-970. doi:10.3174/ajnr.A4199

23) Takano N, Suzuki M, Irie R, et al. Non-contrast-enhanced silent scan MR angiography of intracranial anterior circulation aneurysms treated with a low-profile visualized intraluminal support device. *AJNR Am J Neuroradiol*. 2017;38(8):1610-1616. doi:10.3174/ajnr.A5223

24) Shang S, Ye J, Luo X, et al. Follow-up assessment of coiled intracranial aneurysms using ZTE MRA as compared with TOF MRA: a preliminary image quality study. *Eur Radiol*. 2017;27(10):4271-4280. doi:10.1007/s00330-017-4794-z

25) Heo YJ, Jeong HW, Baek JW, et al. Pointwise encoding time reduction with radial acquisition with subtraction-based MRA during the follow-up of stent-assisted coil embolization of anterior circulation aneurysms. *AJNR Am J Neuroradiol*. 2019;40(5):815-819. doi:10.3174/ajnr.A6035

Contrast-Enhanced US for Characterization and Biopsy of Indeterminate Hepatic Lesions and Metastases: A Review with Case Examples

Jacob Schick, MD; Tej Mehta, MD; Farzad Sedaghat, MD

During the past decade, there have been significant advances in systemic therapy for oncologic disease. Most notably, immunotherapeutics have prolonged survival in patients with previously untreatable, advanced metastatic disease.[1] Concurrently, innovations in medical imaging have made radiologic exams increasingly sensitive in detecting metastases,[2,3] and well-elucidated imaging criteria, such as RECIST, have been validated for assessing treatment response.[4] These factors have led to significant increases in the volume and frequency of oncologic imaging exams.[5,6]

Imaging Techniques

Contrast-enhanced CT (CECT) is the mainstay of oncologic imaging, where it is used for disease staging and surveillance.[7] While the appearance of metastases varies based on the primary malignancy and site of metastasis, many visceral metastases have classic features that may obviate the need for biopsy.[8,9] The liver, one of the most common sites for metastatic disease, is well visualized on CECT scans, allowing for effective metastasis detection.[10] Nonetheless, the variable appearance of metastatic lesions and the possibility of benign mimics can make definitive characterization of hepatic lesions impossible.[11,12]

Most hepatic metastases appear hypoenhancing on CECT, with colorectal, lung, and breast cancer metastases serving as classic examples.[9,10] As lesions grow, central necrosis can give lesions a rim-enhancing appearance with a nonenhancing liquid center.[9] Conversely, hemangioma, the most commonly encountered benign hepatic neoplasm, exhibits progressive peripheral nodular enhancement, with fill-in on delayed phases.[12]

A minority of hepatic metastases appear hyperenhancing and are most conspicuous on arterial phase exams. These include melanoma, renal cell carcinoma, and neuroendocrine tumors.[9,12] While these lesions tend to exhibit washout in the latter phases, distinguishing them from benign entities such as focal nodular hyperplasia or adenoma can be difficult without prior imaging to confirm lesion stability.[12] Furthermore, this imaging appearance may be indistinguishable from well-differentiated hepatocellular carcinoma, though a benign neoplasm would be statistically favored in the absence of cirrhosis.[12]

Increasingly, hepatic metastases are being detected with highly sensitive, advanced imaging techniques like MRI with diffusion-weighted imaging, FDG-PET, or targeted radionuclide SPECT.[13,14] MRI is particularly useful in detecting and surveilling liver metastasis. On T2 sequences, these metastases are typically mildly T2 hyperintense, with possibly moderate central T2 signal intensity in the presence of concurrent cystic or necrotic changes. This contrasts with the marked T2 hyperintensity of many benign lesions. T1 hyperintensity varies and reflects the histologic characteristics of the underlying metastatic lesion. Gradient echo sequences allow detection of iron and fat deposition within focal lesions, which can further aid lesion characterization.

Hepatobiliary contrast agents (HBAs) have increased sensitivity in detecting liver metastasis. These agents can exclude primary hepatic lesions since metastatic lesions will appear hypointense on delayed HBA sequences owing to the absence of functional hepatocytes. One meta-analysis found that Gd-EOB-DTPA demonstrated a higher per-lesion sensitivity than CECT, a median of 94.9% versus 74.2%, respectively.[15]

Affiliation: The Russell H Morgan Department of Radiology and Radiologic Science, Johns Hopkins Hospital, Baltimore, Maryland.
Disclosure: The authors have no conflicts of interest to disclose. None of the authors received outside funding for the production of this original manuscript and no part of this article has been previously published elsewhere.

Published: February 1, 2025. https://doi.org/10.37549/AR-D-24-0066

On diffusion-weighted imaging, metastases commonly exhibit low apparent diffusion coefficient values, reflecting high cellularity, with a reported sensitivity of 87% for liver metastases.[16]

Ultrasound, while used less often in cancer surveillance due to reduced sensitivity,[17] plays a significant role in percutaneous image-guided liver biopsy. It imparts no radiation dose to the patient and provider, allowing continuous real-time imaging. This capability aids precise lesion localization and identification of sensitive surrounding structures, ensuring a safer biopsy approach.[18]

The use of contrast-enhanced US (CEUS) for the assessment and sampling of hepatic metastases has been demonstrated in multiple case series.[19-21] This modality employs microbubble-based agents, which are composed of a fluorinated gas core enveloped by a phospholipid shell. The gas core is exhaled through the lungs, while the phospholipid component is metabolized by the liver, bypassing renal excretion. Lesions typically exhibit enhancement similar to that seen on cross-sectional imaging, but their enhancement characteristics may be better elucidated given the superior temporal resolution afforded by continuous image acquisition.[22] These data can be used to generate kinetics curves, which aid delineation of benign and malignant lesions and, in the case of heterogeneous tumors, identify areas of rapid enhancement and washout, which are predictive of aggressive tumor histology.[23] Additionally, like other contrast-enhanced techniques, CEUS can reliably distinguish enhancing tumor from nonenhancing regions of necrosis and has been found to increase single-puncture success rate and diagnostic accuracy.[19]

At our institution, US contrast is administered for biopsy in select cases where lesions are sonographically occult or exhibit significant heterogeneity on grayscale US.

The following 4 cases illustrate the utility of CEUS for hepatic biopsies.

Case No. 1: Colon Cancer

An elderly patient with a history of metastatic colon cancer was referred to radiology for biopsy of growing hypoattenuating hepatic lesions seen on surveillance CT exam (Figure 1). The patient had previously been treated with a chemotherapy regimen of FOLFOX and bevacizumab, which was discontinued owing to enlargement of the presumed metastatic lesions. Biopsy was requested to assess eligibility for an immunotherapy research trial.

Initial grayscale US demonstrated a subtle contour bulge, which was much less conspicuous than that corresponding to the dominant hypoattenuating lesion seen on CT. Administration of 2 mL of Lumason (sulfur hexafluoride lipid-type A microspheres) revealed a lobulated lesion with persistent, thick peripheral enhancement and a central nonenhancing component, presumed to represent necrosis. Based on the CEUS, the lesion's periphery was targeted for percutaneous biopsy. Initial 25G fine-needle aspiration (FNA) with on-site cytopathology was suspicious for metastatic adenocarcinoma. Multiple 18G core biopsies later confirmed the diagnosis and were sent for immunohistochemical analysis for potential clinical trial enrollment. The patient tolerated the procedure well and was discharged home following a brief recovery.

Case No. 2: Neuroendocrine Tumor

An adult with metastatic neuroendocrine tumor of the small bowel was referred for biopsy of presumed hepatic metastases. The patient had previously received treatment with somatostatin analogs (octreotide LAR, Lutathera) and sunitinib and had relatively stable disease until their most recent DOTATE-PET/CT (Figure 2), which showed multiple radiotracer-avid hepatic lesions growing in size and number. The patient was presumed to have progressive metastatic disease in the setting of continued therapy, raising concern for tumor mutation/dedifferentiation. Multiphase CECT demonstrated no correlation to the radiotracer-avid hepatic lesions. Subsequent CEUS (2 mL Lumason, 2 boluses) revealed a subtle, hyperenhancing, subcapsular right hepatic lobe lesion corresponding to a radiotracer-avid focus on DOTATE-PET/CT. 25G FNA revealed a metastatic neuroendocrine tumor, and multiple 18G core biopsies were obtained for immunohistochemical staining, which demonstrated an increase in Ki67 proliferation index. Based on these results, therapy was initiated with everolimus, a kinase inhibitor.

Case No. 3: Pseudolesion

An adult with a history of choroidal ocular melanoma presented with an indeterminate, mildly T2 hyperintense, right hepatic lobe lesion seen on MRI (Figure 3). The patient had previously been treated with light-activated AU-011

Figure 1. (A) Contrast-enhanced CT demonstrates multiple hypoattenuating lesions within the right hepatic lobe (arrows). (B) Contrast-enhanced US demonstrates a lobulated subcapsular lesion corresponding to the larger, hypoattenuating lesion seen on CT, with thick peripheral enhancement (arrows) and hypoechoic center (white arrowheads), presumed to represent necrosis. (C) Subtle corresponding contour (black arrowhead) is seen on grayscale US.

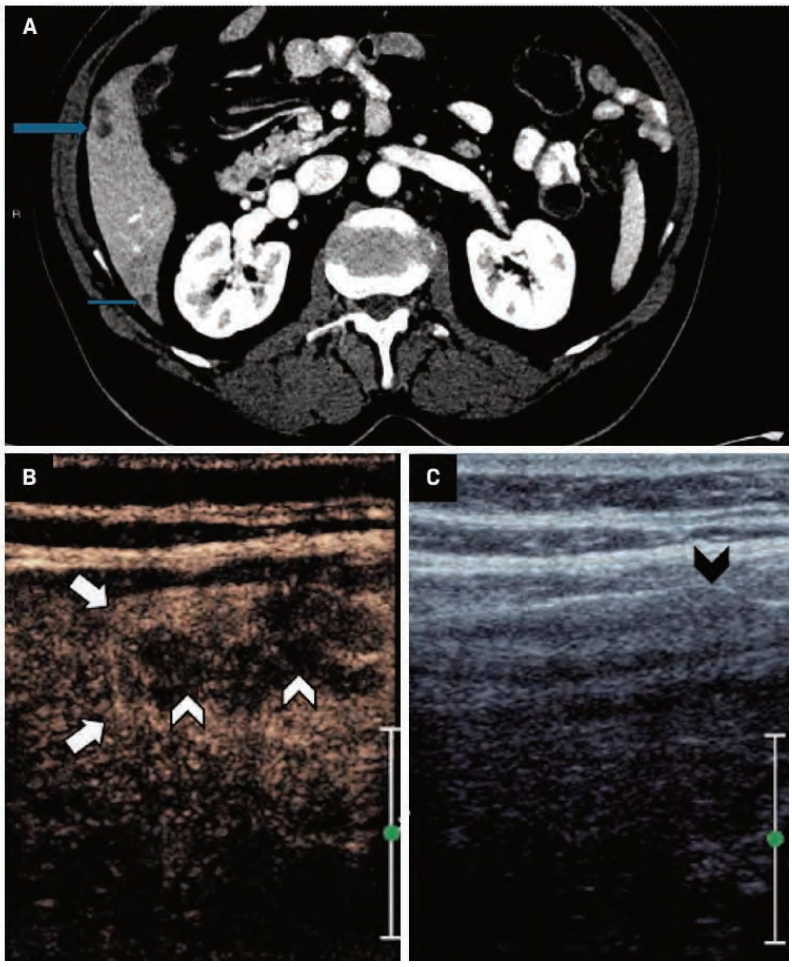

conjugated nanoparticles and had no history of metastatic disease. Given the patient's high-risk disease, the clinical significance of a metastatic lesion, and that the lesion was occult on grayscale US, a CEUS biopsy was performed.

The lesion was identified using anatomic landmarks, and approximately 30 seconds post-administration of 2 mL of US contrast (Lumason), a rim-enhancing lesion was seen. The lesion became isoechoic on subsequent images and was indistinguishable from the liver parenchyma at 60 seconds. While apparent progressive enhancement is atypical for melanoma metastases, the lesion remained indeterminate, and the early-enhancing periphery was targeted for biopsy. Multiple 18G core biopsy samples were obtained, revealing benign hepatocytes with a background of chronic inflammation but no evidence of melanoma. This case highlights the utility of CEUS in delineating occult lesions on grayscale imaging, and its use in targeting biologically active portions of a lesion. Short interval follow-up MRI was stable, and the patient is currently presumed to be disease free.

Case No. 4: Hepatocellular Carcinoma from a Hepatic Adenoma

An adult with no significant medical history presented with an incidental liver mass noted on chest CT (Figure 4). Further characterization with MRI revealed multiple hepatic lesions, the largest of which measured 10.8 × 7.0 cm, with mild T2 hyperintensity, heterogeneous arterial enhancement, and equivocal regions of washout. The lesions all displayed arterial enhancement without washout. A biopsy of the largest lesion revealed a well-differentiated hepatocellular carcinoma arising from within a hepatic adenoma. The patient underwent partial hepatectomy with biopsy and ablation of the remaining liver lesions greater than 1 cm. Pathology of the smaller lesions revealed multiple hepatic adenomas.

Following liver resection, the patient became pregnant. Owing to the risk of growth and rupture during pregnancy, the patient was monitored with serial imaging and alpha-fetoprotein. Since contrast-enhanced MRI is not recommended to monitor lesion size in pregnancy, CEUS was used to assess lesion stability for short-term follow-up. The patient's most recent CEUS

Figure 2. (A) DOTATE-PET demonstrates multiple radio-avid hepatic metastases (white arrows), occult on (B) corresponding contrast-enhanced CT.32id focus (black arrow). (D) A mildly hypoechoic correlate, noted on grayscale US (arrowhead), is difficult to identify prospectively given the heterogeneous appearance of the liver.

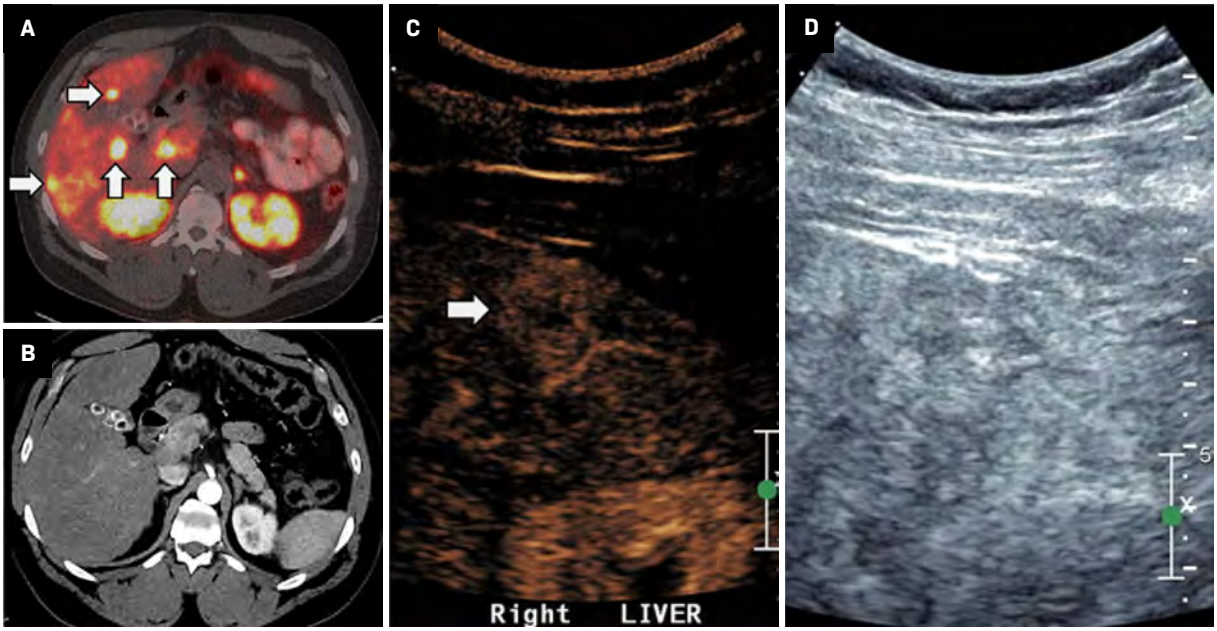

demonstrated mild growth of the largest hepatic adenoma but no suspicious washout, and continued surveillance was recommended.

Discussion

The liver is one of the most common sites of metastatic disease. In general, the prognosis for patients with hepatic metastases has historically been poor.[24] In the past decade, however, effective systemic treatments have emerged for advanced metastatic disease, most notably immunotherapeutics.[1] In this context, the frequency of surveillance imaging and hepatic biopsy has significantly increased.[5,8]

CT is the mainstay of cancer imaging surveillance, often performed at intervals of 3-12 months.[9-13] Imaging surveillance is typically accompanied by clinical follow-up and, when available, trending of serum tumor markers such as CEA (colorectal cancer), CA 19-9 (pancreatic cancer), and CA 125 (ovarian cancer).[25] In certain malignancies, advanced imaging such as MRI, FDG-PET, or targeted radionuclide SPECT may also be performed.[14]

The response to a newly detected hepatic lesion is influenced by radiologic findings and clinical factors. Depending on the lesion's appearance and chronicity, one can speculate on the likelihood of metastatic disease. Indeterminate findings may prompt consideration of biopsy for definitive diagnosis.[18,19] In cases of presumed tumor, the proliferation of novel targeted therapeutic options has increased the need for tissue sampling as many of these treatments are contingent on detection of specific targets requiring advanced histologic and immunohistochemical staining.[1]

This is particularly true in clinical trials, where therapies pose significant risks, and only a subset of patients with specific mutations may be eligible for enrollment.[26] Alternatively, in certain cases, hepatic metastases may trigger re-evaluation of treatment options and objectives. For example, a new hepatic metastasis may indicate disease progression, resulting in changes to treatment regimen and imaging frequency.[4] In cases of oligometastatic disease, percutaneous ablation or surgical wedge resection may be considered. Finally, instances where systemic and surgical treatment options are limited may prompt reassessment of care and disease management goals.

CT and US are the mainstays of image-guided intervention. US is typically preferred owing to the absence of ionizing radiation and the availability of continuous, real-time imaging.[18] In cases of sonographically occult lesions, CECT has often been used as a guidance modality; however, many grayscale occult lesions can be effectively characterized and targeted with CEUS, obviating the need for ionizing radiation and potentially nephrotoxic iodinated contrast.[19-22]

Figure 3. (A) MRI demonstrates a mildly T2 hyperintense right hepatic lobe lesion (white arrow). (B) Contrast-enhanced US at 30 seconds demonstrates a corresponding rim-enhancing lesion (black arrow). (C) Lesion is isoechoic at 60 seconds and (D) occult on greyscale US.

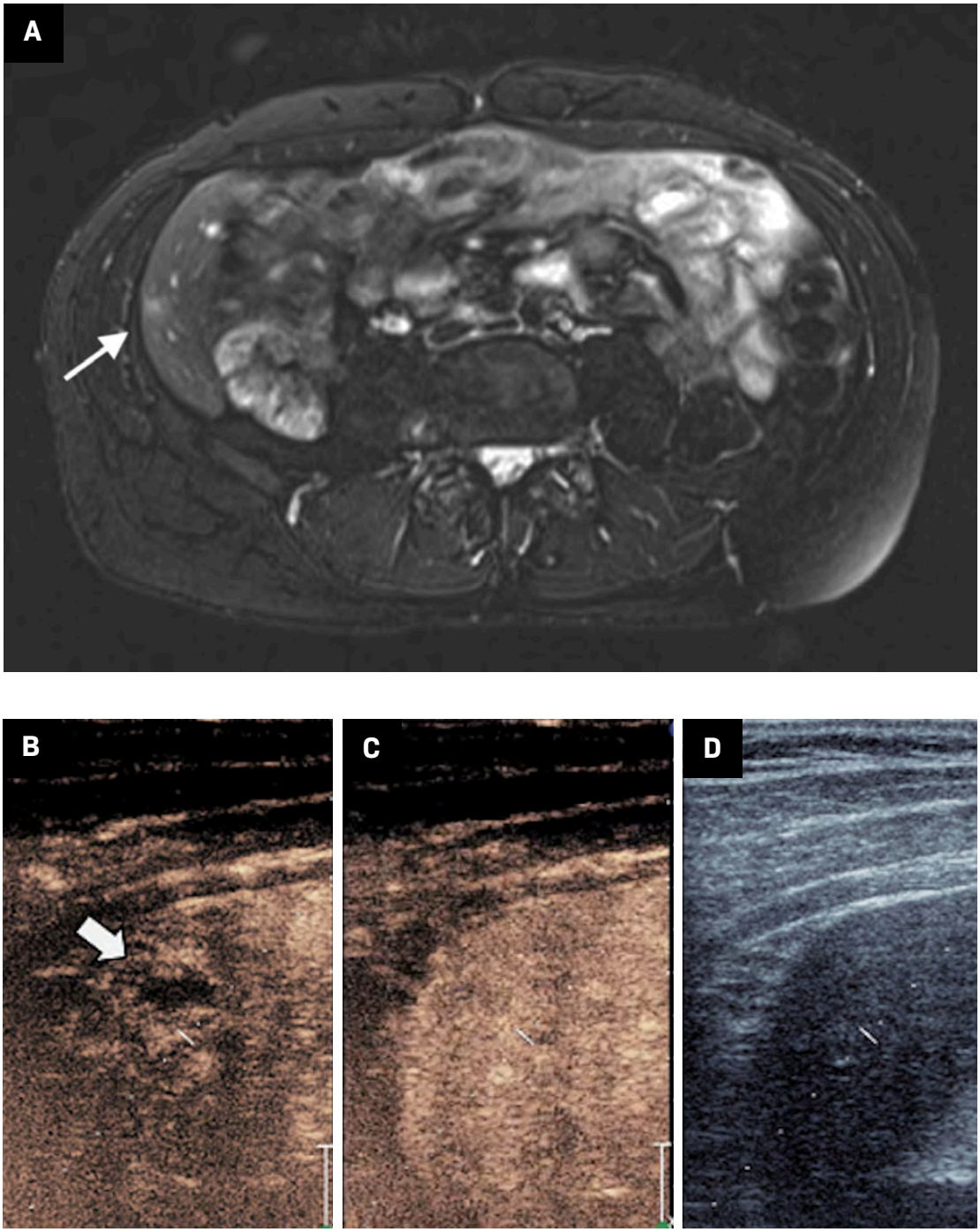

In addition, multiple rounds of CEUS can be administered, allowing for initial image acquisition for diagnosis and subsequent real-time biopsy guidance.[19-21] While contrast quickly degrades (typically within 10 minutes), microspheres can also be annihilated at any time using a high-powered pulse to shorten procedure length.

During a typical CEUS biopsy, a lesion is continuously imaged for at least 60 seconds, allowing visualization of sonographically occult lesions and assessment of

Figure 4. MRI demonstrates an enhancing mass at the inferior aspect of the right lobe of the liver (A, blue arrowhead), with pathology confirming hepatocellular carcinoma arising from an adenoma. Subsequently, lesions > 1 cm were ablated. (B)Middle image demonstrates postablation changes from a treated adenoma (arrow). An enhancing lesion is present at the hepatic dome (arrowhead), consistent with an adenoma that did not meet the size criteria for ablation. (C)On surveillance imaging, the adenoma appears hypoechoic on grayscale images (arrowhead) but is without any suspicious enhancement on contrast-enhaced US, as noted on short-term follow-up during pregnancy.

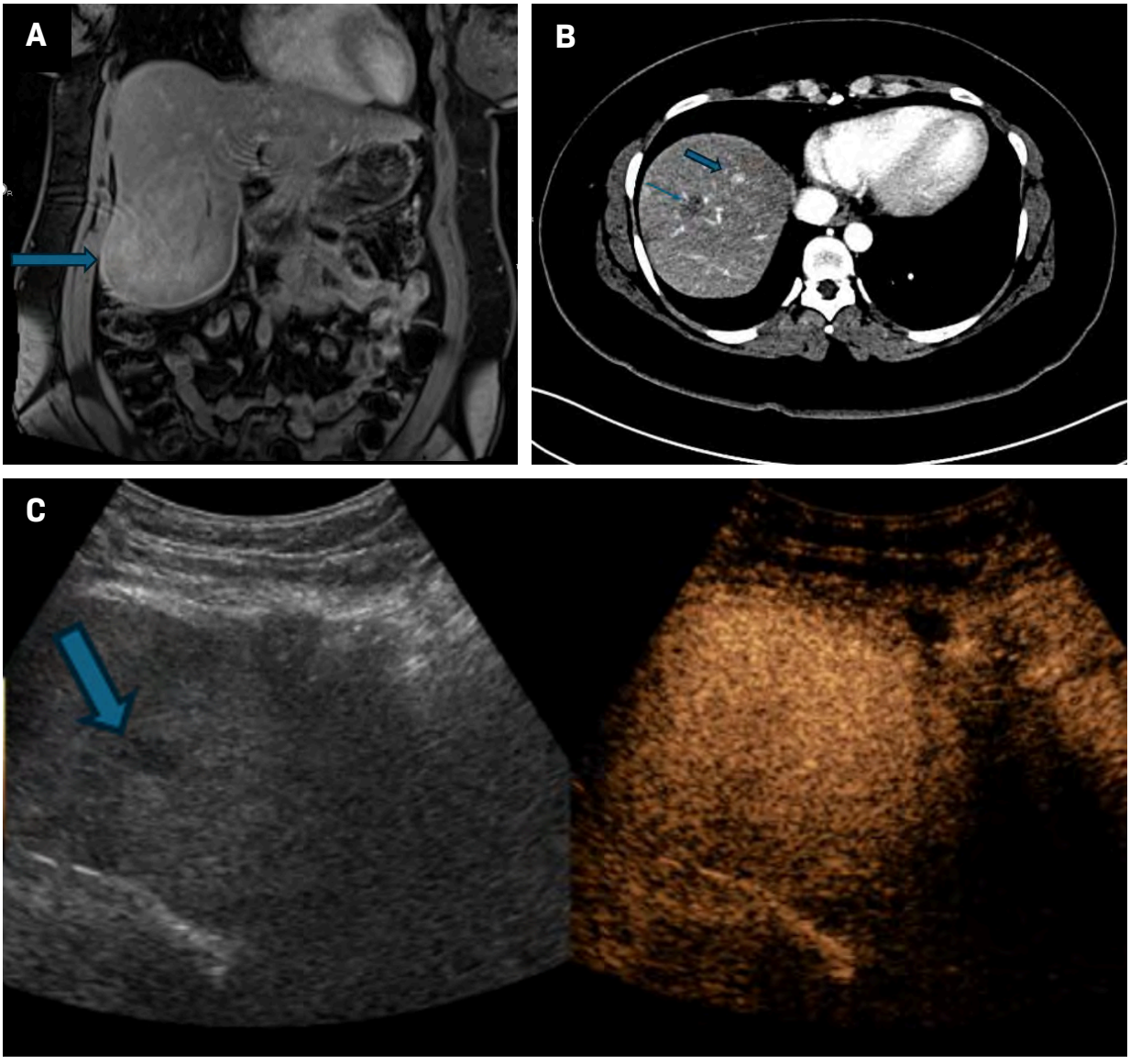

lesion enhancement kinetics.[23] In the setting of heterogeneous lesions, specific targets can be selected, not only to avoid nonenhancing areas of necrosis/debris but also to identify areas of avid arterial enhancement and washout predictive of more aggressive disease.[21] CEUS is also shown to increase the accuracy of percutaneous liver biopsy, particularly in lesions < 2 cm, and reduce the number of puncture attempts.

This targeting is of growing importance as the use of certain immunotherapies depends not only on the presence but also the relative expression of specific tumor markers.[27] As oncologic therapies progress, moreover, the need for representative tumor samples and CEUS for effective lesion characterization and sampling is likely to advance along with them.

References

1) Sharma P, Wagner K, Wolchok JD, Allison JP. Novel cancer immunotherapy agents with survival benefit: recent successes and next steps. *Nat Rev Cancer*. 2011;11(11):805-812. doi:10.1038/nrc3153

2) Lestra T, Mulé S, Millet I, et al. Applications of dual energy computed tomography in abdominal imaging. *Diagn Interv Imaging*. 2016;97(6):593-603. doi:10.1016/j.diii.2015.11.018

3) Alabousi M, McInnes MD, Salameh J-P, et al. MRI vs. CT for the detection of liver metastases in patients with pancreatic carcinoma: a comparative diagnostic test accuracy systematic review and meta-analysis. *J Magn Reson Imaging*. 2021;53(1):38-48. doi:10.1002/jmri.27056

4) Eisenhauer EA, Therasse P, Bogaerts J, et al. New response evaluation criteria in solid tumours: revised RECIST guideline (version 1.1). *Eur J Cancer*. 2009;45(2):228-247. doi:10.1016/j.ejca.2008.10.026

5) Mitchell JM, Lagalia RR. Controlling the escalating use of advanced imaging: the role of radiology benefit management programs. *Med Care Res Rev*. 2009;66(3):339-351. doi:10.1177/1077558709332055

6) Iglehart JK. The new era of medical imaging--progress and pitfalls. *N Engl J Med*. 2006;354(26):2822-2828. doi:10.1056/NEJMhpr061219

7) Jaffe TA, Wickersham NW, Sullivan DC. Quantitative imaging in oncology patients: part 1, radiology practice patterns at major U.S. cancer centers. *AJR Am J Roentgenol*. 2010;195(1):101-106. doi:10.2214/AJR.09.2850

8) Torzilli G, Minagawa M, Takayama T, et al. Accurate preoperative evaluation of liver mass lesions without fine-needle biopsy. *Hepatology*. 1999;30(4):889-893. doi:10.1002/hep.510300411

9) Sica GT, Ji H, Ros PR. CT and MR imaging of hepatic metastases. *AJR Am J Roentgenol*. 2000;174(3):691-698. doi:10.2214/ajr.174.3.1740691

10) Baron RL. Understanding and optimizing use of contrast material for CT of the liver. *AJR Am J Roentgenol*. 1994;163(2):323-331. doi:10.2214/ajr.163.2.8037023

11) Wittenberg J, Stark DD, Forman BH, et al. Differentiation of hepatic metastases from hepatic hemangiomas and cysts by using MR imaging. *AJR Am J Roentgenol*. 1988;151(1):79-84. doi:10.2214/ajr.151.1.79

12) van Leeuwen MS, Noordzij J, Feldberg MA, Hennipman AH, Doornewaard H. Focal liver lesions: characterization with triphasic spiral CT. *Radiology*. 1996;201(2):327-336. doi:10.1148/radiology.201.2.8888219

13) Semelka RC, Worawattanakul S, Kelekis NL, et al. Liver lesion detection, characterization, and effect on patient management: comparison of single-phase spiral CT and current MR techniques. *Magnetic Resonance Imaging*. 1997;7(6):1040-1047. doi:10.1002/jmri.1880070616

14) Chua SC, Groves AM, Kayani I, et al. The impact of 18F-FDG PET/CT in patients with liver metastases. *Eur J Nucl Med Mol Imaging*. 2007;34(12):1906-1914. doi:10.1007/s00259-007-0518-y

15) Vreugdenburg TD, Ma N, Duncan JK, et al. Comparative diagnostic accuracy of hepatocyte-specific gadoxetic acid (gd-EOB-DTPA) enhanced MR imaging and contrast enhanced CT for the detection of liver metastases: a systematic review and meta-analysis. *Int J Colorectal Dis*. 2016;31(11):1739-1749. doi:10.1007/s00384-016-2664-9

16) Vilgrain V, Esvan M, Ronot M, et al. A meta-analysis of diffusion-weighted and gadoxetic acid-enhanced MR imaging for the detection of liver metastases. *Eur Radiol*. 2016;26(12):4595-4615. doi:10.1007/s00330-016-4250-5

17) Wernecke K, Rummeny E, Bongartz G, et al. Detection of hepatic masses in patients with carcinoma: comparative sensitivities of sonography, CT, and MR imaging. *AJR Am J Roentgenol*. 1991;157(4):731-739. doi:10.2214/ajr.157.4.1892027

18) Garcia-Tsao G, Boyer JL. Outpatient liver biopsy: how safe is it?. *Ann Intern Med*. 1993;118(2):150-153. doi:10.7326/0003-4819-118-2-199301150-00013

19) Xu H-X, Liu G-J, Lu M-D, et al. Characterization of small focal liver lesions using real-time contrast-enhanced sonography: diagnostic performance analysis in 200 patients. *J Ultrasound Med*. 2006;25(3):349-361. doi:10.7863/jum.2006.25.3.349

20) Wu W, Chen M-H, Yin S-S, et al. The role of contrast-enhanced sonography of focal liver lesions before percutaneous biopsy. *AJR Am J Roentgenol*. 2006;187(3):752-761. doi:10.2214/AJR.05.0535

21) Cantisani V, Grazhdani H, Fioravanti C, et al. Liver metastases: contrast-enhanced ultrasound compared with computed tomography and magnetic resonance. *World J Gastroenterol*. 2014;20(29):9998-10007. doi:10.3748/wjg.v20.i29.9998

22) Claudon M, Cosgrove D, Albrecht T, et al. Guidelines and good clinical practice recommendations for contrast enhanced ultrasound (CEUS) - update 2008. *Ultraschall Med*. 2008;29(1):28-44. doi:10.1055/s-2007-963785

23) Stramare R, Gazzola M, Coran A, et al. Contrast-enhanced ultrasound findings in soft-tissue lesions: preliminary results. *J Ultrasound*. 2013;16(1):21-27. doi:10.1007/s40477-013-0005-1

24) Choti MA, Bulkley GB. Management of hepatic metastases. *Liver Transpl Surg*. 1999;5(1):65-80. doi:10.1002/lt.500050113

25) Perkins GL, Slater ED, Sanders GK, Prichard JG. Serum tumor markers. *Am Fam Physician*. 2003;68(6):1075-1082.

26) Levy EB, Fiel MI, Hamilton SR, et al. State of the art: toward improving outcomes of lung and liver tumor biopsies in clinical trials-A multidisciplinary approach. *J Clin Oncol*. 2020;38(14):1633-1640. doi:10.1200/JCO.19.02322

27) Patel SP, Kurzrock R. PD-L1 expression as a predictive biomarker in cancer immunotherapy. *Mol Cancer Ther*. 2015;14(4):847-856. doi:10.1158/1535-7163.MCT-14-0983

BRACCO

LIFE FROM INSIDE